

Advanced Analysis of Battery Materials via Correlative Charged Particle Characterisation Techniques

Von der Fakultät 3 – Chemie der Universität Stuttgart zur Erlangung der Würde
eines Doktors der Naturwissenschaften (Dr. rer. nat.) genehmigte Abhandlung

Vorgelegt von

Luca CRESSA

aus Esch-sur-Alzette, Luxemburg

Hauptberichter: Prof. Dr. Dr. h.c. Guido Schmitz
Mitberichter: Dr. habil. Santhana Eswara Moorthy
Prüfungsvorsitzender: Prof. Dr. Joris van Slageren

Tag der mündlichen Prüfung: 05.12.2023

Institut für Materialwissenschaft der Universität Stuttgart

2023

Erklärung über die Eigenständigkeit der Dissertation

Ich versichere, dass ich die vorliegende Arbeit mit dem Titel

„Advanced Analysis of Battery Materials Via Correlative Charged Particle Characterisation Techniques “

selbständig verfasst und keine anderen als die angegebenen Quellen und Hilfsmittel benutzt habe; aus fremden Quellen entnommene Passagen und Gedanken sind als solche kenntlich gemacht.

Declaration of Authorship

I hereby certify that the dissertation entitled

„Advanced Analysis of Battery Materials Via Correlative Charged Particle Characterisation Techniques “

is entirely my own work except where otherwise indicated. Passages and ideas from other sources have been clearly indicated.

Name/Name: Cressa Luca

Unterschrift/Signed:



Datum/Date: 08.12.2023

Acknowledgements

I would like to thank my supervisors Dr. Santhana Eswara and Prof. Guido Schmitz for their supervision, their time, their availability, continuous support, their feedback, uncountable fruitful & intense discussions and for guiding me through this journey during the last almost four years.

I deeply acknowledge all LIST-internal but also external collaborators, scientists and engineers with whom I had the opportunity to work together during the last years. Thank you: M. Ihrig, J. Fell, A. Shaplov, F. Addiego, J. Guillot, P. Boillat, M. Gerard, O. Bouton, M. Clausnitzer, M. Nojabae, R. Costa, Y. Sun, J.-L. Biagi.

A special thanks goes to all those people which became more than just coworkers, but which I consider now as friends and without their support I would probably not have had the strength and persistence to finish this thesis. O. De Castro, K. Huber, B. Aspe, A. Ost, S. Tabean, C. Stoffels, D. Andersen, M. Sikiric C. B. Coulbary, P. Defino, V. Benito, M. Moreira, H. Ouhbi, G. Bengasi, K. Acharya, G. Defoort.

Uncommented acknowledgements go to GangGang and C&C.

Finally, I would like to thank my mom, my dad and my sister for the constant support and believing in me, without you I would not be the man I am today.

Acronyms and Abbreviations

Abstract/Kurzzusammenfassung

Preface

Introduction

Structure of the Thesis

1. CHAPTER 1 Background

1.1. Where we came from

1.2. Battery Research Today

1.2.1. Solid-State Batteries

1.2.2. $\text{Li}_7\text{La}_3\text{Zr}_2\text{O}_{12}$

1.2.3. Types of Li-accumulations in LLZO based batteries

1.3. Analysis & Characterization

1.3.1. Introduction to Correlative Microscopy & Spectroscopy

1.3.2. Introduction to SIMS

1.3.3. Introduction to *In-situ* & *Operando*

1.3.4. Advanced Analysis

1.4. Problem Statements

1.5. Thesis Objectives

Bibliography 1

2. CHAPTER 2 *Operando* Correlative SEM/SIMS

2.1. Motivation

2.2. Towards *Operando*

2.2.1. Prototype design

2.2.1.1. Electrochemical Experiments

2.2.1.2. Contact Pressure Control

2.2.1.3. Adaptation to inert gas transfer system and microscope

2.2.1.4. Final experimental configuration

2.2.2. Tests, validation, and proof of concept

- 2.2.2.1. Contact μ -manipulator – polarity plate
- 2.2.2.2. Resistance test
- 2.2.2.3. EIS comparison Swagelok – Operando holder
- 2.2.3. Materials and Sample Preparation
 - 2.2.3.1. Materials
 - 2.2.3.2. Sample Preparation
 - 2.2.3.3. SIMS analysis
- 2.2.4. Results & Discussion
 - 2.2.4.1. Pre-cycling
 - 2.2.4.2. CC cycling
 - 2.2.4.3. Post-cycling
 - 2.2.4.4. Limitations
 - 2.2.4.5. Discussion
- 2.3. Closing Remarks
- Bibliography 2

3. CHAPTER 3 X-ray Based Correlative Approaches

- 3.1. Motivation
- 3.2. μ CT for Solid State Electrolyte
 - 3.2.1. μ CT Analysis
 - 3.2.2. SIMS Analysis
 - 3.2.3. Results & Discussion
- 3.3. NanoCT for Cathode Material
 - 3.3.1. Sample preparation
 - 3.3.2. NanoCT Analysis
 - 3.3.3. SIMS Analysis
 - 3.3.4. Results & Discussion
 - 3.3.5. Conclusion
- 3.4. EDX & WDXS for composite LLZO-Cathode

- 3.4.1. Sample preparation
- 3.4.2. EDX Analysis
- 3.4.3. WDXS Analysis
- 3.4.4. SIMS Analysis
- 3.4.5. Results & Discussion
- 3.4.6. Case Study
- 3.5. Closing Remarks
- Bibliography 3

4. CHAPTER 4 *Operando* Neutron Imaging

- 4.1. Motivation
- 4.2. Experimental Design
 - 4.2.1. Design of the Sample Holder
 - 4.2.2. Final Experimental Configuration
- 4.3. Material & Methods
 - 4.3.1. Sample Preparation for *operando* Neutron Imaging
 - 4.3.2. Neutron Tomo- & Radiography
 - 4.3.3. Sample Preparation for ex-situ SEM/SIMS Analysis
 - 4.3.4. SIMS analysis
- 4.4. Results
 - 4.4.1. *Operando* Neutron Radiography
 - 4.4.2. Li Quantification
 - 4.4.3. From Neutron Imaging to Secondary Ion Mass Spectrometry
 - 4.4.4. Post-Mortem Structural and Chemical Characterisation
 - 4.4.5. Proposed Hypothesis
 - 4.4.6. Limitations
- 4.5. Conclusions
- Bibliography 4

5. CHAPTER 5 Summary & Outlook

5.1. Summary

5.1.1. Correlative Microscopy

5.1.2. *Operando*

5.1.3. Impact

5.2. Outlook

5.2.1. Today's Limitations

5.2.2. On-going work

5.2.3. Future Work

Bibliography 5

Curriculum Vitae

Acronyms and Abbreviations

2D ... Two-dimensional

3D ... Three-dimensional

AC ... Alternating current

AEM ... Analytical electron microscopy

AFM ... Atomic force microscopy

Al ... Aluminium

Al₂O₃ ... Aluminum oxide

AM ... Active material

Ar ... Argon

ASSB ... All-solid-state battery

at.-% ... Atomic percentage

B ... Boron

Be ... Beryllium

C ... Carbon

CAM ... Cathode active material

CC ... Constant current

CCD ... Charged-coupled device

c-LLZO ... Cubic LLZO

CO₂ ... Carbon dioxide

CPE ... Constant phase element

Cs ... Caesium

CT ... Computer tomography

CV ... Cyclic voltammetry

DC ... Direct current

DFT ... Density-functional theory

DLR ... Deutsches Zentrum für Luft- & Raumfahrt (German Aerospace Center)

e ... Electron

e.g. ... Exempli gratia

EASE ... European Association for Storage of Energy

EDX ... Energy dispersive X-ray spectroscopy
EIS ... Electrochemical impedance spectroscopy
EMIRI ... Energy Materials Industrial Research Initiative
ETIP ... European Technology & Innovation Platform
EUCAR ... European Council for Automotive R&D
FIB ... Focussed ion beam
FOV ... Field of view
Ga ... Gallium
Gb ... Grain boundary
Gd₂O₂S ... Gadolinium oxysulfide
GFIS ... Gas-field ion source
GIS ... Gas injection system
H ... Hydrogen
H₂O ... Water
HCl ... Hydrogen chloride
He ... Helium
i.e. ... Id est
ICON ... Imaging with Cold Neutrons
ICPIS ... Inductively coupled plasma ion source
IGTS ... Inert gas transfer system
IR ... Infra-red
JRC ... Joint Research Centre
Kr ... Krypton
La ... Lanthanum
LaB₆ ... Lanthanum hexaboride
LaO ... Lanthanum oxide
LCO, LiCoO₂ ... Lithium cobalt oxide
LCSM ... Laser confocal scanning microscopy
Li ... Lithium
LIB ... Lithium ion batteries
LiF ... Lithium Fluoride
LiNiCoAlO₂, NCA ... Lithium-Nickel-Cobalt-Aluminium-Oxide

LIPON ... Lithium Phosphorus OxyNitride
Li-S battery ... Lithium sulphur battery
LISICON ... Lithium Super Ionic CONductor
LLZO, $\text{Li}_7\text{La}_3\text{Zr}_2\text{O}_{12}$... Lithium lanthanum zirconium oxide
LLZO:Al,Ta , $\text{Li}_{6.45}\text{Al}_{0.05}\text{La}_3\text{Zr}_{1.6}\text{Ta}_{0.4}\text{O}_{12}$... Lithium lanthanum zirconium oxide doped with Ta and Al
LMIS ... Liquid metal ion sources
LSM ... Layered synthetic microstructure
m w.e. ... Metres water equivalent
Mg ... Magnesium
N ... Nitrogen
 n^0 ... Neutron
 n^0 im. ... Neutron imaging
Na ... Sodium
nanoCT ... Nano computed tomography
NASICON ... Sodium (Na) Super Ionic CONductor
Ne ... Neon
NiM ... Nickel metal hydride
 O_2 ... Oxygen
octa. ... Octahedral
OD ... Optical density
ORR ... Oxygen reduction reaction
PET ... Pentaerythritol
ppm ... Parts per million
PSI ... Paul Scherrer Institute
PV... Photovoltaics
QR ... Quick response
R ... Resistance
ROI ... Region of interest
SAED ... Selected area electron diffraction
SDD ... Source-to-detector distance
SDTrimSP ... Static and Dynamic Trim for Sequential and Parallel computer

SE ... Solid electrolyte
SEI ... Solid electrolyte interface
SEM... Scanning electron microscopy
SET plan... Strategic Energy Technology Plan
SI ... Secondary ion(s)
Si ... Silicon
SiC ... Silicon carbide
SIMS ... Secondary ion mass spectrometry
SOD ... Source-to-object distance
SRIM ... The Stopping and Range of Ions in Matter
SSB ... Solid-state batteries
SSLB ... Solid-state lithium batteries
STEM ... Scanning transmission electron microscopy
SY ... Sputtering yield
Ta ... Tantalum
TAP ... Thallium acid phthalate
Tb ... Terbium
TEM ... Transmission electron microscopy
tetra. ... Tetrahedral
Ti ... Titanium
t-LLZO ... Tetragonal LLZO
TOF ... Time of flight
TOF-SIMS ... Time-of-Flight Secondary Ion Mass Spectrometry
TRIM ... Transport of Ions in Matter
vol.% ... Volumetric percentage
WDXS ... Wavelength-dispersive X-ray spectroscopy
WMO ... World Meteorological Organization
Xe ... Xenon
XPS ... X-ray photoemission spectroscopy
XRD ... X-ray diffraction
Zr ... Zirconium
 μ CT... Micro computed tomography

Abstract

Energy storage systems i.e. batteries represent complex systems in which many factors interact in a dynamic interplay during operation. To design better batteries, a deep understanding of the operational state is key, however, by using traditional analysis methods, this is very challenging and often not feasible.

This work presents the development and optimization of advanced correlative microscopy workflows for chemical and structural analyses of battery materials with nanometer scale resolution and dopant level sensitivity. Advanced characterization techniques have been developed and applied to investigate bulk & interfaces, making it possible to study degradation artefacts as a function of life cycle, hence linking battery performance with underlying structural and chemical processes.

First, the development of a correlative *operando* approach pushes the limits of the present analytical capabilities beyond state-of-the-art. At different states of discharge correlative high-resolution high-sensitivity methods based on electron and ion-beam analytical techniques (SEM/SIMS) are used to study battery evolution and degradation as a consequence of cycling. The presented workflows target to establish fundamental understanding of the complex interplay between interface properties, microstructural appearance, chemical composition and their impact on electrochemical performance.

While correlative SEM/SIMS can be very powerful when studying Li-ion battery materials, it is a pure surface sensitive technique (for structural and chemical analysis), hence X-ray based analysis can serve as complementary technique. For example, μ CT is used to reconstruct 3D volumes of LLZO samples to study porosities, and nanoCT (high resolution XCT inside a SEM) in combination with SIMS is used to study cathodic material. Additionally, a correlative WDXS and SIMS approach is demonstrated to investigate the complex 3D solid-electrolyte-cathode interface (LLZO/LCO). These examples prove that X-ray based techniques can be an excellent complementary technique to SEM/SIMS, opening doors for many interesting studies including 3D bulk information (nanoCT & μ CT), or for chemical quantification (WDXS & XPS). On top of that, the combination of X-ray based techniques with SIMS allows to study all components of an all-solid-state battery from the anode through solid electrolyte to the cathode.

The final experimental chapter demonstrates an *operando* workflow correlating microstructure and chemistry, by transmission, as well as surface-sensitive techniques. The *operando* experiment is performed under neutron irradiation (transmission 2D & 3D) and subsequent SEM/SIMS analysis (surface-sensitive) is used for high-sensitivity, high-resolution analysis of degradation products. The complementary datasets aim a direct correlation between microstructural, chemical composition as well as electrochemical performance.

In this work we study solid-state batteries, focussed on LLZO to analyse and understand the evolution of degradation artefacts such as mechanical degradation, dendrite formation, transition metal diffusion and parasitic reactions. This combined with studying anode (here Li), cathode materials (here LCO) and the solid electrolyte-electrode interphase presents a

powerful technique for multidimensional data acquisition (structure, chemistry & electrochemistry). By designing innovative and useful ways of analysing batteries in multiple length scales (nano- to micrometer), we can accelerate the progress of battery technologies which play a crucial role in the upcoming global energy transition.

Kurzzusammenfassung

Energiespeichersysteme, d.h. Batterien, stellen komplexe Systeme dar, in denen viele Faktoren während des Betriebs in einem dynamischen Zusammenspiel interagieren. Um bessere Batterien zu entwerfen, ist ein tiefes Verständnis des Betriebszustands entscheidend. Dies ist jedoch mit herkömmlichen Analysemethoden oft herausfordernd oder nicht möglich.

Diese Arbeit stellt die Entwicklung und Optimierung fortschrittlicher korrelativer Mikroskopie-Workflows für chemische und strukturelle Analysen von Batteriematerialien vor. Fortgeschrittene Charakterisierungstechniken wurden entwickelt und angewendet, um sowohl Volumen (e.g. 3D) als auch die Grenzflächen zu untersuchen. Dadurch wird es möglich, Degradationsartefakte im Laufe des Lebenszyklus zu untersuchen und somit die Leistung der Batterie mit den zugrunde liegenden strukturellen und chemischen Prozessen zu verknüpfen.

Zunächst wird die Entwicklung eines korrelativen *operando*-Ansatzes vorgestellt und im Anschluss wird ein Konzeptnachweis mit einer symmetrischen Feststoff Halbzelle durchgeführt. Hierbei werden in verschiedenen Entladezuständen korrelative hochauflösende, hochsensible Methoden auf der Basis von Elektronen- und Ionenstrahlanalysetechniken (SEM/SIMS) verwendet, um die Entwicklung und Degradation der Halbzelle als Folge des Zyklus zu untersuchen. Die vorgestellten Workflows zielen darauf ab, ein grundlegendes Verständnis des komplexen Zusammenspiels zwischen den Eigenschaften der Grenzfläche, der Mikrostruktur, der chemischen Zusammensetzung und deren Auswirkungen auf die elektrochemische Leistung zu etablieren.

Während korrelative SEM/SIMS sehr leistungsfähig sein kann, wenn es um die Untersuchung von Li-Ionen-Batteriematerialien geht, handelt es sich um eine rein oberflächensensitive Technik (für Struktur- und chemische Analysen). Daher können Röntgenstrahlen basierende Analyse als ergänzende Technik dienen. Zum Beispiel wird μ CT verwendet, um 3D-Volumina von LLZO-Proben zu rekonstruieren zur Untersuchung dessen Porosität, und nanoCT (hochauflösendes XCT in SEM integriert) in Kombination mit SIMS wird zur Untersuchung von Kathoden Material verwendet. Darüber hinaus wird eine korrelative WDXS- und SIMS-Methode vorgestellt, um die komplexe 3D-Festelektrolyt-Kathoden-Grenzfläche (LLZO/LCO) zu untersuchen. Diese Beispiele zeigen, dass auf Röntgenstrahlen basierende Techniken eine ausgezeichnete ergänzende Methode zu SEM/SIMS darstellen können und Türen für relevante Studien ermöglichen. Darüber hinaus ermöglicht die Kombination von Röntgenstrahlen basierten Techniken mit SIMS, alle Komponenten einer Festkörperbatterie vom Anodenmaterial über den Festelektrolyten bis zur Kathode zu untersuchen.

Das letzte experimentelle Kapitel zeigt einen *operando*-Workflow, der Mikrostruktur und chemische Zusammensetzung durch Transmission sowie oberflächensensitive Techniken analysiert und korreliert. Das *operando*-Experiment wird unter Neutronenbestrahlung (Transmission 2D & 3D) durchgeführt, und anschließend wird eine SEM/SIMS-Analyse (oberflächensensitiv) für hochauflösende Analysen von Degradationsprodukten verwendet.

Die ergänzenden Datensätze zielen auf eine direkte Korrelation zwischen mikrostruktureller, chemischer Zusammensetzung sowie elektrochemischer Leistung ab.

In dieser Arbeit untersuchen wir LLZO-basierte Festkörperbatterien, um die Entwicklung von Degradationsartefakten sowie mechanischer Degradation, Dendritenbildung, Diffusion von Übergangsmetallen und parasitären Reaktionen zu analysieren und zu erforschen. Dies in Kombination mit der Untersuchung von Anodenmaterial (hier Li), Kathodenmaterialien (hier LCO) und der Festelektrolyt-Elektroden-Grenzfläche stellt eine leistungsfähige Technik für die multidimensionale Datenerfassung (Struktur, Chemie & Elektrochemie) dar. Durch die Entwicklung innovativer und nützlicher Methoden zur Analyse von Batterien in unterschiedlichen Größenordnungen (Nano- bis Mikrometer) können wir den Fortschritt von Batterietechnologien beschleunigen.

Preface

This thesis was carried out at the Luxembourg Institute of Science and Technology (LIST) in the Materials Research and Technology (MRT) Department within the AINA group (Advanced Instrumentation for Nano-Analytics). The thesis is affiliated at the Doctoral Program in Materials Science at the University of Stuttgart under the supervision of Prof. Dr. Dr. h.c. Guido Schmitz, and Dr. habil. Santhana Eswara. The thesis supervision committee consisted of Prof. Dr. Dr. h.c. Guido Schmitz, Dr. habil. Santhana Eswara, and Prof. Dr. Joris van Slageren. This PhD project was supported by the Luxembourgish National Research Fund (FNR) through the grants INTER/MERA/20/13992061 under the interBATT project.

Short description of the interBATT project: In the context of the energy transition, batteries are a key technology to address the transformation of the energy system. Despite progress, Li-ion batteries still have safety concerns and performance gains are limited by materials and interface constraints. The interBATT project aims to create material solutions for key interfaces, allowing to enhance energy density while maintaining safety and cycle life. Gained knowledge and promising solutions will ultimately be integrated into a larger prototype pouch-cell. interBATT drives the establishment of a European value-chain, spanning from fundamentals to battery cells.

The main role of LIST in this project was:

- 1) Development and optimization of sample preparation protocol for ion- and electron-beam analysis of battery materials and interfaces.
- 2) Adaptation and optimisation of correlative SIMS-based workflows.
- 3) Correlative data treatment and 3D visualization of multimodal datasets.

The work described in this thesis was disseminated at the following conferences and published in the following journals.

Conference participation

1. **MASSENA** Young Scientist Conference (YSC), Lipperscheid (Luxembourg), June 2021: [oral](#)
2. **Microscopy Conference** (MC2021), virtual, August 2021: [poster](#)
3. **European Materials Research Society** (EMRS) Spring Meeting 2022, virtual, May 2022: [oral](#)
4. **European Conference on Surface Science** (ECOSS35), Belval (Luxembourg), August 2022: [oral](#)
5. **PACE Young Scientist Conference** (YSC), Lipperscheid (Luxembourg), October 2022: [poster](#)
6. **Microscopy & Microanalysis** (M&M23), Minneapolis (USA), July 2023: [oral](#)
7. **74th Annual Meeting of the International Society of Electrochemistry** (ISE), Lyon (France), September 2023: [oral](#)
8. **Battery Innovation Days** (BID), Bordeaux (France), November 2023

Publication list

1. **Cressa, L.**; Sun, Y.; Andersen, D.; Gerard, M.; Castro, O. de; Kopljar, D.; Nojabae, M.; Friedrich, K. A.; Schmitz, G.; Wirtz, T.; Eswara, S. "Toward Operando Structural, Chemical, and Electrochemical Analyses of Solid-State Batteries Using Correlative Secondary Ion Mass Spectrometry Imaging." *Anal. Chem.* 2023, 95, 9932-9939
<https://doi.org/10.1021/acs.analchem.3c01059>
2. **Cressa, L.**; Fell, J.; Pauly, C.; Hoang, Q. H.; Mücklich, F.; Herrmann, H.-G.; Wirtz, T.; Eswara, S. "A FIB-SEM Based Correlative Methodology for X-Ray Nanotomography and Secondary Ion Mass Spectrometry: An Application Example in Lithium Batteries Research." *Microsc. Microanal.* 2022, 28, 1890-1895.
<https://doi.org/10.1017/S1431927622012405>
3. Ihrig, M.; Kuo, L.-Y.; Lobe, S.; Laptev, A. M.; Lin, C.-A.; Tu, C.-H.; Ye, R.; Kaghazchi, P.; **Cressa, L.**; Eswara, S.; Lin, S.-K.; Guillon, O.; Fattakhova-Rohlfing, D.; Finsterbusch, M. "Thermal Recovery of the Electrochemically Degraded LiCoO₂/Li₇La₃Zr₂O₁₂:Al,Ta Interface in an All-Solid-State Lithium Battery." *ACS Appl. Mater. Interfaces* 2023, 15, 4101-4112.
<https://doi.org/10.1021/acsami.2c20004>
4. Andersen, D.; Chen, H.; Pal, S.; **Cressa, L.**; Castro, O. de; Wirtz, T.; Schmitz, G.; Eswara, S. "Correlative high-resolution imaging of hydrogen in Mg₂Ni hydrogen storage thin films." *Int. J. Hydrog. Energy* 2023, 48, 13943-13954.
<https://doi.org/10.1016/j.ijhydene.2022.12.216>
5. Clausnitzer, M.; Ihrig, M.; **Cressa, L.**; Eswara, S.; Hein, S.; Finsterbusch, M.; Kuo, L.-Y.; Danner, T.; Latz, A. "Exploring Degradation Mechanisms at the Cathode/Electrolyte Interface of All-Solid-State Batteries: Insights from Structure-Resolved Simulations" *ACS Appl. Mater. Interfaces* 2023 (Submitted)
6. Shaplov, A.; xxx, H.; xxx, S.; **Cressa, L.**; xxx, O. de; xxx, T.; xxx, G.; xxx, S. "Li surface on polymer batteries." (In preparation)
7. Cressa, L.; Boillat, P.; Sun, Y.; Gerard, M.; De Castro, O.; Nojabae, M.; Schmitz, G.; Wirtz, T.; Eswara, S. "Operando neutron imaging and ex-situ correlative structural and chemical analysis of solid-state battery material" (In preparation)

Introduction

In the context of the climate and energy crisis it became clear that a transition from fossil fuels to renewable and sustainable alternatives is inevitable. The success of the upcoming energy transition relies on two main technological advancements: 1) energy harvesting technologies (e.g. photovoltaics (PV), wind turbines, ...) and 2) energy storage systems (e.g. batteries).

Battery research is blooming, and many innovative materials and technologies are being studied, however big breakthroughs are attenuated, and many questions remain unanswered to this day. One factor which decelerates the progress of battery technology is the fact that only a limited number of adapted and advanced analysis and characterisation methods exists. While there are many characterisation methods, only a few allow a contamination-free sample handling, additionally it is very challenging (& with some techniques not feasible at all) to analyse Lithium, which is an essential component in many battery systems.

Complex systems like batteries need to be analysed by multiple techniques and in best case simultaneously to correlate information and finally get “the full picture”. During the operation of batteries many physical (e.g. charge transfer, diffusion, material expansion, ...) and chemical (solid electrolyte interphase (SEI) formation, dendrites, parasitic reactions, ...) processes occur and to fully understand the underlying processes, structural, chemical, as well as electrochemical analysis is needed.

While some researchers delivered already substantial contributions in the field of advanced battery analytics, more correlative analysis workflows are needed.

An additional challenge in battery analytics is that most studies focus on sporadic or only pre- & post-mortem analysis. However, for a deep understanding of the underlying processes, analysis under operation is required. In-situ and operando workflows are considered as state-of-the-art characterisation technology, allowing to study batteries under realistic and operational conditions, rather than under idealized or simplified conditions.

This thesis focusses on the development, and the proof-of-concept of innovative correlative, in-situ, and operando workflows for solid-state battery materials. Among the used techniques, we correlate structural (SEM, LCSM, μ CT, nanoCT), chemical (SIMS, EDX, WDXS, XPS, neutron imaging), crystallographic (XRD, TEM, SAED) and electrochemical methods (EIS, cycling).

Structure of the Thesis

The 1st chapter of this thesis starts with a brief summary about battery research and will focus on solid state batteries. In the following “analysis and characterization” of battery materials are discussed, as well as the main techniques (e.g. Scanning electron microscopy (SEM) / Secondary ion mass spectrometry (SIMS)) and approaches (correlative workflows, in-situ, operando) used in this work. The chapter ends with problem statements and the thesis objectives.

The 2nd chapter focusses on the design of an operando correlative SEM/SIMS workflow. Starting with a sample holder prototype design, explaining the challenges and requirements, and the final experimental configuration. In the following different electrochemical tests (with resistors, commercial batteries, and standard model samples) were performed for the validation of the prototype. A discussion on different sample preparation techniques is then followed by a proof of concept of the operando SEM/SIMS workflow.

In the 3rd chapter X-ray based correlative approaches (especially with SEM, SIMS, transmission electron microscopy (TEM) & selected area electron diffraction (SAED)) are presented. While micro computed tomography (μ CT) analysis is used to study the porosity of solid electrolytes, correlative nano computed tomography (nanoCT) is used to study cathode material structurally. Next energy dispersive X-ray spectroscopy (EDX) & wavelength-dispersive X-ray spectroscopy (WDXS) are used to quantitatively study the cathode LiCoO₂ (LCO)-Lithium lanthanum zirconium oxide (LLZO) interface and in combination with correlative SEM/SIMS, important hints were provided, supporting a study which is summarized in “Case Study”.

The 4th chapter is dedicated to the design and successful execution of an operando neutron imaging approach. An accepted proposal for neutron beam time at the Paul Scherrer Institute (PSI) enabled this advanced experiment. 2D neutron imaging was performed during battery operation and 3D tomography could be performed before and after the experiment. These results were complemented by post-mortem SEM/SIMS analysis revealing parasitic dendrite formations probably causing the observed short-circuit failure.

The 5th chapter provides an overall summary elucidating the impact of this and similar studies and ends with an outlook.

CHAPTER 1

Introduction

Structure of the Thesis

1. CHAPTER 1 Background
 - 1.1. Where we came from
 - 1.2. Battery Research Today
 - 1.2.1. Solid-State Batteries
 - 1.2.2. $\text{Li}_7\text{La}_3\text{Zr}_2\text{O}_{12}$
 - 1.2.3. Types of Li-accumulations in LLZO based batteries
 - 1.3. Analysis & Characterization
 - 1.3.1. Introduction to Correlative Microscopy & Spectroscopy
 - 1.3.2. Introduction to SIMS
 - 1.3.3. Introduction to In-situ & Operando
 - 1.3.4. Advanced Analysis
 - 1.4. Problem Statements
 - 1.5. Thesis Objectives
2. CHAPTER 2 Operando Correlative SEM/SIMS
3. CHAPTER 3 X-ray Based Correlative Approaches
4. CHAPTER 4 Operando Neutron Imaging
5. CHAPTER 5 Summary & Outlook

1. Background

1.1. Where we came from

During the time this thesis was done, uncountable headlines about climate change were dominating the world news and still are. The World Meteorological Organization (WMO) published in a “State of the Global Climate 2022”¹ an update on the current climate situation. Among their key messages they state:

- In 2022, the average global temperature was 1.15°C higher than the average temperature from 1850 to 1900, with a range of 1.02 to 1.28°C. The period from 2015 to 2022 ranked as the eighth warmest, among the instrumental records spanning 173 years.
- The rise in methane concentration from 2020 to 2021 marked a record-breaking annual increase.
- Roughly 90% of the heat energy retained in the climate system due to greenhouse gases is absorbed by the ocean. In 2022, the measurement of ocean heat content recorded a new highest level ever observed.
- In 2022, the global average sea level continued its upward trend, reaching an all-time high within the period covered by satellite altimeter records, which spans from 1993 to 2022.
- During the hydrological year 2021/2022, a group of reference glaciers saw an average mass balance decline of -1.18 meters in water equivalent (m w.e.). This decrease is significantly greater than the average decrease observed over the past decade.
- In East Africa, there has been a shortage of rainfall for five consecutive wet seasons, marking the longest such period in four decades. As of August 2022, approximately 37 million individuals were dealing with severe food shortages in the region, primarily due to the impact of the prolonged drought and other related challenges.
- Unprecedented rainfall during July and August resulted in widespread flooding in Pakistan. The floods caused a minimum of 1,700 deaths, impacted 33 million individuals, and forced nearly 8 million people to flee their homes.

- Exceptionally high temperatures during the summer impacted both China and Europe, with certain regions experiencing extreme heat combined with unusually dry conditions. The number of additional deaths attributed to the heat in Europe surpassed 15,000 in total, affecting Spain, Germany, the United Kingdom, France, and Portugal.

These eight statements elucidate the dramatic situation humanity is facing right now and that there is absolutely no doubt, that concrete actions must be taken to slow down and hopefully stop the climate crisis. From an optimistic point of view, there has never been so many actions in the right direction, speaking of sustainability, limiting CO₂ emissions, circular economy, “green energy”, ... However, many technologies struggle to catch up with the alarming pace of climate change.

Today, more than ever, humanity is relying on scientific and technological breakthroughs which will save millions of lives and protect nature. Research areas of energy harvesting, and energy storage are blooming, and a few breakthroughs could be seen over the last years. The certain transition from fossil fuels to green energy is inevitably related to the need for reliable and efficient energy storage systems e.g. batteries.

The current battery research is retarding due to a limited availability of advanced analysis and characterization techniques. I want to highlight the word “advanced”, because a plethora of techniques exist but most of them are not well adapted for battery research. Hence in this context, “advanced” is meant for correlative approaches combining multiple techniques, taking care of the demanding requirements which come with battery systems (controlled atmosphere) and, in best case under operating conditions.

1.2. Battery Research Today

To this day lead acid (49.9%) & Li ion batteries (LIB)(45.7%) are still dominating the market², however to support the global energy transition, next-generation batteries need better performance and improved safety. Several countries and associations have published roadmaps to push energy storage technologies, for instance : ETIP³⁻⁹, EASE¹⁰, EMIRI¹¹, EUCAR, implementation of the SET Plan Action 7¹², JRC¹³⁻¹⁶, China¹⁷, Finland¹⁸, India^{19,20}, Japan^{21,22}, and the USA²³.

While current commercial battery technologies are reaching their intrinsic energy density limits, new so-called next-generation battery technologies are emerging.

The status of current commercial batteries and selected future chemistries is summarised in Figure 1, which depicts the energy performance characteristics of the major rechargeable battery types²⁴⁻²⁷.

Many of them use cell chemistries which are fundamentally different from those used in commercial Li-ion batteries. Figure 1 shows common and novel battery chemistries and their approximate potential volumetric (x-axis) and gravimetric (y-axis) energy densities. Li-S batteries show the most promising gravimetric energy density and Li-air as well as solid-state batteries show the potential highest volumetric energy density. Hence those battery chemistries are among the most prominent ones for next-generation batteries (Figure 1), and will be briefly discussed below.

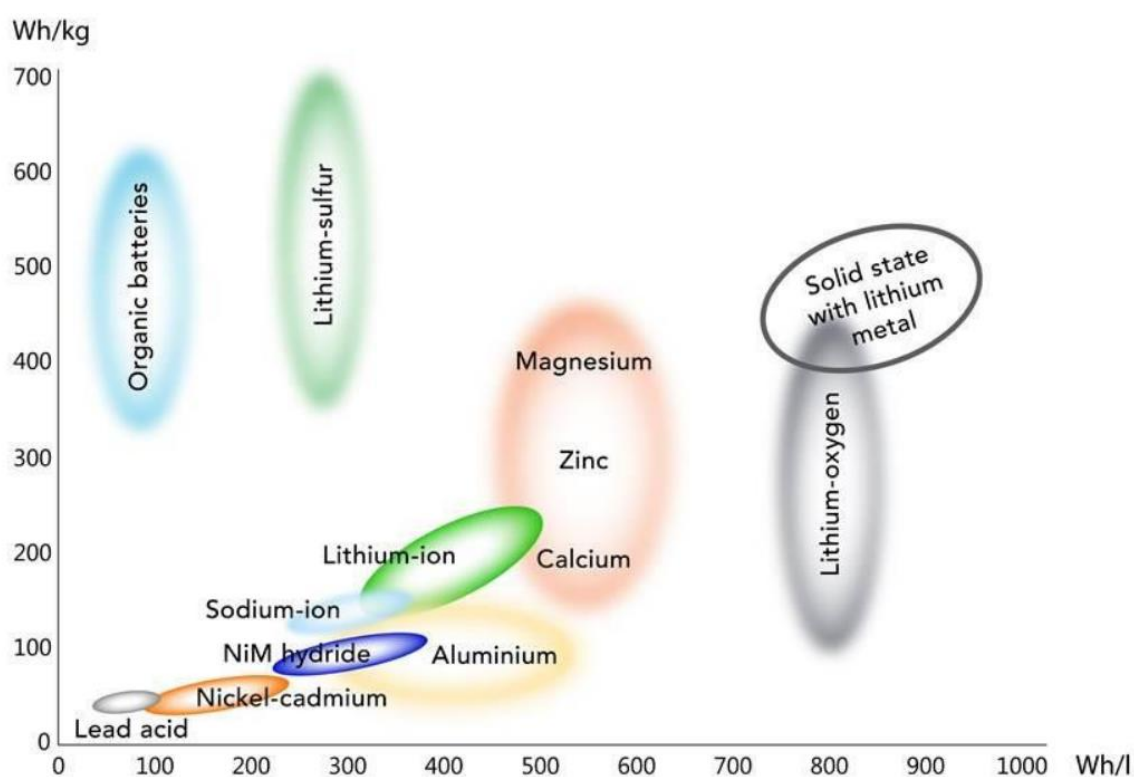


Figure 1: Current commercial batteries and targeted performance of future possible chemistries. The post lithium batteries chemistries are given as names indicating all kinds of metal-type batteries in respective category. There is a large uncertainty of their respective position in the graph. NiM hydride refers to nickel metal hydride. (Diagram taken from ²⁶)

For Li-S batteries the theoretical cell voltage is calculated as $E^\circ = 2.24 \text{ V}$ (vs Li/Li⁺) from the reaction enthalpy, in combination with a high gravimetric energy density (see Figure 1) the technology becomes attractive for commercial use.

Figure 2 shows a typical voltage profile (charging and discharging cycle) of a Li-S cell, while Figure 3 shows the simplified reaction from S⁰ to S²⁻, indicating the soluble and insoluble phases in organic solvent (e.g. ethylene carbonate (EC)/dimethyl carbonate (DMC) with the conducting salt LiPF₆).

The discharging process can be divided into three areas, as indicated in Figure 2. Area 1 of the discharge curve starts with the reduction of S_8 . The continuous decrease of the discharge curve is characterized by the formation of polysulfides such as Li_2S_8 & Li_2S_6 . The transition to Area 2 is characterized by a minimum and a continuous reduction of sulphur occurs. In Area 2 there is co-existence of high and low order polysulfides, while ideally a full transition from Li_2S_2 to Li_2S takes place at the end of discharging (Area 3).

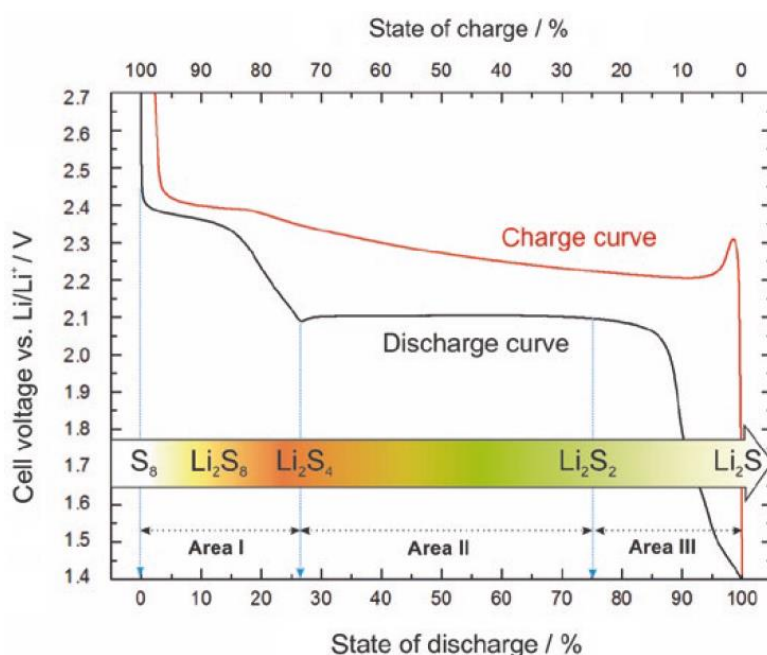


Figure 2: Typical voltage profile (charging and discharging cycle) of a lithium-sulphur cell.²⁶

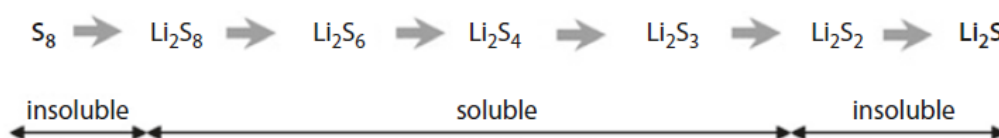


Figure 3: Cell reaction with several intermediate steps for the reduction of sulfur (S^0) to the sulfide ion (S^{2-}).²⁶

Up to now and in spite of many different approaches, Li-S cells could not be sufficiently improved to ensure satisfying cycling behaviour with respect to application parameters. Increased research and development efforts are therefore required to develop a mass-marketable Li-S cell.

Li-air batteries represent a completely different type of battery, with an open system - similar to fuel cells- where atmospheric O_2 participates in the cell reaction. The theoretical cell voltage is 2.96 V and high energy densities are to be expected with this cell concept. However, the current status quo of Li-air batteries, without a doubt still requires more fundamental research.

Figure 4 shows a simplified schematic of a Li-air cell (Li anode, electrolyte/separator, air cathode) and the discharge reaction at the air cathode.

Apart from Li-S and Li-air, solid-state batteries are also considered as promising cell chemistry for next generation batteries (Figure 1 "Solid state with Li metal"). Unlike traditional lithium-ion batteries, which typically use liquid or gel-like electrolytes, All-solid-state batteries (ASSBs) employ solid-state electrolyte with relatively good ionic conductivity. Main advantages of ASSBs are: 1) enhanced safety, the absence of flammable liquid electrolytes reduces the risk of thermal runaway, which can lead to fires or explosions and, 2) theoretical higher energy density.

As this thesis is mainly focussing on the advanced analysis and characterization of solid-state batteries, the following section will briefly introduce the state-of-the-art of solid-state battery technologies, before their analysis and characterization is introduced.

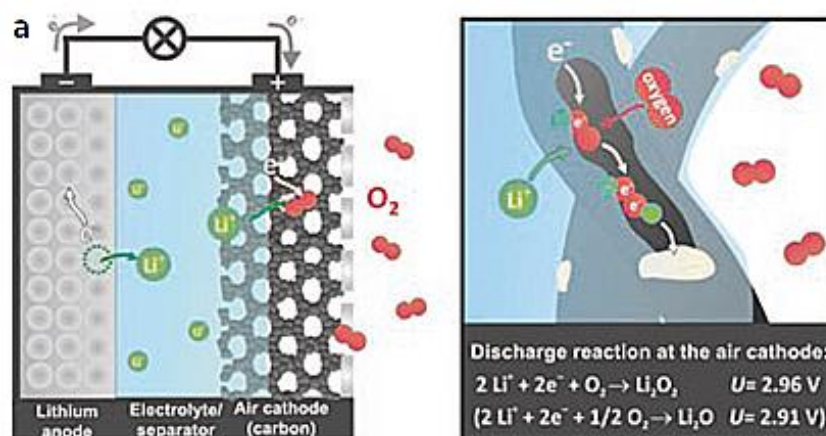


Figure 4: Schematic diagram of a lithium-air cell and electrode reaction for Li_2O_2 as the discharge product (oxygen reduction reaction, ORR).²⁶

1.2.1. All-Solid-State Batteries

Recent emerging developments involve the advancement of rechargeable solid-state batteries (SSBs). These batteries are sometimes referred to as "all-solid-state batteries" (ASSBs) or "solid-state lithium batteries" (SSLB) to emphasize that they are designed without the traditional liquid electrolyte. This chapter will focus on inorganic solid-state electrolyte chemistries and won't treat quasi-solid-state electrolyte or solid polymer electrolytes. Typically, solid electrolytes are composed of an inorganic solid with good ionic conductivity, high energy density²⁸ and good stability (ideally: thermal, mechanical, chemical and electrochemical). Different chemistries of solid electrolytes exist, e.g. oxides, sulfides, phosphates-based, crystalline structures (e.g. Lithium Super Ionic CONductor - LISICON, sodium (Na) Super Ionic CONductor -

NASICON, garnets), and glass ceramics (e.g. Lithium Phosphorus OxyNitride LIPON) count to the most promising ones.

Some very recent studies try to combine the advantages of multiple next generation cell chemistries, for instance H.-F. Wang et al.²⁹ summarize the “Fundamental Understanding and Construction of Solid-State Li-Air Batteries” in an impressive work. The paper discusses various materials and components used in constructing solid-state Li-Air batteries, exploring potential innovations and advancements, pointing out challenges and limitations associated with these batteries and propose strategies for addressing them.

1.2.2. $\text{Li}_7\text{La}_3\text{Zr}_2\text{O}_{12}$

In this work we will mainly study a garnet-type solid electrolyte namely lithium lanthanum zirconium oxide (LLZO, $\text{Li}_7\text{La}_3\text{Zr}_2\text{O}_{12}$). LLZO has two polymorphs: a cubic phase (c-LLZO) and a tetragonal phase (t-LLZO) (Figure 5). The blue parts represent the ZrO_6 octahedrons, and the orange dodecahedrons represent LaO_8 , the different Li sites are indicated by different colours (see legend in Figure 5). At room temperature, the cubic phase demonstrates approximately 100 times greater ionic conductivity, with a value of around $\sim 10^{-4}$ S/cm, compared to the tetragonal phase, which has a much lower ionic conductivity of approximately $\sim 10^{-6}$ S/cm.

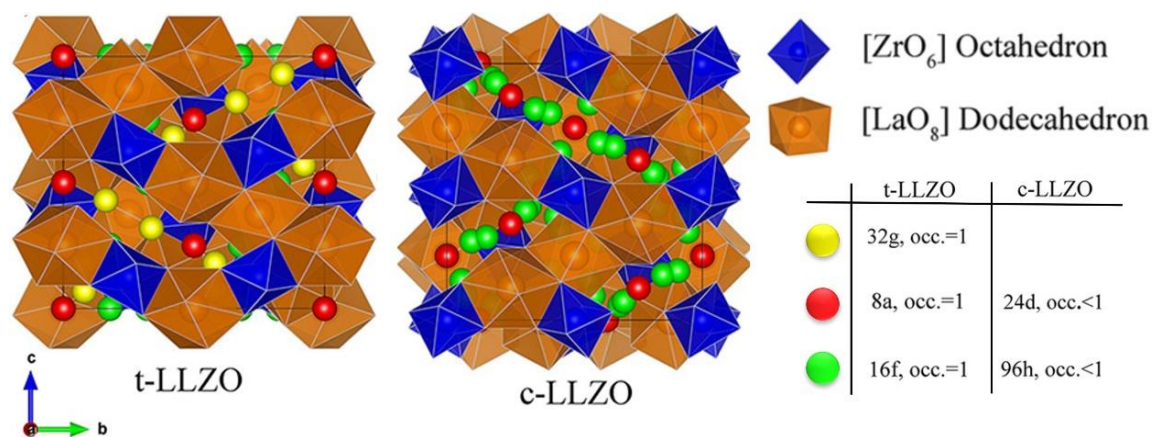


Figure 5: Crystal structure of tetragonal LLZO (t-LLZO), and cubic LLZO (c-LLZO) \rightarrow unit cell ($\text{Li}_7\text{La}_3\text{Zr}_2\text{O}_{12}$)₈. The different colors of the Li atoms (yellow, red, and green) represent the occupation of different sites. In t-LLZO yellow= 32g; red=8a; green= 16f; and in c-LLZO red=24d; green=96h. (taken and modified from ³⁰)

It is known from literature, that Al and Ta doping influences the Li^+ conductivity ³¹⁻³³, hence Chapter 3 focusses on the analysis of Al and Ta doped LLZO. Different parts of a SSB like for example the Li anode, the electrolyte LLZO or the cathode (either pure lithium cobalt oxide (LiCoO_2 - LCO) or LCO-based active materials (AM)) are analysed individually. However also, the interphases and the interplay between solid

electrolyte and either anode (Chapter 2 & 4) or cathode (Chapter 3) are studied. Figure 6 shows an exemplary schematic of an SSB, composed of an Li anode, an LLZO solid electrolyte and a cathode (here not specified for simplicity reasons). The three individual material pellets are illustrated in a), b) shows a side-view of an assembled SSB and c) shows an exemplary volume of the three layers. This exemplary volume will be used through the entire manuscript to discuss the analysis of the SSB.

All operando experiments (Chapter 2 & 4) were performed with a symmetric Li/LLZO/Li cell.

It is important to keep in mind that through the entire manuscript, the focus lies on the development of advanced correlative microscopy workflows rather than on the optimisation of the battery chemistry. Synthesis of the LLZO and cathode materials goes beyond the scope of this thesis. However, assembly, disassembly, and different kinds of sample preparation, being an essential part of the workflow described in this work have been performed by the author and are described in the individual chapters under “Sample preparation”.

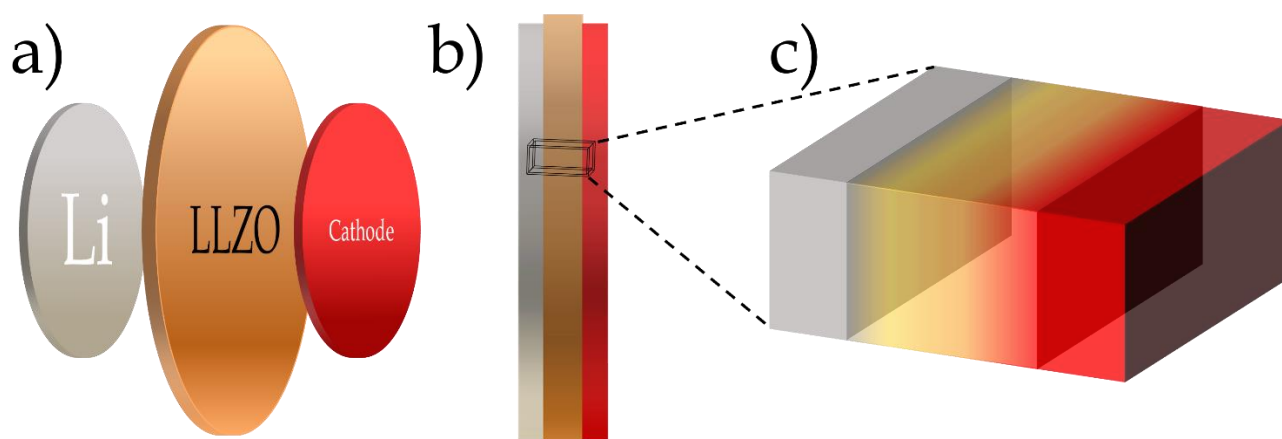


Figure 6: Exemplary schematic of a) the three individual material pellets (Li, LLZO, and cathode). b) a sideview of the assembled SSB, and c) an exemplary volume of the SSB.

1.2.3. Types of Li-accumulations in LLZO based batteries

One of the major degradation mechanisms in Li batteries is dendrite formation, often resulting in short-circuits. In this work (especially Chapter 2 and 4) we focus on the study of such degradations, hence an overview of different types of Li-accumulations are summarised in Table 1. While Frencck et al.³⁴ already investigated different factors that control the formation of different Li-accumulation morphologies, they mainly focussed on liquid and polymer electrolytes and hardly on inorganic solid electrolytes. For instance, they defined six different morphologies (whiskers, moss, dendrites, globules, trees, and cracks) with only one for solid electrolytes, which they call “cracks” and looks similar to the intergranular (or grain boundary) Li accumulations

we could observe (Chapter 2 & 4). They explained the nature of the different morphologies based on two main parameters namely, the shear modulus of the electrolyte and, the current density normalized by the limiting current density.

Kazyak et al.³⁵ studied Li penetration in ceramic solid electrolytes and identified four unique morphologies of dendrites, demonstrating that a singular mechanism is insufficient to describe the complexity of Li propagation pathways. They define and discuss four different morphologies namely: “straight”, “branching”, “spalling”, and “diffuse”. The “straight” type is defined by a subsurface Li plane with a linear path of propagation and intersecting the electrolyte surface as a linear crack. It also shows Li extruding out of the cracks at the surface as a result of the viscoplasticity of metallic Li. The second type “branching” is typified by the fact that the Li accumulations tend to branch and grow in multiple directions (contrary to the “straight” type).

The precise reason for the branching remains unclear. The “spalling” type was defined by a Li-filled crack, like the “straight” type, following a curved path instead of a straight one. When a crack forms a closed loop, the LLZO material at the centre becomes disconnected from the main body of the pellet, and unlike the “straight” and “branching” types, the “spalling” type does not correlate with a decrease in polarization and didn’t lead to short-circuit. The fourth type is called “diffuse” and Kazyak et al.³⁵ claim it to be fundamentally different from the other three types. This type seems to form a network of very thin structures and that are observed via SEM and optical microscopy as dark spots being Li dendrites. Based on the postmortem analysis, the “diffuse” type preferentially accumulates along grain boundaries and intergranular cavities.

Golozar et al.³⁶ could observe mossy, bumpy and needle-type structures of Li-accumulations. While mossy and needle-type structures could be observed by other researcher too; to our knowledge the bumpy type, with a large and chunky appearance haven’t been reported by other researchers so far.

Cheng et al.³⁷ reported Li-accumulations which Frenck et al.³⁴ later described as “cracks”. However, some observations of Cheng et al. fit quite well the description of the “straight” or “spalling” type defined by Kazyak et al.³⁵

Ren et al.³⁸ could observe Li-accumulations through grain boundaries and interconnected pores^{39,40}, which are difficult to classify between the different types, based on the published results.

CHAPTER 1

Table 1: Summary of different types of Li-accumulations within LLZO from literature.

AUTHORS	TYPES	MEDIUM	SIMPLE DESCRIPTION
Frenck et al. ³⁴	whiskers, moss, dendrites, globules, trees	Liquid/ polymer electrolyte	As not in solid electrolyte we will not discuss these types in detail.
	cracks	$\text{Li}_{6.25}\text{Al}_{0.25}\text{La}_3\text{Zr}_2\text{O}_{12}$	Li being “pressed” through LLZO grain boundaries (taken from ³⁷), web-like structure.
Kazyak et al. ³⁵	straight	$\text{Li}_7\text{La}_3\text{Zr}_2\text{O}_{12}$	Subsurface plane intersecting LLZO as a linear crack.
	branching	$\text{Li}_7\text{La}_3\text{Zr}_2\text{O}_{12}$	Crack with tendency to bifurcate as it grows, leading to a 3D branching structure.
	spalling	$\text{Li}_7\text{La}_3\text{Zr}_2\text{O}_{12}$	Growth of isolated structure in the bulk.
	diffuse	$\text{Li}_7\text{La}_3\text{Zr}_2\text{O}_{12}$	Network of very thin structures along grain boundaries.
Golozar et al. ³⁶	mossy	$\text{Li}_7\text{La}_3\text{Zr}_2\text{O}_{12}$	Large mossy Li -accumulations.
	needle	$\text{Li}_7\text{La}_3\text{Zr}_2\text{O}_{12}$	Large needles >5 μm diameter and >150 μm .
	bump	$\text{Li}_7\text{La}_3\text{Zr}_2\text{O}_{12}$	Large drop-like Li-accumulations.
Cheng et al. ³⁷	“straight” or “spalling”	$\text{Li}_{6.25}\text{Al}_{0.25}\text{La}_3\text{Zr}_2\text{O}_{12}$	Appearance like “straight” or “spalling” from ³⁵ .
	“cracks”	$\text{Li}_{6.25}\text{Al}_{0.25}\text{La}_3\text{Zr}_2\text{O}_{12}$	Li being “pressed” through LLZO grain boundaries, web-like structure.
Ren et al. ³⁸	“Interporous/ granular”	$\text{Li}_{6.75}\text{La}_3\text{Zr}_{1.75}\text{Ta}_{0.25}\text{O}_{12}$	Li accumulations through grain boundaries and interconnected pores.
Cressa et al. ⁴¹	“Intergranular/ diffuse”	$\text{Li}_7\text{La}_3\text{Zr}_2\text{O}_{12}$	Li being “pressed” through LLZO grain boundaries, “liquid” appearance.
Chapter 4 in this work	“whiskers”	$\text{Li}_7\text{La}_3\text{Zr}_2\text{O}_{12}$	Thin needles: length $\sim 7 \mu\text{m}$ and a diameter $< 0.3 \mu\text{m}$
	“mossy”	$\text{Li}_7\text{La}_3\text{Zr}_2\text{O}_{12}$	Looks like grown and entangled whiskers.
	“Intergranular/ diffuse”	$\text{Li}_7\text{La}_3\text{Zr}_2\text{O}_{12}$	Li being “pressed” through LLZO grain boundaries, “liquid” appearance.

In Chapter 2 we were able to study intergranular, “diffuse”-type morphology. And in Chapter 4, three types of Li-accumulations being: “whiskers”, “mossy”, and intergranular, “diffuse”-type morphologies are studied.

Having said all this, it becomes clear that there is not a unified way to categorize Li-accumulations. Frenck et al. and Kazyak et al. delivered impressive studies, by trying to bring order in the chaos; however, with new morphologies being observed by several researchers, confusion arises again as those morphologies don't fit in the already described categories. In Chapter 4 we are going to present a different way of categorizing different Li-accumulation types and we are going to propose a hypothesis which could explain the co-existence of different types (whiskers, mossy, and intergranular/diffuse) which were observed in this Chapter 4.

1.3. Analysis & Characterization

As described before, the analysis and characterisation of batteries is essential for their continuous development. In this subchapter, the principle of correlative microscopy (in general but also in relation to battery materials) will be discussed, followed by an introduction of SIMS, and a discussion about *in-situ* and *operando* approaches.

1.3.1. Introduction to Correlative Microscopy & Spectroscopy

Correlative microscopy and spectroscopy are performed on the same sample (sometimes even at the exact same region of interest (ROI)) and involve the application of multiple techniques, aiming to gather complementary data that enhances our understanding of the sample and its characteristics. In general, every analysis technique can be used in a correlative workflow (at least ex-situ). In this work however, we will focus on correlative workflows based on charged particle techniques e.g.: electron & ion microscopes, and SIMS in combination with a focussed ion beam (FIB).

Correlative microscopy & spectroscopy allows to acquire complementary data: i) structural: including morphology, porosity, structural dis-/order, homo-/heterogeneity, grain size & distribution, as well as ii) chemical: like chemical composition &/or distribution of chemical compounds, the presence of trace elements or dopants, and iii) physical: electrochemical analysis, impedance/resistance, pressure dependant factors, magnetism, optical properties.

While many scientists have shown already impressive advancements in the field of correlative microscopy⁴² only a few have optimised their workflows for the analysis of battery materials⁴³⁻⁴⁸.

This work focuses on the optimisation of correlative workflows especially for SSBs. As mentioned before, charged particle techniques play an essential role in this work, and while SEM is a very common and well-known technique, it will not be discussed in this introduction. On the other hand, SIMS being a less common technique will be described more in detail in the following subsection.

1.3.2. Introduction to SIMS

SIMS is a destructive, surface sensitive analysis technique, which involves accelerating ions towards a sample. At the impact secondary ions (SI) (and neutrals) are sputtered, which are being separated by their mass to charge ratio. This analysis technique allows different operational modes, allowing to gather different information: common mass spectrometry, 2- & 3D chemical imaging, and 1D depth profiling.

Typically, in SIMS one can distinguish between two modes depending on the primary ion dose. Static SIMS is typically operated with a pulsed ion beam in combination with a time-of-flight mass (TOF) spectrometer. And dynamic SIMS using a direct current (DC) is usually operated using a magnetic sector or quadrupole mass spectrometer for depth profiling or imaging applications. The SIMS used in this work represents a dynamic system with a magnetic sector mass spectrometer.

The general operation of SIMS can be divided into five main process steps: 1) Primary ion beam; 2) SI generation; 3) Collection of SIs; 4) Mass analyser; and 5) Detection.

1) Primary ion beam

The ion beam, generally a FIB can be generated with different elements (He^+ , Ne^+ , Ga^+ , Cs^+ , O^-) or clusters, hence they rely on different techniques to be generated. Among the most prominent ion sources are for instance, the gas-field ion source (GFIS) used for He, Ne, O beams; liquid metal ion sources (LMIS) for Ga, Li, Be, B, C, Si... ; and inductively coupled plasma ion source (ICPIS) mainly for inert gases (Xe, Kr, Ar, O, N, ...)⁴⁹.

When a primary ion beam is accelerated toward a sample, upon impact the material erodes due to the impact of highly energetic ions, leading to the expulsion of surface atoms, known as sputtering. Simultaneously, in the bulk the high energetic ions create a collision cascade i.e. a series of elastic collisions of primary ions and sample atoms, resulting in potential implantation of the primary ions and displacement of matrix atoms.

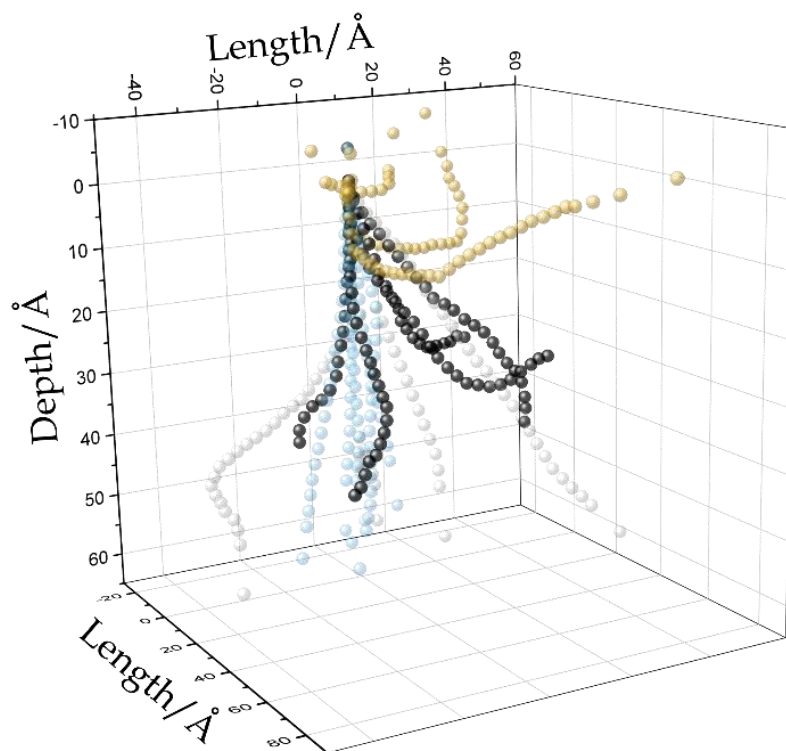


Figure 7: Three-dimensional illustration of ion and recoil trajectories obtained with SDTrimSP for Ga ions on a thin layer (50 Å) of elemental Si. Black balls represent trajectories of five Ga ions which got implanted into the bulk. Yellow balls are trajectories of five Si atoms that are being backward sputtered. Blue balls represent the trajectories of five forward sputtered Ga ions and the grey ones are five forward sputtered Si recoils.

Figure 7 illustrates the 3D trajectories of Ga ions in amorphous Si, elucidating different phenomena, for instance: the black balls represent trajectories of five ions which got implanted into the Si bulk; yellow balls are trajectories of five Si atoms that are being backward sputtered; blue balls represent the trajectories of five forward sputtered Ga ions and the grey ones are five forward sputtered Si recoil atoms. While the primary ions are travelling through the target material, energy loss processes of the primary ion are occurring and can be attributed to either electronic (energy loss/transfer to the electrons in the material) or nuclear (energy loss/transfer to the nuclei) stopping power.

Figure 8 shows the simulated stopping power as a function of the ion energy for Ga & Ne inside a pure amorphous Si matrix (generated via SRIM). The stopping power is given by its two components, the electronic stopping (red) and the nuclear stopping (blue), the black data points represent the total stopping power i.e. the sum of the two previous ones. Regarding Ga (Figure 8 a) the contribution of the nuclear stopping power is quite important, reaching a maximum value of approximately 113 eV/Å for an energy around 70 keV. Above 700 keV, the electronic stopping power will dominate the total stopping power.

On the other hand, for Ne (Figure 8 b) the nuclear stopping power dominates until an ion energy of approximately 50 keV, beyond that the electronic stopping power takes over. In the context of the analysis of battery materials usually a higher contribution of nuclear stopping power (e.g. Ga⁺) is preferred to obtain higher sputtering yields, which is preferential for SIMS analysis. On the other hand, a higher contribution of the electronic stopping power (e.g. Ne⁺) is related to higher lateral resolution, which is the main advantage in ion microscopes using a Ne⁺ or He⁺ source.

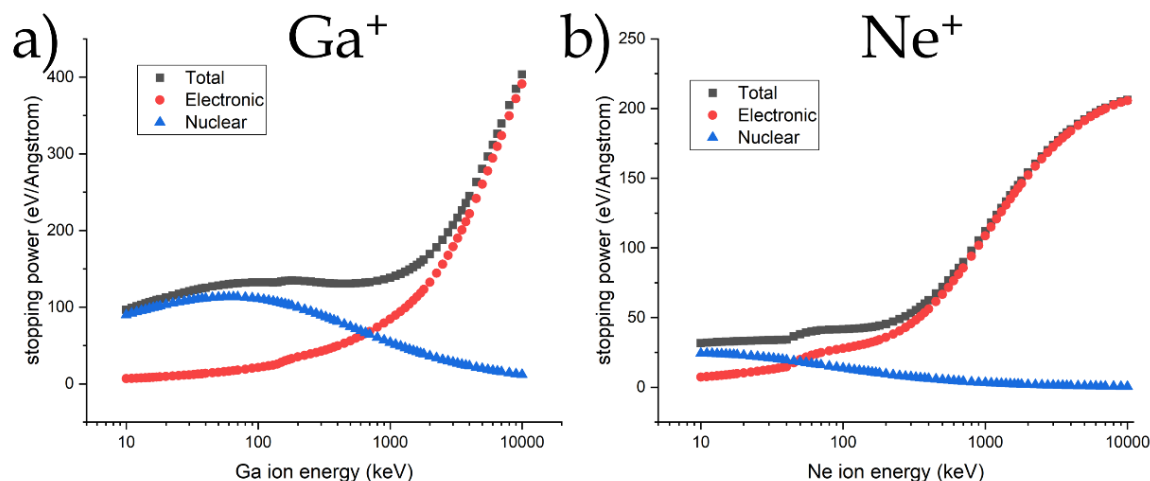


Figure 8: By SRIM calculated stopping power (eV/Å) as a function of the ion energy (from 10 keV to 10 MeV) a) for Ga⁺ and b) for Ne⁺, with Si (2.3 g/cm³) as target material. The electronic stopping power is plotted in red, the nuclear in blue and the total in black.

On the target surface and above typically, a mixture of neutrals, positively, negatively charged ions and combinations of small clusters are being sputtered simultaneously. Depending on the analysis mode either the positive or the negative ions can be analysed via SIMS.

2) SI generation

The SI generation depends on a multitude of factors: like primary ion species & energy, mass, irradiation dose, impact angle, ionization, target material. Based on Sigmund's theory⁵⁰ of sputtering it is possible to approximately calculate the sputtering yield (SY), which describes the number of sputtered atoms per incident ion.

Ionization happens upon a charge exchange interaction between the sputtered atom and the surface. The ionization yield is strongly influenced by matrix effects i.e. the significant influence of sputter & ionisation phenomena by the chemical surrounding of the region of interest (ROI), even within a single material containing diverse atomic species.

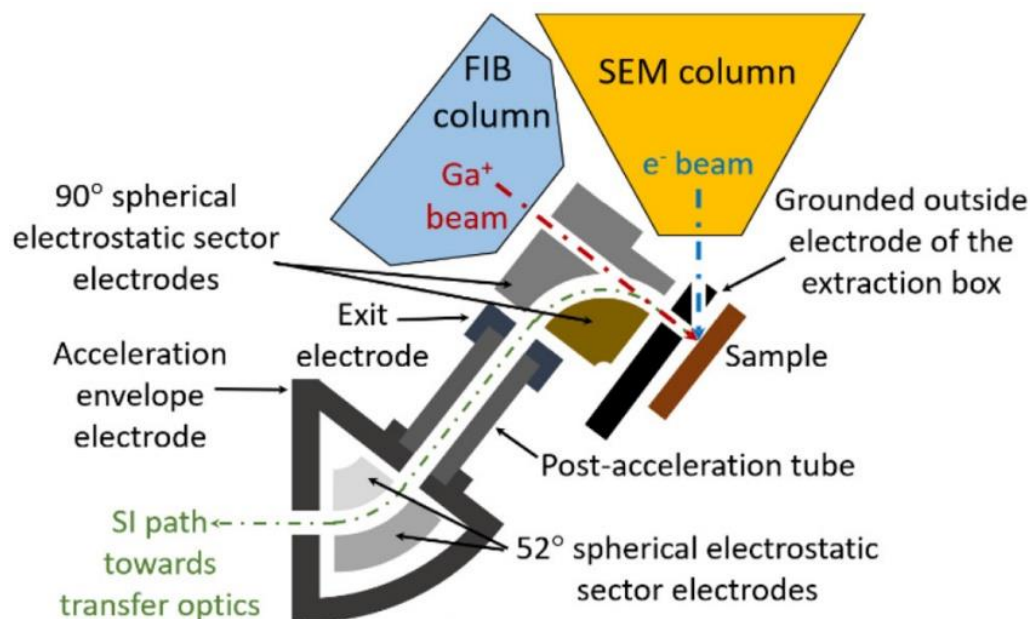


Figure 9: Schematic layout of the extraction box region close to the sample/column end nozzle area, post acceleration region, and second 52° bending electrostatic sector. (Schematic taken with permission from ⁵¹)

3) Collection of SIs

The collection of SIs is performed via an extraction system, illustrated in Figure 9 (details described elsewhere^{52,51}). The secondary ion extraction box is placed in-between the ion source and the target material. A tiny hole allows the primary ions to travel through the extraction box. During the SIMS operation, the extraction box is placed very close to the sample (~0.5 mm), and the sample is biased to +500 V for positive and -500 V for negative SI extraction, respectively. The electric field created by the sample bias potential and the grounded first electrode of the extraction box is responsible for the SI extraction.

After post-acceleration of the SIs, a specialized transfer optics system, composed of three lenses and four quadrupole deflectors, subsequently conveys the SIs to the mass analyser.

4) Mass analyser

Subsequently the SI beam enters the magnetic sector, where the beam consisting of many different (either positive or negative) ions, get separated regarding the mass to charge ratio of the individual ion species. The used system shows a mass resolving power ($M/\Delta M$) of ~400 with an overall transmission of above 40%.

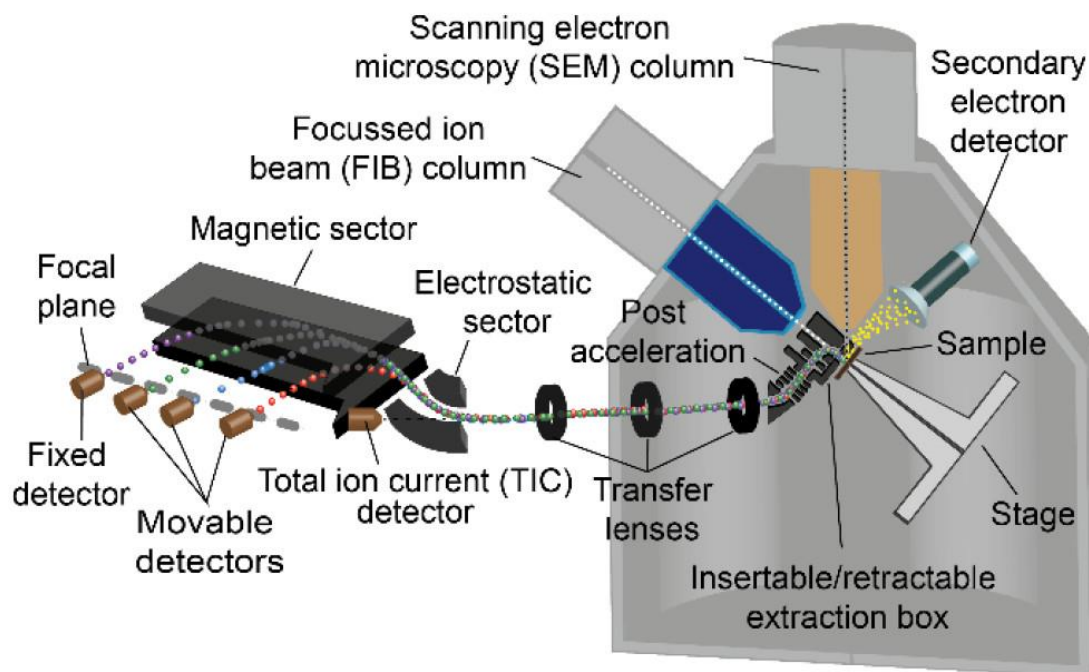


Figure 10: Schematic layout of the FIB-SEM-SIMS instrument. (Schematic taken with permission from ⁵¹)

5) Detection

Three types of mass analysers are very common in SIMS: the quadrupole, the time-of-flight, and the magnetic sector. The SIMS systems used in this work are equipped with a magnetic sector detection system. The detection of the physically separated ions can be performed either with individual (movable) detectors which are positioned on the focal plane, this allows the detection of multiple (limited to number of detectors) masses simultaneously. On the other hand, a focal plane detector which is composed of multiple micro channel plates enables the simultaneous detection of all elements of the periodic table.

Figure 10 shows a schematic of the SEM/SIMS system used in this work. It is based on a Thermo Fisher Scios DualBeam FIB-SEM equipped with an in-house developed double-focusing magnetic sector SIMS system, which allows the detection of four masses in parallel. The FIB consists of a gallium liquid metal ion source producing $^{69}\text{Ga}^+$ primary ions. The SEM column is vertically arranged, and the FIB column is at a fixed angle of 52° relative to it. The sample stage can be moved in three dimensions and can also be tilted and rotated as needed, allowing a high degree of flexibility. The extraction optics of the SIMS is inserted (between FIB nozzle and sample stage see Figure 9) for analysis, allowing high SI extraction (Figure 9 & Figure 10). The system can be used to generate mass spectra, 2D & 3D chemical imaging, and depth profiling,

enabling high-resolution high-sensitivity correlative analysis. Further details on the SIMS system can be found elsewhere.^{52,51}

Drawbacks of the SIMS system is its destructive nature. During analysis the sample surface is altered due to sputtering, however simple simulations (SRIM⁵³ - Stopping and Range of Ions in Matter) can help to estimate the degree of damage caused (see Chapter 2). Sub-surface alteration is dominated by ion implantation and intermixing of bulk-atoms, which can be limited by optimising experimental parameters. Another disadvantage is the matrix effect making quantitative studies very challenging.

The main advantages of dynamic SIMS in relation of this work are: 1st in combination with SEM correlative, structural and chemical analysis is possible. 2nd all elements are analysable including Li which is essential when studying batteries. 3rd a high sensitivity (dopant-level) and high-resolution (nanometer scale) is achieved. 4th as the SIMS used in this work is a compact add-on, the flexible microscope design is very versatile and ideal to integrate in-situ and/or operando modalities.

1.3.3. Introduction to *In-situ* & *Operando*

"In situ" is a Latin phrase that translates to "in its original place" or "on-site" in English. In scientific research it is referred to experiments or observations that are performed at the actual location or under specific conditions of interest, without the need to remove or alter the subject under study.

Interconnected physical, chemical, and structural processes occurring during operation of complex systems e.g. batteries, solar cells, and fuel cells, require in situ analysis. Several researchers have developed innovative in-situ experiments for instance, T. Liu et al.⁵⁴ studies the solid electrolyte interphase (SEI) formation on graphite anodes through correlative atomic-scale microscopy with different in-situ and operando techniques. They were able to characterize the formation process of the SEI on graphitic electrodes at the nanoscale in an impressive work. This approach however is focussed on liquid electrolyte battery systems.

While L. Xue et al.⁵⁵ summarizes recent applications of in-situ/operando Raman techniques for studying real-time variations in Li-S batteries to reveal the reaction mechanism; Z. Yu et al.⁵⁶ explores a novel method for gaining insights into the sulphur redox reactions within Li-S batteries, by employing an in-situ correlative electrochemistry and mass spectrometry approach.

The manuscript from A.M. Tripathi et al.⁵⁷ intensively reviews and discusses various in-situ techniques for studying battery interfaces. They emphasize in-situ spectroscopic techniques (e.g. infra-red (IR), Raman, X-ray) for chemical studies and

highlight how these techniques can help identify the formation and composition of SEI. Regarding morphological and structural studies on battery interfaces, A.M. Tripathi et al. emphasizes SEM and transmission electron microscopy (TEM) (and atomic force microscopy (AFM)) as they can provide valuable insights into the physical changes during cycling. Optical, gravimetric, scanning probe-, neutron- & magnetic-based are also reviewed in this overall complete work. Furthermore, the importance of diverse electrochemical experiments (e.g. Cyclic voltammetry (CV), Electrochemical impedance spectroscopy (EIS), cycling, ...) are highlighted and the authors discuss the significance of *operando* techniques, which combines multiple analytical methods with battery operation to provide a comprehensive understanding of battery interfaces.

"Operando" is a scientific term used to describe a methodology where an experiment or analysis is conducted under realistic and operational conditions, such as during the operation of a device, rather than under idealized or simplified conditions. The main goal is to study the behaviour of materials and systems during actual operation.

For instance, Masuda et al.⁵⁸ introduced a ground-breaking technique using in situ time-of-flight secondary ion mass spectrometer (TOF-SIMS) imaging to analyse SSBs. However, their approach did not account for potential interference between battery cycling and the analysis process.

Mathayan et al.^{59,60} employed *operando* elastic recoil detection analysis and Rutherford backscattering spectrometry to investigate the transport of lithium and oxygen. However, their methodology was limited to ultra-thin batteries with a maximum thickness of a few micrometres, and it failed to capture changes in the microstructure of the batteries.

Otoyama et al.⁶¹ employed an innovative approach by utilizing *operando* confocal microscopy to observe structural changes in SSBs. However, the spatial resolution of optical microscopes restricts their observations to large μm -range, and they lacked a chemical characterization method.

Yamagishi et al.⁶² developed a highly promising *operando* TOF-SIMS technique for studying SSBs, enabling the dynamic tracking of lithium distribution in the graphite anode during battery operation. Their study covered relatively large areas ($>100 \mu\text{m}$) and focused specifically on the anodic side's lithium distribution. The fundamental principle of TOF-SIMS unavoidably requires pulsing the primary (or secondary) ion beam, which creates a duty cycle. As a consequence, the time taken to acquire images (given a specific number of SIs per pixel) is significantly longer compared to the imaging method used in magnetic sector SIMS. Magnetic sector SIMS employs a DC beam with no duty cycle. Additionally, magnetic sector SIMS offers better extraction

efficiency and overall transmission, leading to superior detection limits in comparison to TOF-SIMS.

1.3.4. Advanced Analysis

As mentioned, “Advanced Analysis” in the context of battery research covers a multitude of functions and takes care of all the necessary requirements:

Table 2: Essential requirements which are necessary for advanced analysis of air- and moisture-sensitive samples.

Essential requirements	
	Contamination-free:
1.	preparation of battery materials (e.g. LLZO)
2.	assembly of half-cells, batteries, ...
3.	macro- & microscopic sample preparation (e.g. cross-section, lamella, ...)
→	through controlled atmosphere (inert gas or vacuum) due to moisture and oxygen sensibility of many battery components.

Table 3: Different analysis types which can be combined and ideal options for each type.

	Analysis	Ideal Options
a.	Structural analysis	mm- to nm-scale
b.	Chemical analysis	Quantitative & qualitative
c.	Crystallographic analysis	Globally and localised
d.	Electrochemical analysis	In-Situ & Operando

Table 2 shows essential requirements which need to be fulfilled to perform correlative analysis approaches. If one of those requirements are not satisfied, advanced analysis of batteries is not feasible. Table 3 enumerates the different types of analysis and characterization which can be performed. For instance, structural, chemical, crystallographic, and electrochemical analysis. The right side of the table mentions ideal options for every analysis type. We consider as “Advanced Analysis” every approach which fulfils the three essential requirements (Table 2), and which combines at least two of the four listed analysis types (Table 3). Every additional analysis increases the quality of the study and could provide an essential piece of the puzzle. Every idealized option which is included in the workflow valorises the study even more and results -to this day- in a unique correlative workflow.

1.4. Problem Statements

Battery research has never been more important than it is today, and it is only a matter of time until next-generation battery technologies will make the transition from lab-

scale to large-scale industrial production. However, a few factors are slowing down this transition, we identified five limiting factors of battery research e.g.:

- i. One decelerating factor is the **limited availability of advanced analysis and characterization workflows**, allowing to get a deep understanding of the underlying processes in battery systems.
- ii. The fact that many **physical and chemical phenomena** take place during a battery's operation, **demands correlative analysis** approaches to study multiple interconnected processes.
- iii. Most conventional characterisation techniques are barely, or not at all able **to analyse low-Z elements such as Li**, which is an essential element of batteries compositions.
- iv. Apart from structural and chemical analysis, electrochemical analysis is essential as it is the dominant factor revealing the batteries performance. Ex- & In-situ analysis is often insufficient to draw conclusions, hence **scientists agree that *operando* workflows are needed**.
- v. Necessity of structural analysis **over multiple length scales** (from mm- to nm-scale) and chemical analysis with **high resolution and high sensitivity**.

The order of the five problem statements does not reflect their significance.

1.5. Thesis Objectives

Based on the five problem statements mentioned before, we defined thesis objectives in order to assist and accelerate battery research, hence pushing toward a faster transition from lab to real world application.

- i. Design of **workflows optimised for battery analysis**, while ensuring enough flexibility to study a variety of battery systems and not be limited to one very specific sample type. This increases the offer and availability of such complex workflows.
- ii. **Combine multiple complementary techniques** (correlative approaches) to be able to draw conclusions based on interconnected phenomena e.g. pressure-impedance relation, cycling-dendrite formation, degradation-transition metal diffusion, ...
- iii. **Chemical analysis of** relevant elements including **lithium**, which is an essential component in LIB, via SIMS (qualitative) and neutron imaging (quantitative).

CHAPTER 1

- iv. **Implementation of *operando* capabilities in correlative workflows**, allowing to study batteries under operational conditions rather than under idealised static conditions.
- v. Using techniques allowing **high resolution and dopant-level sensitivity**, as well as studying **multiple length scales (mm to nm)**.

References

- (1) World Meteorological Organization (WMO). *State of the Global Climate 2022* (<https://public.wmo.int/en/our-mandate/climate/wmo-statement-state-of-global-climate>), 2023.
- (2) Zhao, Y.; Pohl, O.; Bhatt, A. I.; Collis, G. E.; Mahon, P. J.; R  ther, T.; Hollenkamp, A. F. *Sustainable Chemistry* **2021**, DOI: 10.3390/suschem2010011.
- (3) Batteries Europe Development of reporting methodologies (<https://www.diva-portal.org/smash/record.jsf?pid=diva2%3A1629438&dswid=-6893>) (23/10/2023).
- (4) Batteries Europe Roadmap on advanced materials for batteries (2021). (<https://energy.ec.europa.eu/system/files/2021-12/vol-3-008-2.pdf>) (23/10/2023).
- (5) Batteries Europe Roadmap on cell design and manufacturing (2021). (<https://energy.ec.europa.eu/system/files/2021-11/wg4.pdf>) (23/10/2023).
- (6) Batteries Europe Roadmap on mobile applications of batteries (2021). (<https://www.2zeroemission.eu/wp-content/uploads/2021/12/Application-and-integration-mobile.pdf>) (23/10/2023).
- (7) Batteries Europe Roadmap on new and emerging technologies (2021). (<https://www.diva-portal.org/smash/record.jsf?pid=diva2%3A1629368&dswid=-9875>) (23/10/2023).
- (8) Batteries Europe Roadmap on raw materials and recycling (2021). (<https://energy.ec.europa.eu/system/files/2021-12/vol-2-009.pdf>) (23/10/2023).
- (9) Batteries Europe Roadmap on stationary applications for batteries (2021). (<https://energy.ec.europa.eu/system/files/2022-01/vol-6-009.pdf>) (23/10/2023).
- (10) <https://ease-storage.eu/publication/ease-era-energy-storage-technology-development-roadmap-2017/>.
- (11) https://emiri.eu/uploads/content_files/65/value__file/EMIRI.
- (12) E. Commission Implementation of the Strategic Action Plan on Batteries: Building a Strategic Battery Value Chain in Europe. (<https://eur-lex.europa.eu/legal-content/EN/TXT/?uri=COM:2019:176:FIN>) (23/10/2023).
- (13) Lebedeva, N., Di Persio, F., Brett, L. Lithium ion battery value chain and related opportunities for Europe. JRC Science for policy report (2016). (<https://publications.jrc.ec.europa.eu/repository/handle/JRC105010>) (23/10/2023).
- (14) Ruiz, V., Pfrang, A. JRC exploratory research: safer Li-ion batteries by preventing thermal propagation: Workshop report: summary & outcomes (JRC Petten, Netherlands, 8-9 March 2018). Publications Office of the European Union. Luxembourg (2018). (<https://publications.jrc.ec.europa.eu/repository/handle/JRC113320>) (23/10/2023).
- (15) Steen, M., Lebedeva, N., Di Persio, F., Boon-Brett, L. EU competitiveness in advanced Li-ion batteries for e-mobility and stationary storage applications - opportunities and actions. Publications Office of the European Union. Luxembourg (2017). (<https://publications.jrc.ec.europa.eu/repository/handle/JRC108043>) (23/10/2023).
- (16) Tsiropoluos, I., Tarvydas, D., Lebedeva, N. Li-ion batteries for mobility and stationary storage applications. JRC Science for policy report (2018). (<https://publications.jrc.ec.europa.eu/repository/handle/JRC113360>) (23/10/2023).
- (17) Hao, H.; Cheng, X.; Liu, Z.; Zhao, F. *Energy Policy* **2017**, DOI: 10.1016/j.enpol.2017.06.011.
- (18) Business Finland Batteries from Finland (2019). (<https://www.businessfinland.fi/49c3dd/globalassets/finnish-customers/02-build-your-network/bioeconomy--cleantech/batteries-from-finland/batteries-report-presentation-march-2019.pdf>) (23/10/2023).
- (19) Aayog, N. Zero Emission Vehicles (ZEVs): Towards a policy framework. (2018). (https://eamrit.niti.gov.in/assets/admin/dist/img/new-fronend-img/report-pdf/EV_report.pdf) (23/10/2023).

- (20) India Smart Grid Forum (ISGF). *Energy Storage System Roadmap for India: 2019-2032*. (2019). (https://www.cecpc-eu.in/uploads/documents/events/Webinar_on_Energy_Storage_ISGF.pdf) (23/10/2023).
- (21) Kurosawa, A. *Energy Storage Roadmap - Technology and Institution - Japan* (2017). (https://www.icef.go.jp/pdf/2018/roadmap/Energy_Storage_Roadmap_ICEF2017.pdf) (23/10/2023).
- (22) Takehiko, N. *The Japanese policy and NEDO activity for future mobility*. (2017). (<https://www.tresor.economie.gouv.fr/Articles/70dfe615-29bf-4ee4-a232-2fd2b954c025/files/59a6914a-57e1-495f-8108-abdec7d0715>) (23/10/2023).
- (23) U.S. DRIVE Electrochemical Energy Storage Technical Team Roadmap. 2017. (<https://www.energy.gov/eere/vehicles/articles/us-drive-electrochemical-energy-storage-technical-team-roadmap>) (23/10/2023).
- (24) Castillo, L.; Cook, G. *Lithium-ion batteries*; Nova Science Publishers: New York, 2018.
- (25) Huggins, R. A. *Advanced batteries*; Springer: New York, 2009.
- (26) Korthauer, R. *Lithium-Ion Batteries: Basics and Applications*; Springer Berlin Heidelberg: Berlin, Heidelberg, 2018.
- (27) Yoshio, M.; Brodd, R. J.; Kozawa, A. *Lithium-Ion Batteries*; Springer New York: New York, NY, 2009.
- (28) Zhang, L.; Zhuang, Q.; Zheng, R.; Wang, Z.; Sun, H.; Arandiyani, H.; Wang, Y.; Liu, Y.; Shao, Z. *Energy Storage Materials* **2022**, DOI: 10.1016/j.ensm.2022.04.026.
- (29) Wang, H.-F.; Wang, X.-X.; Li, F.; Xu, J.-J. *Small Science* **2022**, DOI: 10.1002/smssc.202200005.
- (30) Chen, F.; Li, J.; Huang, Z.; Yang, Y.; Shen, Q.; Zhang, L. *J. Phys. Chem. C* **2018**, DOI: 10.1021/acs.jpcc.7b10911.
- (31) Lobe, S.; Dellen, C.; Finsterbusch, M.; Gehrke, H.-G.; Sebold, D.; Tsai, C.-L.; Uhlenbruck, S.; Guillon, O. *Journal of Power Sources* **2016**, DOI: 10.1016/j.jpowsour.2015.12.054.
- (32) Ramakumar, S.; Deviannapoorani, C.; Dhivya, L.; Shankar, L. S.; Murugan, R. *Progress in Materials Science* **2017**, DOI: 10.1016/j.pmatsci.2017.04.007.
- (33) Zou, J.; Gao, X.; Zhou, X.; Yang, J.; Tang, J.; Kou, H.; Chang, R.; Zhang, Y. *Nanotechnology* **2023**, DOI: 10.1088/1361-6528/acb3cb.
- (34) Frenck, L.; Sethi, G. K.; Maslyn, J. A.; Balsara, N. P. *Front. Energy Res.* **2019**, DOI: 10.3389/fenrg.2019.00115.
- (35) Kazyak, E.; Garcia-Mendez, R.; LePage, W. S.; Sharafi, A.; Davis, A. L.; Sanchez, A. J.; Chen, K.-H.; Haslam, C.; Sakamoto, J.; Dasgupta, N. P. *Matter* **2020**, DOI: 10.1016/j.matt.2020.02.008.
- (36) Golozar, M.; Paoletta, A.; Demers, H.; Savoie, S.; Girard, G.; Delaporte, N.; Gauvin, R.; Guerfi, A.; Lorrmann, H.; Zaghbi, K. *Scientific reports* **2020**, DOI: 10.1038/s41598-020-75456-0.
- (37) Cheng, E. J.; Sharafi, A.; Sakamoto, J. *Electrochimica Acta* **2017**, DOI: 10.1016/j.electacta.2016.12.018.
- (38) Ren, Y.; Shen, Y.; Lin, Y.; Nan, C.-W. *Electrochemistry Communications* **2015**, DOI: 10.1016/j.elecom.2015.05.001.
- (39) Aguesse, F.; Manalastas, W.; Buannic, L.; Del Lopez Amo, J. M.; Singh, G.; Llordés, A.; Kilner, J. *ACS applied materials & interfaces* **2017**, DOI: 10.1021/acsami.6b13925.
- (40) Shen, F.; Dixit, M. B.; Xiao, X.; Hatzell, K. B. *ACS Energy Lett.* **2018**, DOI: 10.1021/acsenergylett.8b00249.
- (41) Cressa, L.; Sun, Y.; Andersen, D.; Gerard, M.; Castro, O. de; Kopljar, D.; Nojabae, M.; Friedrich, K. A.; Schmitz, G.; Wirtz, T.; Eswara, S. *Analytical chemistry* **2023**, DOI: 10.1021/acs.analchem.3c01059.
- (42) Loussert Fonta, C.; Humbel, B. M. *Archives of biochemistry and biophysics* **2015**, DOI: 10.1016/j.abb.2015.05.017.
- (43) Bi, Y.; Yang, W.; Du, R.; Zhou, J.; Liu, M.; Liu, Y.; Wang, D. *Journal of Power Sources* **2015**, DOI: 10.1016/j.jpowsour.2015.02.095.

- (44) Cojocaru-Mirédin, O.; Schmieg, J.; Müller, M.; Weber, A.; Ivers-Tiffée, E.; Gerthsen, D. *Microscopy and Microanalysis* **2022**, DOI: 10.1017/S1431927622003476.
- (45) Gelb, J.; Finegan, D. P.; Brett, D. J.; Shearing, P. R. *Journal of Power Sources* **2017**, DOI: 10.1016/j.jpowsour.2017.04.102.
- (46) Li, Y.; Huang, W.; Li, Y.; Pei, A.; Boyle, D. T.; Cui, Y. *Joule* **2018**, DOI: 10.1016/j.joule.2018.08.004.
- (47) Li, Y.; Li, Y.; Pei, A.; Yan, K.; Sun, Y.; Wu, C.-L.; Joubert, L.-M.; Chin, R.; Koh, A. L.; Yu, Y.; Perrino, J.; Butz, B.; Chu, S.; Cui, Y. *Science (New York, N.Y.)* **2017**, DOI: 10.1126/science.aam6014.
- (48) Thomas, C.; Edelman, M.; Lysenkov, D.; Hafner, C.; Bernthaler, T.; Schneider, G. *Microsc Microanal* **2010**, DOI: 10.1017/S1431927610056254.
- (49) Mazarov, P.; Dudnikov, V. G.; Tolstoguzov, A. B. *Phys.-Usp.* **2020**, DOI: 10.3367/UFNe.2020.09.038845.
- (50) Sigmund, P. *Phys. Rev.* **1969**, DOI: 10.1103/PhysRev.184.383.
- (51) Castro, O. de; Audinot, J.-N.; Hoang, H. Q.; Coulbary, C.; Bouton, O.; Barrahma, R.; Ost, A.; Stoffels, C.; Jiao, C.; Dutka, M.; Geryk, M.; Wirtz, T. *Analytical chemistry* **2022**, DOI: 10.1021/acs.analchem.2c01410.
- (52) Audinot, J.-N.; Philipp, P.; Castro, O. de; Biesemeier, A.; Hoang, Q. H.; Wirtz, T. *Reports on progress in physics. Physical Society (Great Britain)* **2021**, DOI: 10.1088/1361-6633/ac1e32.
- (53) Ziegler, J. F.; Ziegler, M. D.; Biersack, J. P. *Nuclear Instruments and Methods in Physics Research Section B: Beam Interactions with Materials and Atoms* **2010**, DOI: 10.1016/j.nimb.2010.02.091.
- (54) Liu, T.; Lin, L.; Bi, X.; Tian, L.; Yang, K.; Liu, J.; Li, M.; Chen, Z.; Lu, J.; Amine, K.; Xu, K.; Pan, F. *Nature nanotechnology* **2019**, DOI: 10.1038/s41565-018-0284-y.
- (55) Xue, L.; Li, Y.; Hu, A.; Zhou, M.; Chen, W.; Lei, T.; Yan, Y.; Huang, J.; Yang, C.; Wang, X.; Hu, Y.; Xiong, J. *Small Structures* **2022**, DOI: 10.1002/sstr.202100170.
- (56) Yu, Z.; Shao, Y.; Ma, L.; Liu, C.; Gu, C.; Liu, J.; He, P.; Li, M.; Nie, Z.; Peng, Z.; Shao, Y. *Advanced materials (Deerfield Beach, Fla.)* **2022**, DOI: 10.1002/adma.202106618.
- (57) Tripathi, A. M.; Su, W.-N.; Hwang, B. J. *Chemical Society reviews* **2018**, DOI: 10.1039/C7CS00180K.
- (58) Masuda, H.; Ishida, N.; Ogata, Y.; Ito, D.; Fujita, D. *Journal of Power Sources* **2018**, DOI: 10.1016/j.jpowsour.2018.08.040.
- (59) Mathayan, V.; Morita, K.; Tsuchiya, B.; Ye, R.; Baba, M.; Primetzhofer, D. *Materials Today Energy* **2021**, DOI: 10.1016/j.mtener.2021.100844.
- (60) Mathayan, V.; Moro, M. V.; Morita, K.; Tsuchiya, B.; Ye, R.; Baba, M.; Primetzhofer, D. *Appl. Phys. Lett.* **2020**, DOI: 10.1063/5.0014761.
- (61) Otoyama, M.; Kowada, H.; Sakuda, A.; Tatsumisago, M.; Hayashi, A. *The journal of physical chemistry letters* **2020**, DOI: 10.1021/acs.jpcllett.9b03456.
- (62) Yamagishi, Y.; Morita, H.; Nomura, Y.; Igaki, E. *The journal of physical chemistry letters* **2021**, DOI: 10.1021/acs.jpcllett.1c01089.

CHAPTER 2

1. CHAPTER 1 Background

2. CHAPTER 2 *Operando* Correlative SEM/SIMS

2.1. Motivation

2.2. Towards *Operando*

2.2.1. Prototype design

2.2.1.1. Electrochemical Experiments

2.2.1.2. Contact Pressure Control

2.2.1.3. Adaptation to inert gas transfer system and microscope

2.2.1.4. Final experimental configuration

2.2.2. Tests, validation, and proof of concept

2.2.2.1. Contact μ -manipulator – polarity plate

2.2.2.2. Resistance test

2.2.2.3. EIS comparison Swagelok – *Operando* holder

2.2.3. Materials and Sample Preparation

2.2.3.1. Materials

2.2.3.2. Sample Preparation

2.2.3.3. SIMS analysis

2.2.4. Results & Discussion

2.2.4.1. Pre-cycling

2.2.4.2. CC cycling

2.2.4.3. Post-cycling

2.2.4.4. Limitations

2.2.4.5. Discussion

2.3. Closing Remarks

Tables

References

2. *Operando* Correlative SEM/SIMS

2.1 Motivation

A plethora of new battery materials are object to research and uncountable questions remain unanswered to this day.¹⁻⁶ One way out of the darkness is by accumulating as much data as possible, in best case simultaneous and under operating conditions. Scientists agree that when studying complex systems such as batteries, it is insufficient to perform only ex- &/or in-situ characterization with pristine or post-mortem batteries, hence *operando* approaches are required.^{7,8} With *operando* correlative techniques we develop analysis and characterization approaches which intend to create a direct link between structure, chemical composition, and electrochemical performance, and by that accelerating battery research.

Correlative microscopy and spectroscopy utilize a combination of techniques to investigate the exact same region of interest (ROI). By employing multiple approaches, complementary information of the studied system and its properties can be obtained. These advanced analysis approaches study and correlate different aspects or properties i.e. morphology, structure, as well as chemical aspects like composition, distribution of chemical compounds, trace element or dopant concentration, and physical properties like optical properties or electrochemical performance.

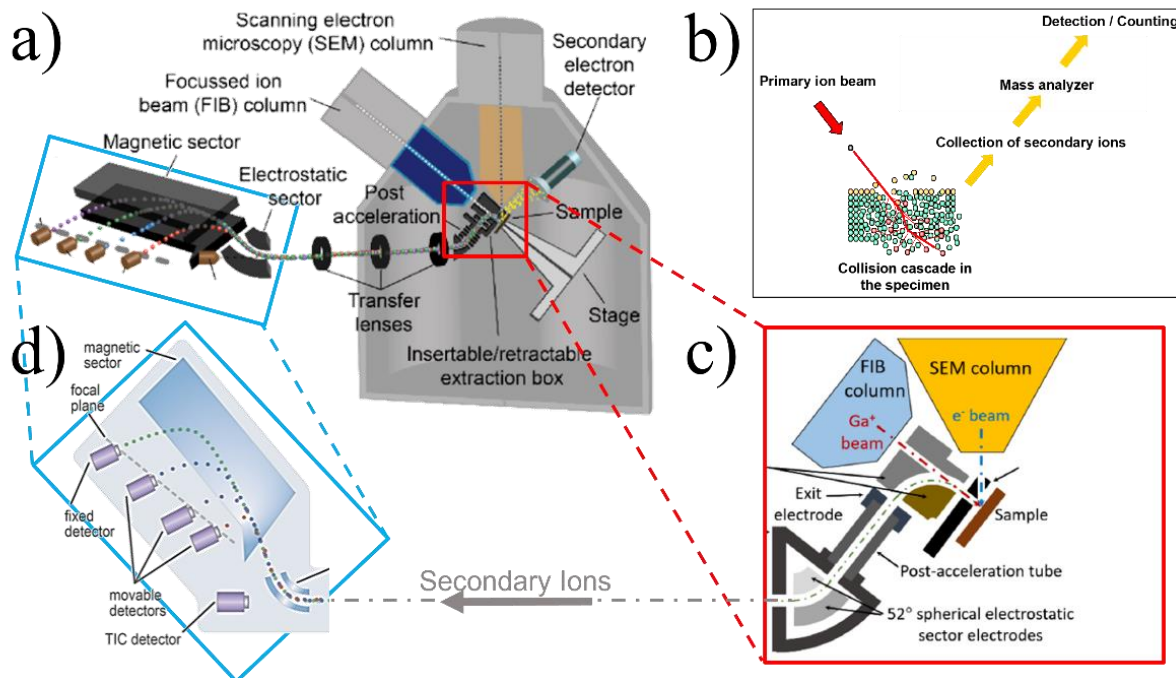


Figure 1: Schematics of the FIB-SEM-SIMS instrument: a) the set-up of the vacuum chamber with the secondary electron column on top, the FIB column with an inclination of 52° relative to the scanning electron column, a secondary electron detector and the sample stage which can be moved, rotated and tilted. b) The theoretical path from primary ion irradiation to secondary ion (SI) collection, which are then entering the mass analyser. c) the insertable/retractable extraction box. Here the Ga ions (primary ions) from the FIB column are passing through a small aperture in the extraction box and are hitting the sample. Consequently, secondary ions are being efficiently extracted and collected by the extraction box. Through a post-acceleration tube and a 52° spherical electrostatic sector the secondary ions enter the transfer optics part of the instrument.

Here three lenses are responsible for focussing and shaping the secondary ion beam. Then in d) the SI enter an electrostatic sector, before they enter the magnetic sector where the SI are separated by their mass to charge ratio. On the focal plane, four detectors (one fixed, three movable) are positioned and capture/detect the SI. (taken from ⁹)

In this work we mainly use a FIB/SEM onto which a compact magnetic sector SIMS has been attached (see Figure 1). This combination of a simple and robust imaging by SEM with a high-resolution, high-sensitivity characterization and chemical imaging technique SIMS, results in a very powerful instrument for correlative structural and compositional analysis. For the operation of SIMS, an extraction box will be inserted by means of automated piezo-positioners between the sample and the nozzle of the ion column. The primary ion beam ($^{69}\text{Ga}^+$) passes through a tiny hole in the extraction box and hits the sample (Figure 1 b & c). Sputtered secondary ions (of one polarity) can be collected by the extraction box and are post accelerated to the mass spectrometer (Figure 1 b & d). SEM/SIMS can be used for a multitude of different studies⁹ e.g. biology, materials science, geology; however, this work focusses on battery materials and especially on LLZO based solid-state batteries (see Figure 2). The correlative technique allows to gather complementary data on structure and chemistry and can be used for surface analysis of LLZO, the anode, the cathode as well as the interface between LLZO and the electrodes. While SEM/SIMS is purely surface sensitive, later chapters combine transmission techniques revealing bulk information.

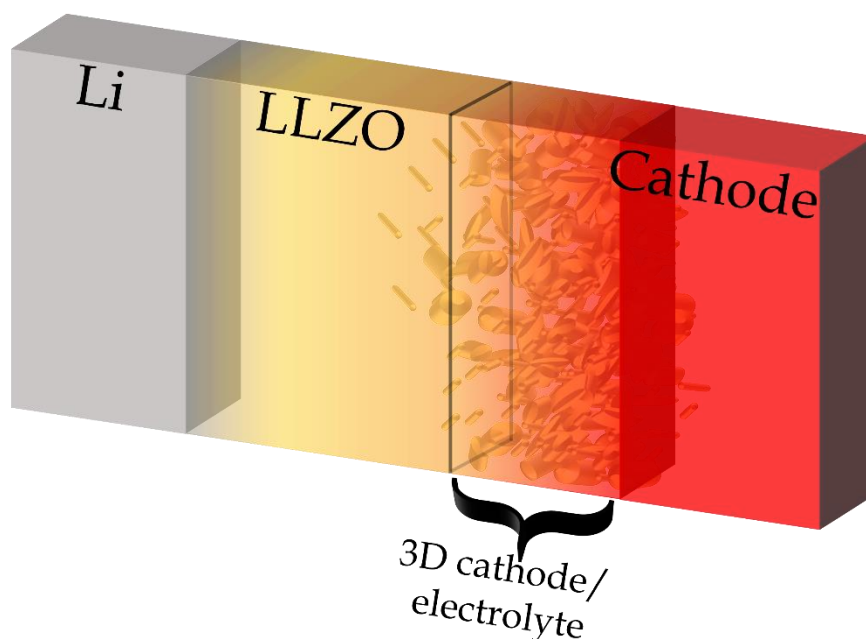


Figure 2: Schematics of a model solid-state battery with on the left the anode (e.g. lithium) in the centre the solid electrolyte (LLZO) and the cathode (e.g. LCO). The 2D electrodes are representative for a pure electrode composition, however the 3D composite cathode/electrolyte region represents a complex designed structure where cathode and electrolyte gradually merge.

Figure 2 shows a schematic of a model all-solid-state battery with on the left the anode (e.g. lithium) in the centre the solid electrolyte (LLZO) and the cathode (e.g. LCO), which has been discussed in detail in Chapter 1. Different chapters in this work

address and focus on the analysis of different parts of the battery. The samples which are studied in this chapter with correlative approaches are LLZO-based battery samples, more specifically Li/LLZO/Li half-cells.

With SEM/SIMS being already a correlative technique per se, within this work we took advantage of a multitude of other techniques (e.g. X-ray based techniques, neutron imaging, and *operando* approaches) to obtain complementary data beyond structural and chemical imaging performed via SEM/SIMS.

This chapter elucidates the design, the validation and calibration of a SEM *operando* approach for solid-state batteries. While SEM analysis can be performed in *operando* mode, SIMS characterization is now only operational *in situ*. The chapter ends with proof-of-concept measurements and a discussion. In chapter 4 a different *operando* methodology, based on neutron imaging will be discussed.

2.2 Towards *Operando*

"*Operando*" is a scientific term used to describe a methodology where an experiment or analysis is conducted under realistic and operational conditions, such as during the actual operation of a device, rather than under idealized or simplified conditions. The main goal is to study the behaviour of materials and systems during actual operation.

In this chapter we first elucidate the challenges and the benefits which come with the implementation of *operando* in analytical workflows. As our approach is based on a custom-made sample-holder, the prototype design as well as calibrations and validations are shown. Proof-of-concept results will be discussed at the end of this chapter.

Electrochemical energy storage systems i.e. batteries represent complex systems in which many factors interact in a dynamic interplay during operation. To design more efficient and safer batteries, a deep understanding of the operational state is key. However, to do so with traditional analysis methods, is very challenging and often not feasible. The reason for the restricted access to advanced *operando* analytical techniques to study lithium-ion batteries (LIB) can be attributed to three factors:

- 1) The incorporation of *operando* techniques in analytical instruments often involves significant modifications to the instruments themselves.
- 2) A continuous inert gas atmosphere or vacuum is necessary due to the sensitivity of many battery components to air and moisture.
- 3) Conventional chemical analysis methods like Energy-dispersive X-ray spectroscopy are not suitable for analysing low-Z elements such as hydrogen (H) or lithium (Li), which are crucial when studying batteries.

Numerous studies have been conducted in the field of battery research, with researchers designing creative setups and workflows to enable *in-situ* or *operando* studies of batteries.¹⁰⁻¹⁷

In this study, we propose a methodology for conducting *in situ* magnetic sector SIMS with an impressive lateral resolution of 15 nm for chemical imaging and a depth resolution of approximately 4 nm. The primary focus lies in investigating the degradation mechanisms inside solid electrolytes.⁹

Zhang et al.¹⁸ provides a summary of the progress and future perspectives in electrochemical and structural analysis of all-solid-state lithium batteries using analytical electron microscopy (AEM). AEM techniques, such as scanning transmission electron microscopy (STEM) and energy-dispersive X-ray spectroscopy (EDX), have proven valuable in investigating complex interfacial phenomena and degradation mechanisms in solid-state batteries.¹⁹ The article also discusses future directions and challenges in advancing AEM analysis for all-solid-state batteries and especially highlight the need for advancements in sample preparation techniques, data analysis, and *in situ/operando* characterization methods to further improve the understanding of battery materials and interfaces.

Few studies, have a more critical view on the analysis of SSBs and *operando* approaches. López et al.²⁰ discuss the analysis of interfaces and also show that the development of strategies to probe buried interfaces might pave the way to progress in attractive *in situ* and *operando* measurements. Blondeau et al.²¹ study beam effects on *operando* systems and warns from misinterpretations and incorrect conclusions originated from the interference between cycling and analysis. The critical point of view of such articles are crucial for the development and progress of next generation *operando* analytical tools.

2.2.1 Prototype design

To this day there is no existing commercial option for *operando* correlative SEM / *in situ* SIMS analysis of SSBs. Hence, we developed a custom-designed sample holder. The following technical specifications have been met by the design:

- 1) Option to secure a sample between two electrically conductive plates that are separated by an insulating material.
- 2) Possibility to adjust and regulate the force exerted on the sample between the two plates.

3) The size of the setup is sufficiently small to fit into the inert gas transfer system (IGTS) and is compatible with the airlock system of the FIB-SEM instrument. This includes considerations such as dimensions, sample stage adapter, and materials.

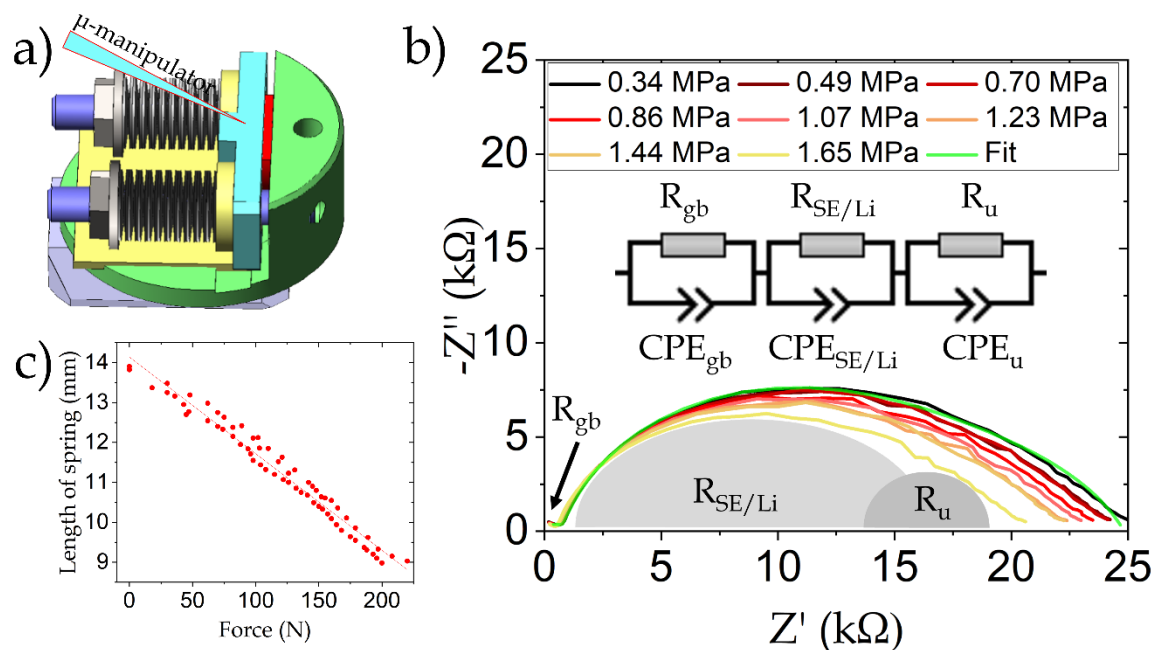


Figure 3: a) Schematics of the custom-designed sample holder; the red component represents the semi-circular sample clamped between two electrically insulated plates (green & cyan). b) Example of interface resistance reduction with increasing pressure. The applied pressure from 0.34 MPa to 1.65 MPa shows a considerable reduction of the interface impedance $R_{SE/Li}$. The equivalent circuit for the fitting (0.34 MPa) is shown as inset and the impedance contributions of grain boundary (R_{gb}), solid electrolyte with the Li electrodes ($R_{SE/Li}$) and an additional resistance (R_u) are exemplarily shown. The fitting parameters are given in Table S1. c) Calibration curve of the sample-holder correlating “length of the spring” to “applied force”.

Figure 3 a) illustrates a representation of the sample holder; a specially designed IGTS, developed in collaboration with Ferrovac AG (refer to Figure 4), allows to transfer samples between a glove box and the instrument without any contamination. This feature ensures contamination-free and time-efficient workflows, as there is no need to transfer samples between electrochemical experiments and structural/chemical analysis. The FIB-SEM instrument is equipped with an in-house designed magnetic sector SIMS, and details about the FIB-SEM-SIMS instrument and its performance can be found elsewhere⁹ (Chapter 1). The incorporation of SIMS into described workflows provides significant advantages for chemical analysis²², as it enables the detection and measurement of the distribution of low-Z elements such as ^1H ²³ and ^7Li ^{24,25}.

2.2.1.1. Electrochemical experiments. The custom designed sample holder enables a multitude of electrochemical experiments such as constant current (CC) cycling or electrochemical impedance spectroscopy (EIS) at ambient atmosphere, inside a glovebox and inside of the FIB/SEM instrument. A potentiostat from BioLogic (SP-150) is used and connected to the polarity plates of the sample holder either directly (at air or in the glovebox) or via sample stage bias connection and the

micromanipulator (inside FIB/SEM). Preliminary tests (CC dis/charge) with commercial batteries as well as resistance measurements with surface-mount resistors were performed to validate the prototype and its design. The EIS measurements shown in Figure 3 b) were conducted using potentiostatic mode with a frequency range of 1 MHz to 1 Hz. The applied voltage amplitude was 5 mV. The observed impedance plot displayed a large semi-circle that decreases in size as pressure increases. The large semi-circle corresponds to the impedance at the interface between the solid electrolyte and the lithium $R_{SE/Li}$. Detailed information on the fit parameters used for simulating the EIS data in Figure 3 b) can be found in the appendix (Table 1), and the justifications for the identifications of the different features in the Nyquist plots are confirmed by literature²⁶⁻³⁵. It is important to note that the measurements depicted in Figure 3 b) and c), as well as all electrochemical tests performed on commercial coin cells, were carried out outside the FIB-SEM instrument. These measurements were conducted within a controlled atmosphere provided by a glovebox.

2.2.1.2. Contact pressure control. Pressure regulation is achieved through the use of springs in the sample holder. These springs, made up of multiple Belleville washers, are capable of applying a force ranging from 20 N to 220 N. To ensure accurate pressure control, the springs were calibrated using force sensors provided by SingleTact (<https://www.singletact.com/>). The calibration curve of the "applied force" versus the "length of the spring" is depicted in Figure 3 c). This calibration allows the operator to consistently apply the same pressure when analyzing multiple samples.

This pressure control feature is significant for several reasons. Firstly, increasing the pressure enhances the effective contact area between the lithium and the solid electrolyte, resulting in an improvement in contact area which can lead to decreased impedance at the interface. Additionally, high-pressure conditions have been shown to extend the lifetime of solid-state batteries (SSBs), making them a subject of investigation for potential applications³⁶⁻⁴⁰.

An experimental illustration of the relationship between impedance and pressure can be observed in Figure 3 b). The graph demonstrates a decrease in the resistance at the solid-electrolyte-lithium interface by ~20% as the pressure is increased from 0.34 to 1.65 MPa.

2.2.1.3. Adaptation to inert gas transfer system and microscope. The sample holder was specifically designed to seamlessly integrate with both the inert gas transfer system (IGTS) and the FIB-SEM instrument. Careful consideration was given to the dimensions of the sample holder, which has a diameter of 3.2 cm and a height

of 1.9 cm. The materials used in its construction are stainless steel and Al_2O_3 , ensuring optimal compatibility with the IGTS and FIB-SEM instrument.

A contamination free sample preparation and sample transfer is only possible with an inert gas transfer system which in our case is composed of a transfer chamber on the microscope and a portable vacuum-tight transfer box (Figure 4 a, b). This box can be introduced in a glove box, and the *operando* sample holder (with the sample) can be locked inside the transfer box. Subsequently the transfer box is removed from the glove box and attached to the air lock at the microscope (Figure 4 c, d), where the argon atmosphere inside the box gets pumped before the sample is introduced inside the microscope.

To enable electrochemical analyses within the FIB-SEM instrument, an electrical closed circuit needs to be established. One electrode of the potentiostat is connected to the sample stage bias connection of the microscope, while the second electrode is connected to the micro-manipulator. The micro-manipulator, depicted in Figure 3 a) (schematics) and Figure 6 b) (SEM image), consists of a microscopic needle located inside the FIB-SEM instrument. It is capable of movement along the three spatial axes and is typically used for FIB lamella preparation for transmission electron microscopy (TEM). This setup allows for the performance of electrochemical analyses while utilizing the capabilities of the FIB-SEM instrument.

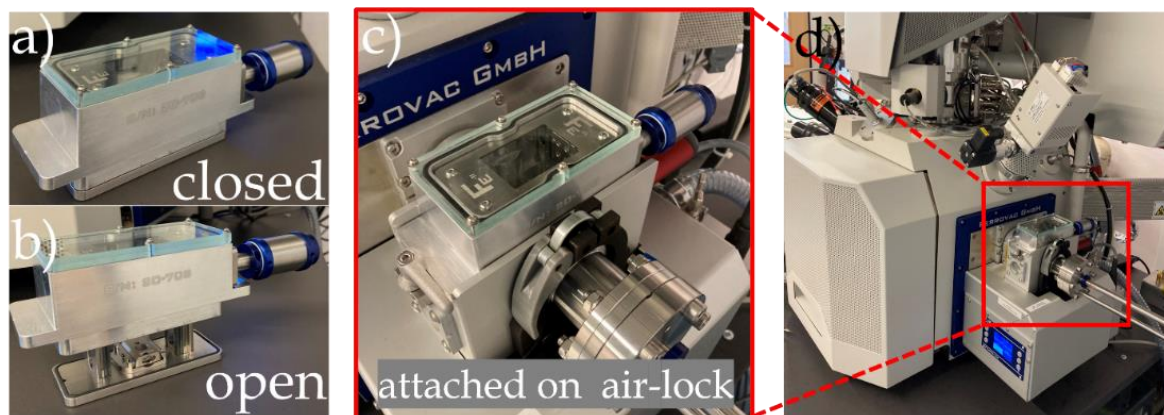


Figure 4: Inert gas transfer system. a) closed and b) open portable transfer box c) transfer box mounted on the air lock, and d) a view of the transfer box, air lock and microscope.⁴¹

2.2.1.4. Final experimental configuration. The final experimental setup, illustrated in Figure 5 a), can be described as follows: an external potentiostat is connected to the FIB-SEM instrument using two electrodes. One electrode, represented by the blue cable in Figure 5, is attached to the micromanipulator. The micromanipulator is capable of movement along the three spatial axes inside the instrument and can establish contact with the electrode plate of the *operando* sample holder, which is highlighted in blue in Figure 5 b) and c).

The second electrode, indicated by the red cable, is connected to the sample stage bias connection closing the circuit. This connection point is electrically isolated from the rest of the microscope and is highlighted in red in Figure 5 b) and c). A third cable, depicted in grey, links the potentiostat to a PC, which serves to control and monitor the electrochemical experiments.

In Figure 5 a), the dashed green box denotes the SIMS add-on. To switch between the "electrochemical analysis" and "SEM/SIMS analysis" modes, the micromanipulator is retracted. Additionally, an automated piezo-positioner mechanism is employed to insert the secondary ion extraction box between the sample and the ion column nozzle. Detailed information is provided by De Castro et al.⁹

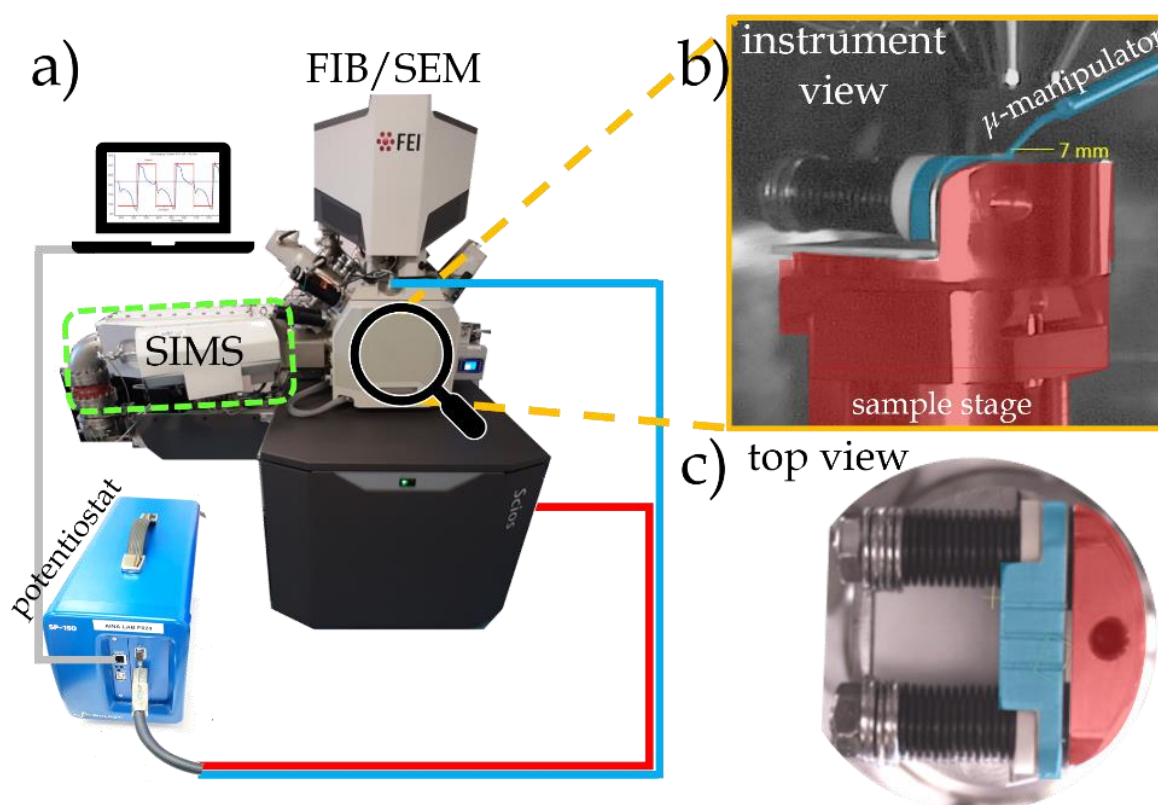


Figure 5: a) Schematic of the instrumental set-up of the FIB-SEM instrument and the SIMS add-on (green box). The potentiostat (BioLogic SP-150) is connected to different parts of the instrument: via red cable to the sample stage bias connection and via blue cable to the micro-manipulator. The grey cable connects the PC and is responsible for monitoring and controlling the electrochemical experiments. The zoom-in in b) shows the view inside of the instrument when the sample holder is introduced. The sample stage plus the part of the sample holder which are electrically connected, are highlighted in red and indicate one polarity. The FIB micro-manipulator and the electrically connected plate are highlighted in blue and indicate the other polarity. c) shows a top view of the sample holder; the slit between the red and blue plates is where the sample is clamped. The sample holder contains parts which are made of aluminium oxide Al_2O_3 to ensure electrical insulation between the two terminals.⁴²

2.2.2 Tests & validation

The electrochemical experiments such as constant current cycling, chronopotentiometry or impedance spectroscopy were performed using a SP-150 potentiostat from BioLogic. All test measurements with commercial coin cells have

been performed either outside or inside but vented FIB/SEM sample chamber to prevent contamination of the chamber due to possible outgassing. Several electrochemical tests have been performed with commercial coin cell batteries, surface mount resistors, and half-cells to validate the prototype design and troubleshoot potential issues.

2.2.2.1. Contact μ -manipulator – polarity plate. 6 a) shows an example of a chrono potentiometric discharge (with 20 mA from 3.2 V to \sim 1.5 V) of a RS Pro CR2032 3 V Lithium Manganese coin battery, 225 mAh (primary battery). The focus of this test was the optimisation of contact between micromanipulator and electrode plate. The black noisy line presents an example where the contact between the micromanipulator and the corresponding plate of the sample holder was not ideal. In this case, we contacted the electrode via the μ -tip (see 6 b). To increase the contact area between micromanipulator and electrode, we decided to remove the μ -tip and instead to contact the electrode directly with the bigger supporting rod onto which the microscopic tip is usually attached. The red curve shows the same experiment but with an intimate contact between micromanipulator and electrode, resulting in a smooth discharge curve.

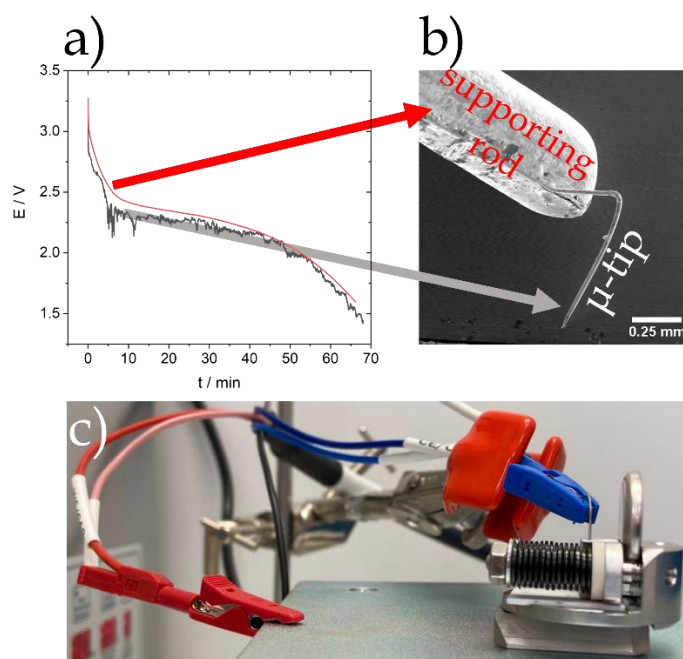


Figure 6: a) chronopotentiometry of a RS Pro CR2032 3 V Lithium Manganese coin battery with bad contact (black) and good contact (red) between micromanipulator and electrode. b) SEM image of the micromanipulator (supporting rod and the μ -tip) c) experimental testing set-up outside the FIB-SEM instrument. Red electrode attached to a lifting platform imitating the sample stage and the crocodile clip of the blue cable holding the micromanipulator that contacts the other electrode.⁴²

Figure 6 b) illustrates a SEM image showing the micromanipulator (= supporting rod and the μ -tip). These and many additional test measurements have been performed to validate and ensure a proper and artefact-free operation of our custom-designed sample holder. Figure 6 c) shows the experimental set-up for electrochemical

experiments with commercial coin cells outside of the FIB/SEM with red electrode attached to a metallic lifting platform imitating the sample stage and the crocodile clip of the blue cable holding the micromanipulator that contacts the second electrode plate.

2.2.2.2. Resistance test. Additionally, we performed resistance tests to see whether our experimental setup (*operando* holder & microscope) does not add too much resistance, which could result in erroneous results and misinterpretations. These tests have been performed with two different surface mount resistors (100 Ω and 200 Ω), and for each, the experiment has been performed with 1, 2, and 3 resistors. Figure 7 shows how the resistors were mounted on the sample holder and the zoom-in shows an SEM image of one of the resistors. The sample holder itself only adds an average of $1.3 \pm 0.8 \Omega$ to the system which is indeed negligible. The measurements performed with the sample holder inside the microscope and contacted using the micromanipulator shows an average total resistance of $12.8 \pm 3.5 \Omega$ also this is negligible compared to the electrochemical systems which will be analysed.

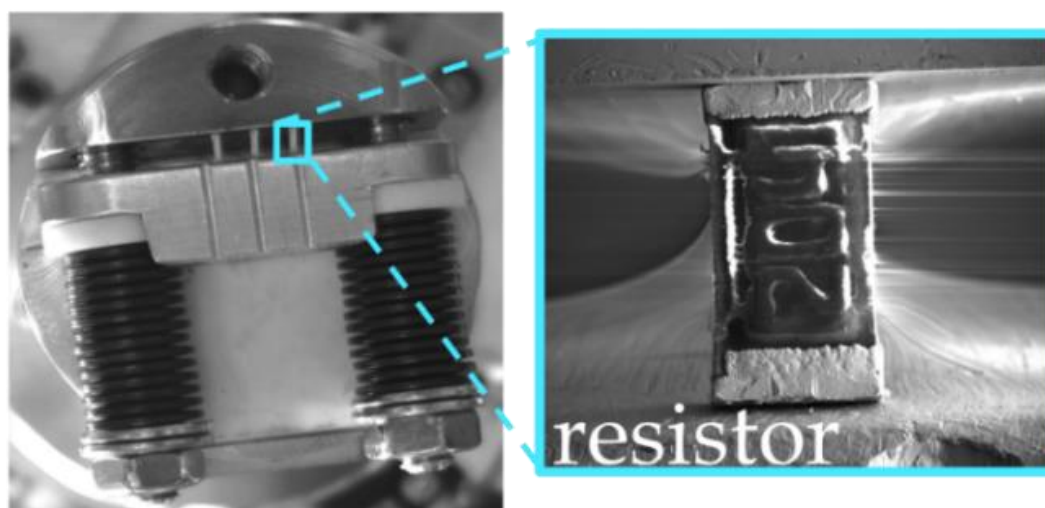


Figure 7: Operando sample holder with three resistors mounted. The zoom-in shows an SEM image of one of the resistors.⁴²

2.2.2.3. EIS comparison Swagelok – Operando holder. EIS measurements of the same sample have been performed first in a Swagelok cell and subsequently in our *operando* prototype sample holder. The EIS profiles can be seen in Figure 8. The shapes of the two EIS measurements are identical, the only difference is that for the *operando* sample holder the impedance of the SE/Li interface is slightly lower which is probably a consequence of the sample being clamped with more force (pressure) than in the Swagelok cell. The fit parameters for simulated EIS in Figure 8 can be found in the annex (Table 2). Nonetheless, as the shape of the semi-circles is identical, we conclude that our set-up does not significantly alters the impedance of the samples, if the force which is applied onto the sample stays the same.

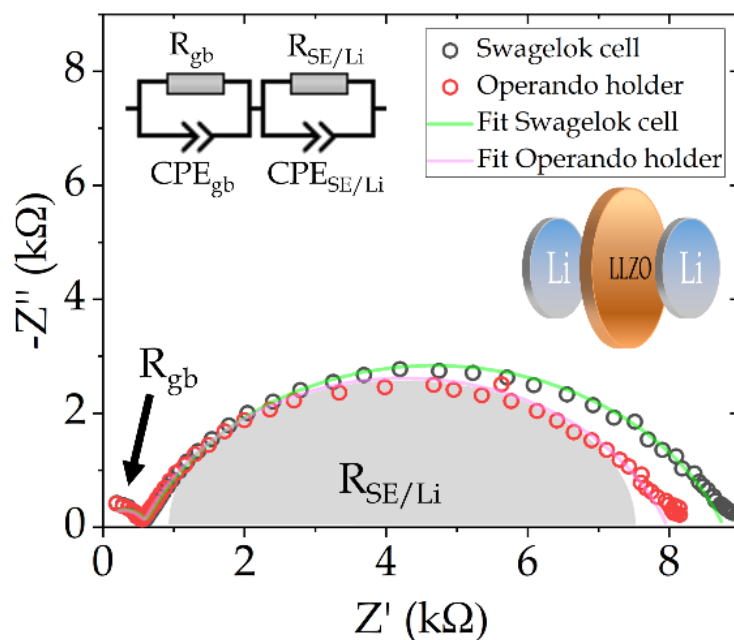


Figure 8: EIS measurements of the same Li/LLZO/Li half-cell inside a conventional Swagelok cell and inside the operando sample holder. The equivalent circuit for the fitting is shown as inset and the impedance contributions of grain boundary (R_{gb}) and solid electrolyte - Li interface ($R_{SE/Li}$) are exemplarily shown.⁴²

2.2.3 Materials and Sample Preparation

This subchapter will elucidate what materials have been used for the samples and how the samples were prepared to enable a successful proof of concept of the *operando* approach. The complex workflow relies on the success of several experimental stages, each of which must be completed successfully.

- 1) Contamination-free sample preparation and transfer from glove-box to instrument (FIB/SEM).
- 2) Pre-cycling structural (via SEM) and chemical (via SIMS) analysis.
- 3) Constant current cycling (until short-circuit in this proof of concept).
- 4) Post-cycling structural (via SEM) and chemical (via SIMS) analysis, with a focus on degradations related to cycling.

2.2.3.1. Materials. $\text{Li}_7\text{La}_3\text{Zr}_2\text{O}_{12}$ (LLZO) powder (particle diameter: 2–20 μm) from Jining CreaTech Energy Technology Co., Ltd, China, was used to produce the pellets. The preparation of LLZO pellets in this study followed similar procedures as described in the works of Zhang et al.⁴³, Jiang et al.⁴⁴, and Ganesh Kumar et al.⁴⁵. The resulting pellets exhibited a high density of 5.1 g/cm^3 .

Following the sintering process, the pellets were polished using sandpaper with a grit number of #4000, resulting in final dimensions of 11 mm in diameter and 1-1.5 mm in thickness. The metallic Li-foil, which was used for assembling the half-cell, was obtained from Alfa Aesar (CAS-No. 7439-93-2).

Figure 9 shows the phase purity of a pristine LLZO pellet (blue), determined by X-ray diffraction (XRD, Bruker AXS D8 Discover) using the Cu-K α 1 radiation with a 2θ step size of 0.02° (scan rate = $0.02^\circ/180$ s). A reference pattern (black) for cubic structure was taken from the PDF 04-022-7984 database, and a post-mortem (red) XRD pattern are plotted as well. The fact that the reference pattern and the pattern from the pristine sample show the same peaks, indicates a pure LLZO phase of the sample.

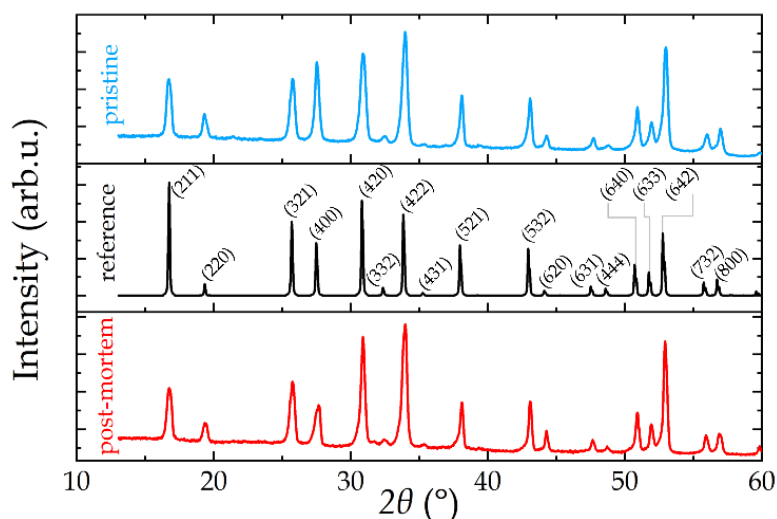


Figure 9: XRD patterns of a pristine LLZO pellet (blue), a reference pattern (black) for cubic structure taken from the PDF 04-022-7984 database, and a post-mortem sample (red). (XRD performed by Yanyan Sun at DLR)⁴²

2.2.3.2. Sample Preparation. Sample preparation for SIMS analysis requires addressing two main sample requirements. Firstly, to ensure efficient secondary ion extraction, a homogeneous electrical field must be generated between the sample and the extraction box. This can only be achieved when analyzing planar samples. Secondly, the ROIs which are in this case degradation effects induced by cycling, should be readily accessible for analysis. As per these requirements, the ROIs should either be on an exposed surface or within a depth that can be reached through FIB-milling.

Considering these factors, it was concluded that using a regular circular cell is not suitable for the *operando* approach. The curvature of a circular cell poses challenges, particularly for SIMS analysis. Therefore, a compromise was sought, leading to the decision to analyze a semi-circular solid-state half-cell.

To implement this approach, the LLZO pellet was divided into two parts, resulting in a semi-circular pellet with one planar side. The semi-circular LLZO pellet was then embedded between two semi-circular Li-foils, forming a Li/LLZO/Li sandwich structure. This assembly was mounted in the custom-designed sample holder. Importantly, the straight and planar side of the assembly was positioned to face the electron-/ion-beam for analysis. It is worth noting that operating with this

unconventional dimension for a solid-state half-cell introduces a drawback: the electrochemical cycling performed in this setup cannot be directly compared to that of commercial cyclers.

Three different ways to divide the sample and treat the freshly exposed surface of interest were investigated:

- a) Cutting the LLZO pellet with a wire saw, polishing with SiC sandpaper up to #4000 and cleaning with 1M HCl followed by 1 h vacuum drying at room temperature.
- b) Cutting the LLZO pellet with a wire saw and cleaning with 1 M HCl followed by 1 h vacuum drying at room temperature.
- c) Physically breaking the LLZO pellet by hand and cleaning with 1M HCl followed by 1 h vacuum drying at room temperature.

In order to get a straight edge when physically breaking the LLZO pellet, a notch was carefully carved with a cutter knife to dictate the direction of breaking.

A comparison of the three sample preparation methods based on the microstructural appearance (laser profilometer), the SEM image quality and the SIMS feasibility based on the $^{139}\text{La}^+$ signal was made (Figure 10).

Figure 10 a) shows an SEM image of a polished LLZO surface, in b) we see an unpolished surface (cut via wire saw) and c) shows a sample surface which has been cracked by hand. The polished sample (Figure 10 a) has the advantage that it has the least topography, hence resulting in promising SIMS results (Figure 10 e). The unpolished sample (Figure 10 b) has a very rough topography with strong artefacts in SIMS. The line profiles in d) reveal that the polished sample is obviously the one with least topography. The unpolished sample shows topographic roughness with up to 10 μm amplitude which is very unfavourable for SIMS analysis. The cracked sample reveals more pronounced roughness than the polished sample, however it has plateaus which are large and flat enough to successfully perform SIMS analysis. Unlike the polished sample, the cracked sample has the benefit that the granular shape of LLZO remains intact and that there is no cross-contamination possible related to cutting (often lubricant or liquid used) or polishing. One drawback of the polished sample is that polishing introduces small artefacts, e.g. lines that can clearly be seen in the SEM (Figure 10 a) and in the SIMS image (Figure 10 e). On the other hand, the cracked sample also presents a minor drawback: due to locally different incidence angles of the primary beam, slightly different sputter yields are obtained, resulting in different counts at different faces of a LLZO grain (details under Results and Discussion). Nonetheless, we decided that the cracked sample has the lowest risk of cross-contamination (structurally as well as chemically) and presents very good SIMS results in the ratio of sputter yields, hence was selected to be the sample preparation

of choice for this proof-of-concept study. It is worth mentioning that for ions non-blocking interfaces are used in this work.

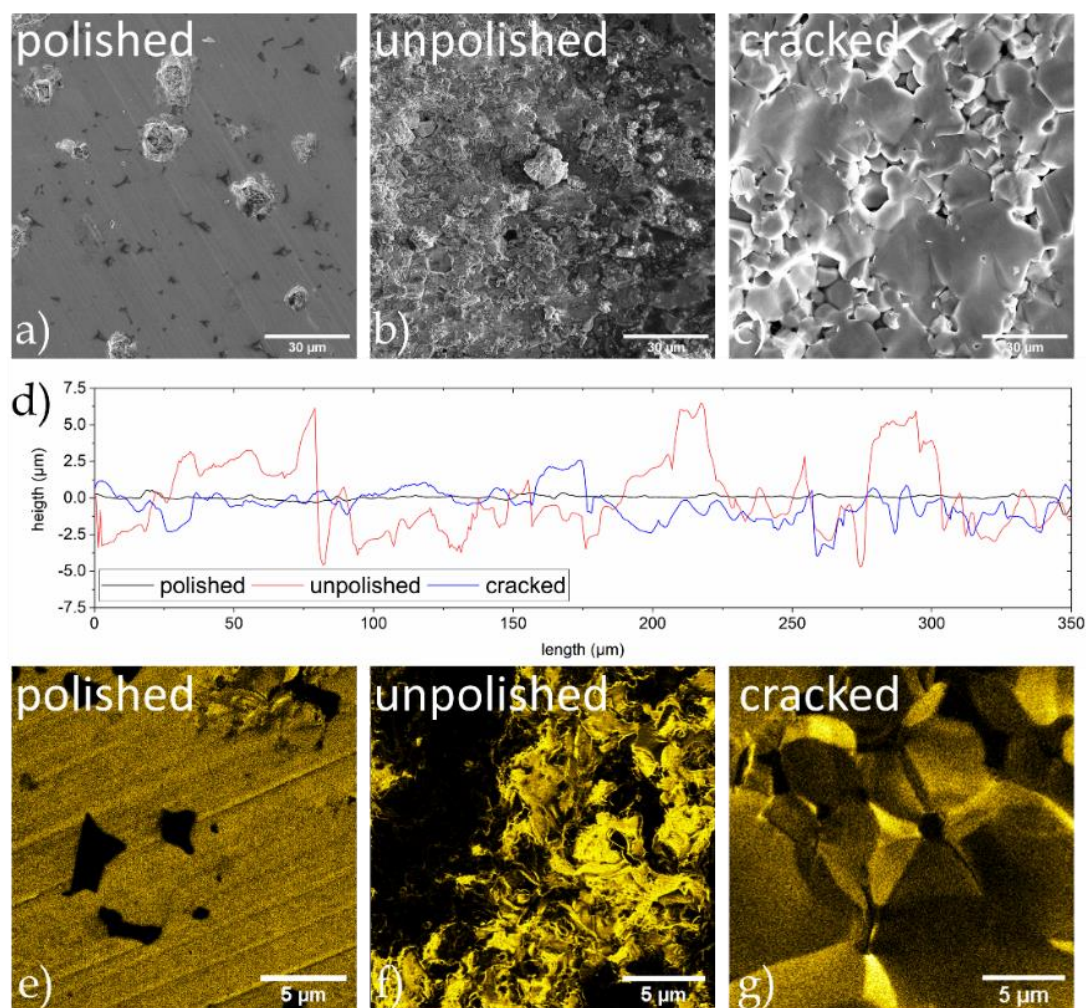


Figure 10: The top row shows SEM images of a) the polished, b) unpolished and c) cracked samples. The diagram in d) shows topographic line profiles of the three samples, which have been performed with a Keyence VK-X1100 Laser Scanning Confocal Microscope (LSCM). The black curve is representative for the polished sample, the red curve for the unpolished and the blue curve for the cracked sample. The last row (e, f and g) shows $^{139}\text{La}^+$ SIMS maps of the three samples. The cracked sample occasionally show relatively smooth microscale sections which are suitable for SIMS analysis.⁴²

2.2.3.3. SIMS Analysis. A Thermo Fisher Scios DualBeam FIB-SEM instrument with a custom-made double-focusing magnetic sector SIMS system was used to perform chemical imaging. This system allows the simultaneous detection of multiple masses. The FIB utilizes a gallium liquid metal ion source to produce primary ions of $^{69}\text{Ga}^+$. The collected and imaged secondary ions were $^7\text{Li}^+$, $^{139}\text{La}^+$, and $^{155}\text{LaO}^+$. The SIMS measurements were conducted with a primary ion beam energy of 30 keV, a beam current ranging from 0.1 to 0.3 nA, and dwell times between 0.5 and 1 ms. The resulting images had a resolution of 512×512 pixels and covered fields of view between 20×20 and 30×30 μm. To extract positive secondary ions, the sample was biased to +500 V, which corresponded to a primary ion impact energy of 29.5 keV.

Data analysis was performed using the freely available software ImageJ⁴⁶ and the commercial software AVIZO (Version 2021.1., Thermo Fisher).

Prior to the experiment the sample underwent a vacuum drying process inside the transfer chamber for approximately 1 hour and was then moved into an Ar-glove box with low oxygen and water contamination ($[O_2] \approx 0.6$ ppm; $[H_2O] \approx 0.8$ ppm) for the assembly of the half-cell. The sample was clamped between two plates of the sample holder with a force of approximately 76 N, resulting in a pressure of approximately 1.93 MPa. The force value was determined using the calibration curve shown in Figure 3 c), and the pressure was calculated based on the effective surface area on which the force was applied.

Once the sample was prepared and securely mounted in the sample holder, the holder was placed inside an airtight transfer shuttle (see Figure 4), enabling contamination-free transfer between the glove box and the FIB-SEM instrument. After introducing the sample holder into the FIB-SEM instrument (see Figure 5), the sample underwent both microstructural and chemical analysis.

2.2.4 Results & Discussion

2.2.4.1. Pre-cycling. The microstructural analysis of the sample involved the use of secondary electron imaging, which provided insights into the granular structure of the pellet, including porosities (Figure 11 a). X-ray computer tomography measurements conducted on similar samples synthesized using a comparable procedure indicated a porosity level below 8% (refer to Chapter 3 for details).

During the pre-cycling analysis, only a single phase was identifiable based on the structure and chemical composition of the sample. The XRD pattern displayed in Figure 9 exhibited no additional peaks when comparing the pristine LLZO pellet to the reference pattern obtained from the PDF 04-022-7984 database. This observation indicates the presence of only a single phase.

The SIMS analysis further confirmed the exclusive composition of LLZO through chemical imaging. Figures 11 b, c, and d illustrate the chemical images of ${}^7\text{Li}^+$, ${}^{139}\text{La}^+$, and ${}^{155}\text{LaO}^+$ ions, respectively. The absence of any additional phases in the XRD data, the lack of such phases in the secondary electron images, and the homogeneous distribution of the detected secondary ions all serve as strong indications that the sample preparation and transfer processes were conducted in a contamination-free manner.

The observed slight differences in the signals of the secondary electrons and secondary ions on different faces of the particles can be attributed to topographic effects. These variations in detected secondary charged particle intensities within a

single phase align with Sigmund's theory of sputtering⁴⁷ as well as numerous studies on particle-matter interactions⁴⁸⁻⁵¹.

Figure 11 b), c), d), g), h), and i) demonstrate a typical scenario of differential sputter yields associated with distinct local incidence angles of the primary beam. The LLZO particles have an intrinsic granular shape, and as the sample was not polished, the exposed surface of the pellet exhibits significant topography, reaching up to a microscale level (as depicted in Figure 10). When the primary beam interacts with surfaces of varying inclinations, variations in the sputter yield and consequently the intensities of the secondary ions can be observed. Typically, the sputter yield increases up to a glancing angle, beyond which it decreases due to the reflection of the primary

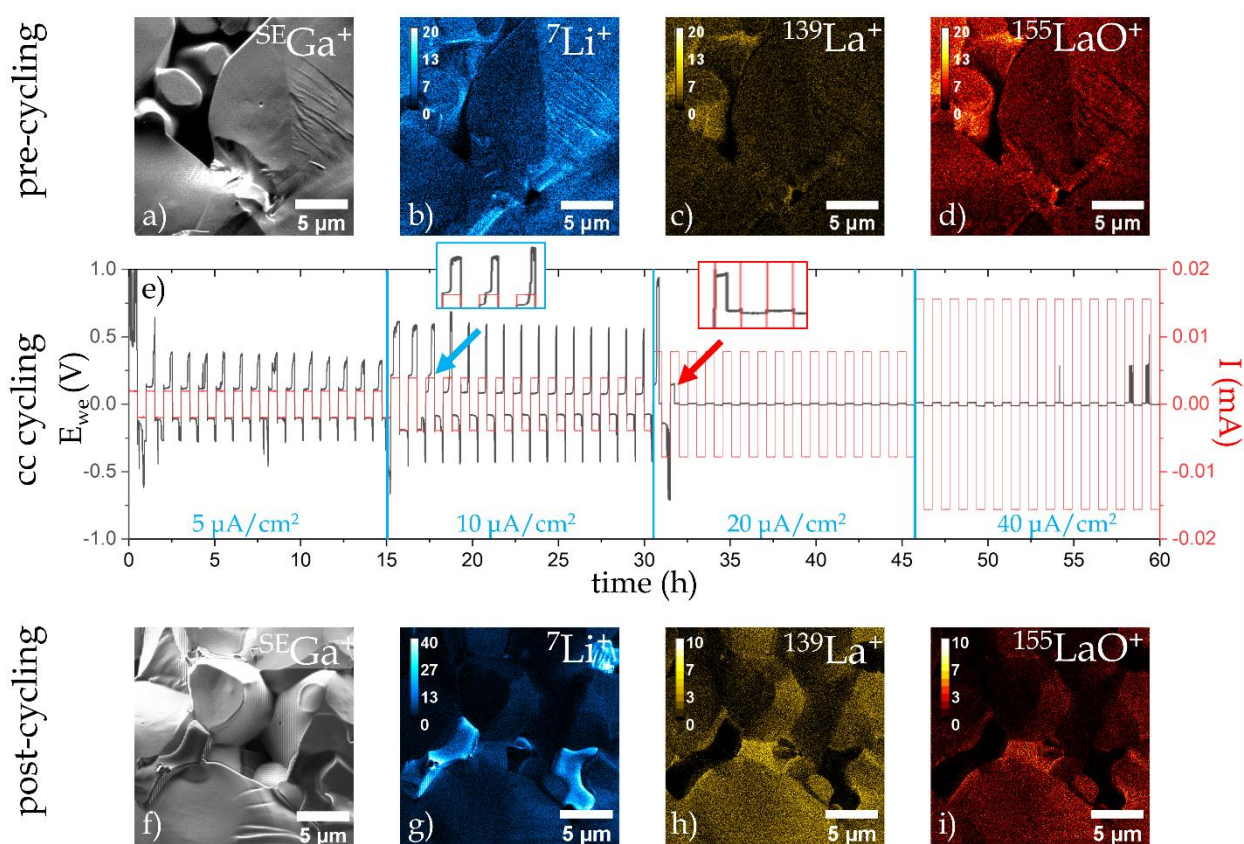


Figure 11: Correlative SIMS analysis in pre-cycled (a-d) and in post-cycled state (f-i). a) and f) show a secondary electron image generated by $^{69}\text{Ga}^+$ irradiation ($E = 30 \text{ keV}$, $I = 0.1 \text{ nA}$, $t_{\text{dwell}} = 2-3 \mu\text{s}$). b-d) and g-i) show elemental maps of $^7\text{Li}^+$, $^{139}\text{La}^+$ and $^{155}\text{LaO}^+$ for both states. e) shows the current and voltage profiles for the 60 cycles = 15 cycles \times 4 different current densities (5, 10, 20 and $40 \mu\text{A}/\text{cm}^2$). During the 2nd cycle of the $20 \mu\text{A}/\text{cm}^2$ current density, the sample short-circuited (red arrow) as indicated by the voltage profile which drops close to zero.⁴²

ions⁵². As a result, it is not possible to achieve SIMS data with perfect homogenous extraction and detection on relatively rough surfaces. However, the relative ratios between the sputter yields of the elements remain unaffected by the surface topography.⁵³

2.2.4.2. CC cycling. Immediately following the pre-cycling analysis, constant current cycling was initiated using four different settings: 5, 10, 20, and $40 \mu\text{A}/\text{cm}^2$,

with 15 cycles for each setting (Figure 11 e). Each full cycle, consisting of charging and discharging, lasted one hour, resulting in a total experiment duration of 60 hours. The observed temporal variations in cell voltage has a typical shape observed in literature and intensively discussed and explained by K.N. Wood et al.⁵⁴ During the initial 15 cycles at 5 $\mu\text{A}/\text{cm}^2$, the voltage range observed was between -0.5 V and 0.5 V. However, the voltage profile displayed slight asymmetry, exhibiting a slight shift towards positive voltages. Cycles 16 to 30 were conducted at 10 $\mu\text{A}/\text{cm}^2$, resulting in a voltage profile ranging from -0.55 V to 0.70 V and a more significant shift towards positive voltages. It is worth noting that at the 18th cycle (the third cycle with a current density of 10 $\mu\text{A}/\text{cm}^2$), the voltage required to maintain the current dropped (indicated by the blue arrow in Figure 11 e). This drop indicates a decrease in resistance, which could be attributed to the nucleation and/or growth of dendrites.

During cycle 32 (the second cycle with a current density of 20 $\mu\text{A}/\text{cm}^2$), a sudden drop in polarization voltage to approximately 0 V occurred, indicating a short-circuit failure of the half-cell (indicated by the red arrow in Figure 11 e). At this point, virtually no potential difference between the electrodes was measured while maintaining a constant current. This suggests that the electrical conductivity of the LLZO pellet abruptly increased during cycling. This abrupt change in electrical properties could result from a compositional change linked to a sudden percolation transition, leading to an inherently higher electrical conductivity than that of pristine LLZO.

2.2.4.3. Post-cycling. After cycling, the sample can be directly analysed in the same instrument without the need to transfer. The structural analysis revealed the presence of a second darker phase at LLZO grain boundaries and in intergranular cavities (see Figure 11 & Figure 12). Multiple regions could be identified where this new phase emerged, e.g. Figure 12 a) shows a region close to the Li/LLZO interface as well as in b) the interior of a pore in the bulk of LLZO, both ROIs elucidating the presence of the new phase. Subsequent SIMS analysis demonstrated a significant increase in the counts of the $^7\text{Li}^+$ signal specifically at the locations corresponding to the dark phase (Figure 11 g). In contrast, no signals were detected for the $^{139}\text{La}^+$ and $^{155}\text{LaO}^+$ ions on this region (Figure 11 h & i). This finding strongly indicates the formation of a new phase consisting of almost pure lithium. XRD measurements performed on a post-mortem LLZO sample (Figure 9) did not reveal any additional peaks compared to the pristine pellet. This observation suggests that the volume fraction of the new phase may be below the detection limit of the XRD technique (<5%). XCT analysis (see Chapter 3) indicated a reduction of porosity fraction from pristine (~2.8%) to post-mortem (~1.0%) LLZO sample, which could be indicative for the volume fraction occupied by the Li-rich phase. (Details on porosity determination in Chapter 3). This emphasizes the importance of conducting chemical imaging at a high resolution. This is enabled by nanoscale SIMS imaging, which enables chemical

mapping with a lateral resolution of 15 nm and a depth resolution of approximately 4 nm.⁹

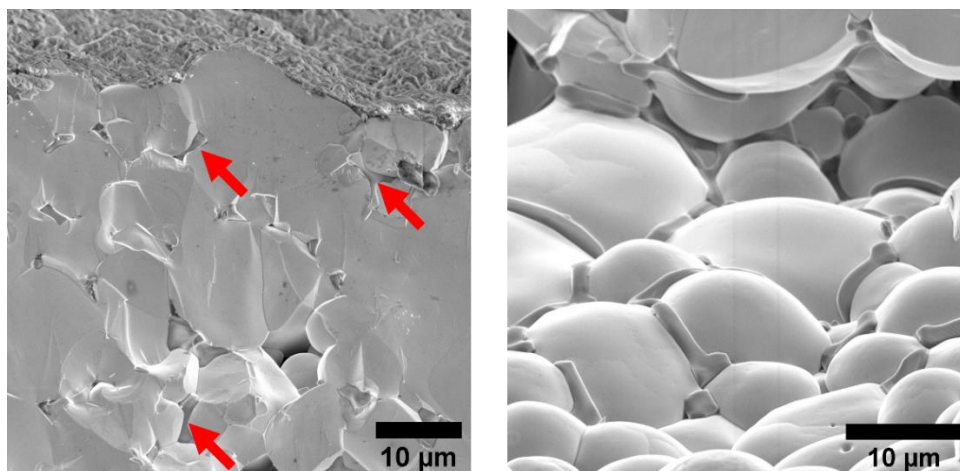


Figure 12: Post-mortem SE images of the LLZO solid electrolyte. a) Regions close to the Li/LLZO interface showed a darker phase in intergranular cavities (red arrows). b) Dark phase between LLZO particles in a crack of the LLZO pellet.

Figure 13 a) and b) present overlays of the elemental maps of ${}^7\text{Li}^+$, ${}^{139}\text{La}^+$, and ${}^{155}\text{LaO}^+$ for the pre- and post-cycled states, respectively (as shown in Figure 11). In the pre-cycled state (Figure 13 a), the chemical distribution of the detected elements appears predominantly homogeneous. The signals have been normalized for a qualitative comparison of the line profiles. In contrast, the post-cycled state (Figure 13 b) confirms the hypothesis of a new phase, as evidenced by a significant increase in the ${}^7\text{Li}^+$ signal and the absence of ${}^{139}\text{La}^+$ and ${}^{155}\text{LaO}^+$. The experimental observations indicate that cycling led to the formation of a new phase. This new phase primarily consists of Li and does not contain detectable amounts of La or LaO. It mainly grows at grain boundaries and intergranular cavities and is below the detection limit of XRD. The formation and growth of this phase has direct impact on the electrochemical properties and is likely responsible for the short-circuit failure (as observed in Figure 11 e).

Comparing the SE images in Figure 11 a) and f), it becomes apparent that a darker phase appeared in the post-cycled analysis. Typically, we would expect higher SE and secondary ion signals due to the high impact angle and increased sputter yields. However, the dark areas in the secondary electron image appear very bright in the chemical map of ${}^7\text{Li}^+$, indicating a high concentration of Li rather than a topographic effect. This confirms that the newly visible structures represent a distinct phase, specifically indicative of a dendrite, and are not merely artifacts resulting from sample topography. Furthermore, the relative ratios of the different elements within this structure significantly differ from those within the LLZO grains.

While similar degradation products have been observed by other researchers after short-circuiting of LLZO-based batteries^{55–58}, our study uniquely detected and

mapped Li on the phase that emerged after cycling. Although numerous factors can influence the reduction from ionic ${}^7\text{Li}^+$ to metallic ${}^7\text{Li}^0$, the diffusion and deposition of Li are likely decisive in this process. So, there is little doubt that the detected Li-rich phase represent Li-dendrites, which must have caused the short-circuit failure, but they must grow from the electrical contacting Li foils to allow the required electrons transported to the side of reducing Li^+ , but they must grow from the electrical contacting Li foils to allow the required electrons transported to the side of reducing Li^+ .

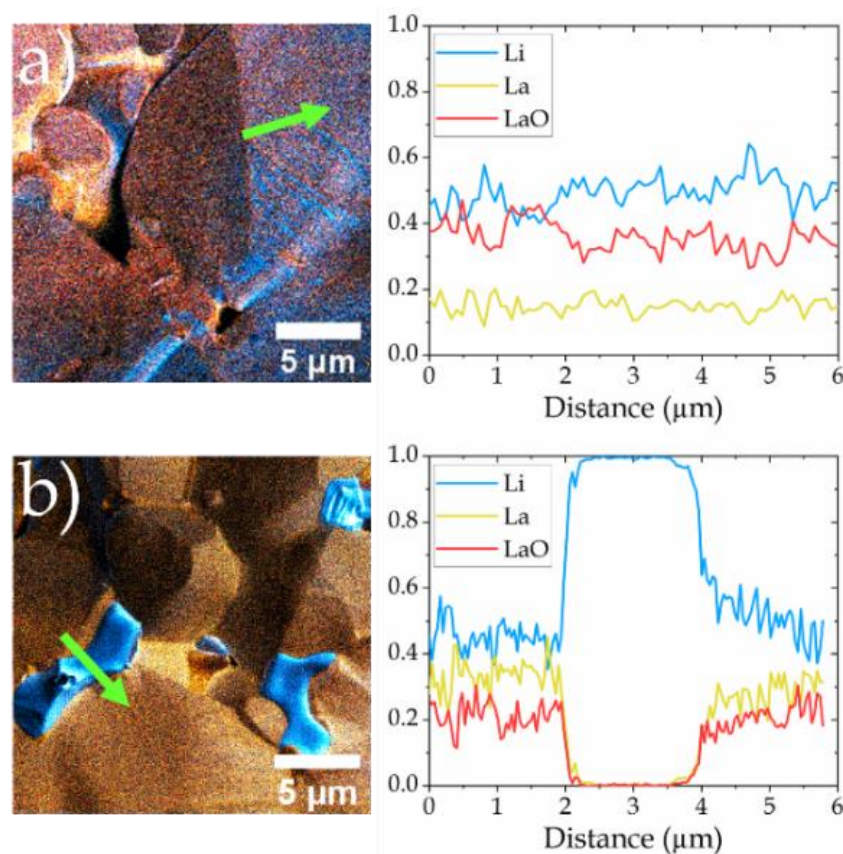


Figure 13: Merged elemental maps (from Figure 11) of ${}^7\text{Li}^+$ (blue), ${}^{139}\text{La}^+$ (yellow) and ${}^{155}\text{LaO}^+$ (red) and corresponding line profiles of the regions indicated by the green arrow in a) for the pre-cycling and in b) for the post-cycled state. The counts for the line profile diagrams have been normalised for a qualitative comparison, hence the relative intensities have been compared to the total (local) counts of every pixel.⁴²

2.2.4.4. Limitations. *Operando* analysis refers to the analysis conducted under operational conditions; however, there are different nuances within this definition. When planning an *operando* analysis, there are two distinct approaches. The first approach involves simultaneous analysis and operation, which we refer to as "dynamic" *operando*. In this approach, the system is continuously analysed while it is in operation. The second approach involves operating the system and then pausing it at a specific moment, effectively freezing the system in its operational state for a limited period. This allows for the analysis to be performed on the system in this static

state. By repeating this process at various stages of operation, we gather data that can be referred to as "static" *operando*.

Our proof-of-concept study classifies as "dynamic" for the SEM analysis, and "static" for the SIMS. The static operation has the drawback that when stopping the experiment, the system seeks electrochemical neutrality and equilibrium, meaning that the system will not be in a perfectly frozen state. However irreversible changes which occurred as a consequence of cycling, will be analysable without the need of a perfectly frozen state. One advantage of the "static" mode is that the analysis and electrochemical cycling are decoupled and therefore the analysis has no influence on the actual operation itself. This is especially true for analyses using electrically charged particles such as ions (or electrons). For "dynamic" *operando* analyses, this interference needs to be understood and considered during data interpretation.²¹ Chapter 5: Neutron Imaging, shows an example of a "dynamic" *operando* approach based on a custom-designed experimental set-up in combination with a neutron beam, which is considered as complementary analysis to the workflow presented in the current chapter.

Given that SIMS is a destructive characterization technique, it is crucial to assess the potential impact of any structural and chemical alterations on the electrochemical properties. One example is the known influence of Ga incorporation on the conductivity of LLZO⁵⁹. In order to investigate the extent of these effects, SRIM⁶⁰ (Stopping and Range of Ions in Matter) simulations were conducted, employing parameters that matched the experimental conditions.

Calculation of the implanted Ga in at.% as a function of sample depth.

→ *Current:*

$$I = 0.3 \text{ nA} = 0.3 \cdot 10^{-9} \frac{\text{C}}{\text{s}}$$

→ *How many ions:*

$$\begin{aligned} & 0.3 \cdot 10^{-9} \frac{\text{C}}{\text{s}} \cdot \frac{1}{e} \\ & = 1.87 \cdot 10^9 \frac{\text{ions}}{\text{s}} \end{aligned}$$

→ *Implementing acquisition time:*

$$\begin{aligned} & 1.87 \cdot 10^9 \frac{\text{ions}}{\text{s}} \cdot 262 \text{ s} \\ & = 4.90 \cdot 10^{11} \text{ ions} \end{aligned}$$

→ *Dose per μm^2 :*

$$30 \times 30 \mu\text{m}^2$$

$$\frac{4.90 \cdot 10^{11} \text{ ions}}{30 \times 30 \mu\text{m}^2}$$

$$\boxed{\text{dose} = 5.45 \cdot 10^8 \frac{\text{ions}}{\mu\text{m}^2}}$$

→ By multiplying the dose with the SRIM output for the simulated ranges $\left[\frac{\text{atoms}/\text{cm}^3}{\text{atoms}/\text{cm}^2} \right]$

$$\rightarrow x \frac{\text{atoms}/\text{cm}^3}{\text{atoms}/\text{cm}^2} \cdot 5.45 \cdot 10^{16} \frac{\text{atoms}}{\text{cm}^2} = y \frac{\text{atoms}}{\text{cm}^3}$$

→ if we now divide y by the total number of $\frac{\text{atoms}}{\text{cm}^3}$ which are present in a material with a density of $5.1 \frac{\text{g}}{\text{cm}^3}$ ($\sim 7.3 \cdot 10^{11} \frac{\text{atoms}}{\mu\text{m}^3}$), we obtain the at. % – fraction of implanted Ga atoms as a function of depth (Figure 15 a).

The results of these simulations reveal that the depth of the sample affected by the ion beam is approximately 30 nm, and the maximum concentration of Ga implanted is around 3.7 at.% (Figure 15 a). The maximum volume affected in this study is calculated to be approximately $27 \mu\text{m}^3$ per SIMS acquisition, considering a size of approximately $30 \times 30 \mu\text{m}^2$ and a depth of $0.03 \mu\text{m}$. In comparison, the volume of the LLZO pellet is approximately 59.39 mm^3 , which is nine orders of magnitude larger. As a result, it can be concluded that the volume affected by SIMS analysis, as well as the Ga implantation, is negligible. Therefore, the analysis does not significantly alter the overall structure or chemistry of the sample, however locally in the image area it could.

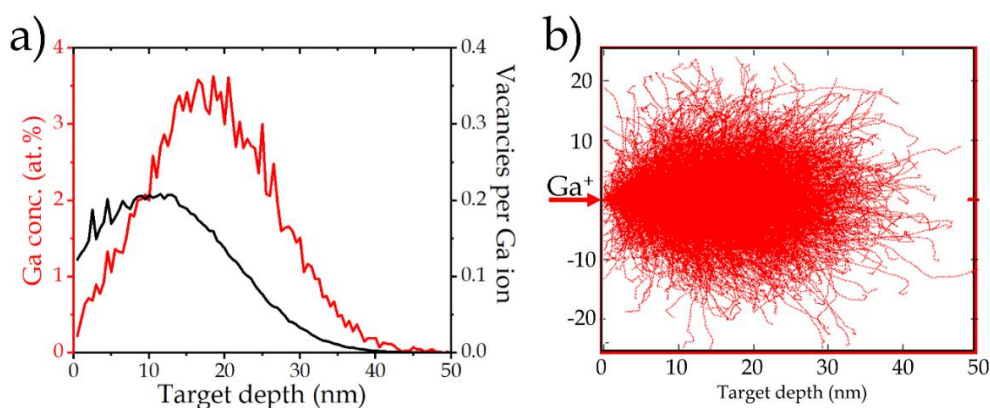


Figure 14: a) Concentration profile of implanted Ga (red) and number of created vacancies per Ga ion (black). b) Primary ion trajectories (Ga^+) in an amorphous LLZO phase (density 5.1 g/cm^3). Both axes represent distances, the arrow shows the location of ion impact and the red lines in the diagram represent individual trajectories of 10^4 Ga-ions travelling inside the LLZO phase.⁴²

2.2.4.5. Discussion

In this chapter⁴², we focussed is primarily on two extreme cases: the pristine state and the short-circuited end state. However, the experimental design allows for the cycling process to be paused at any given moment to conduct structural and chemical analysis before resuming the cycling. By examining multiple stages during the cycling process, we can study the evolution of irreversible structural and chemical alterations. For this proof-of-concept study, it was crucial to push the half-cell to a point where such alterations, as those occurring in a short-circuit, would become most clearly visible.

Our method can also be employed without modifications to track the degradation of the battery over multiple time steps. The *operando* methodology presented here opens opportunities for various studies aiming to correlate electrochemical, structural, and chemical data from the same sample without the need for transferring between different instruments. Additionally, the inclusion of SIMS in this workflow is particularly advantageous for battery research. SIMS has the capability to detect and analyse low-Z elements like Li, which are challenging to study using conventional techniques but are essential components of many batteries.

In addition to the *operando* capability of the custom-designed sample holder, there are other appealing features that make this design and methodology attractive. As mentioned under "Pressure Control," the force exerted by the springs (or the pressure applied to the contacts) can be controlled and adjusted. This allows for pressure-dependent studies and the ability to influence the impedance of the electrode-solid electrolyte interface, as observed in Figure 3 b). It also enables consistent experimental conditions when analysing multiple samples.

While this work was conducted with a solid-state half-cell, the sample holder design and the overall workflow are equally applicable to full battery cells. By adapting the pressure applied to the sample, solid polymer electrolytes and gel systems could be considered for analysis. Furthermore, this setup has potential applications beyond battery research. For instance, it could be applied to the analysis of photovoltaic materials^{61,62}, piezoelectric materials, or any materials with pressure-dependent and/or electrochemistry-related processes.

2.3 Closing Remarks

In this chapter we presented the design, and proof of concept of a correlative FIB-SEM-SIMS-based *operando* workflow with a Li/LLZO/Li solid state half-cell.

First, the capabilities and the importance of the FIB-SEM-SIMS instrument, but also other correlative workflows for battery analysis are explained.

The necessity for *operando* workflows introduces the next subchapter, followed by a sample holder prototype design. Different tests and proof of concept measurements to validate the prototype were discussed. Sample composition and sample preparation in context of the correlative *operando* workflow were presented. The final subchapter explains the full workflow and shows results of a Li/LLZO/Li half-cell which was: 1) structurally (SEM) and chemically (SIMS) analysed, then 2) cycled inside the instrument until short-circuit failure and then 3) post-mortem analysed (SEM-SIMS).

Considering that our conclusions are derived from a restricted number of examined samples, it is important to approach the interpretations with caution. The fact that only very low current densities were achievable with the experimental arrangement emphasizes the requirement for additional optimization, not only regarding the components under investigation but also concerning the cell and sample holder configuration. Nevertheless, these aspects are currently being actively pursued in ongoing research. For this study, however, our primary objective has been to establish a proof of concept for the *operando* workflow.

The following significant steps for improvement would be: 1) first, observe degradation artefacts grow over multiple cycles in static mode and 2) upgrade the instrumental set-up for a full dynamic *operando* analysis. These studies are already in progress. As for the moment only the SEM is in dynamic *operando* mode, but SIMS is restricted to static operation. We are in the process of upgrading the set-up and the workflow to perform fully *operando* SIMS soon.

The presented correlative workflow is an unprecedented technique which successfully demonstrated the direct relation between structure, chemical composition, and electrochemical performance.

In the context of the model sample shown in Figure 2, we note that this chapter focusses on the solid-state electrolyte in the context of short circuit failure degradation i.e. Li-diffusion, dendrites. The next chapter combines X-ray based techniques with SEM-SIMS, complementing the analytical capability for the analysis of all the components of a SSB.

ANNEXE 1

The EIS measurements were done in potentiostatic mode in a frequency range from 1 MHz to 1 Hz with an amplitude of 5 mV. Generally, for simple Li/LLZO/Li systems from high to low frequencies, the resistances should appear from left to right in the following order: R_b bulk resistance, R_{gb} grain boundary resistance, $R_{SE/Li}$ interface resistance. From literature it is known that the bulk resistance is only accessible in frequency ranges above 1 MHz. As our set-up allows only a maximum frequency of 1 MHz, the bulk resistance is not accessible in the measured range. However, in Figure 3 b) a third semi-circle (impedance at low frequencies) of unidentified origin is needed to fit the experimental data. A detailed investigation of this is beyond the scope of this study.

Table 1: Fit parameters for impedance spectroscopy of a symmetric Li/LLZO/Li cell shown in Figure 3 b (Pressure dependant EIS). R represents an ohmic resistor and CPE a constant phase element. The indices are gb: grain boundary, SE/Li: Solid electrolytes/Li-electrode and u: unidentified. The exponent for the CPE is denoted as n .

Pressure dependant EIS			
name	value	fit error	unit
R_{gb}	707.733	16.201	Ω
CPE_{gb}	1.32E-09	2.65E-10	$F \cdot s^{(n-1)}$
n_{gb}	0.899	0.013	/
$R_{SE/Li}$	14978.706	2030.624	Ω
$CPE_{SE/Li}$	4.07E-08	3.57E-09	$F \cdot s^{(n-1)}$
$n_{SE/Li}$	0.860	0.019	/
R_u	9146.892	2100.510	Ω
CPE_u	1.08E-06	2.91E-07	$F \cdot s^{(n-1)}$
n_u	0.702	0.035	/

Table 2: Fit parameters for impedance spectroscopy of the Operando – Swagelok comparison from Figure 8. R represents an ohmic resistor and CPE a constant phase element. The indices are gb: grain boundary and SE/Li: Solid electrolytes/Li-electrode. The exponent for the CPE is denoted as n .

Fit Operando Holder			
name	value	fit error	unit
R_{gb}	552.16	9.89	Ω
CPE_{gb}	3.605E-10	1.42E-10	$F \cdot s^{(n-1)}$
n_{gb}	1	0.0261	/
$R_{SE/Li}$	7426.8	85	Ω
$CPE_{SE/Li}$	3.76E-07	2.97E-08	$F \cdot s^{(n-1)}$
$n_{SE/Li}$	0.78233	0.00874	/

Fit Swagelok Holder			
name	value	fit error	unit
R_{gb}	584.01	8.63	Ω
CPE_{gb}	3.366E-10	1.08E-10	$F \cdot s^{(n-1)}$
n_{gb}	1	0.0212	/
$R_{SE/Li}$	8190.6	78.5	Ω
$CPE_{SE/Li}$	4.095E-07	2.58E-08	$F \cdot s^{(n-1)}$
$n_{SE/Li}$	0.77243	0.00708	/

References

- (1) Eng, A. Y. S.; Soni, C. B.; Lum, Y.; Khoo, E.; Yao, Z.; Vineeth, S. K.; Kumar, V.; Lu, J.; Johnson, C. S.; Wolverton, C.; Seh, Z. W. *Theory-guided experimental design in battery materials research. Sci Adv* **2022**, *8*, eabm2422.
- (2) Fichtner, M.; Edström, K.; Ayerbe, E.; Berecibar, M.; Bhowmik, A.; Castelli, I. E.; Clark, S.; Dominko, R.; Erakca, M.; Franco, A. A.; Grimaud, A.; Horstmann, B.; Latz, A.; Lormann, H.; Meeus, M.; Narayan, R.; Pammer, F.; Ruhland, J.; Stein, H.; Vegge, T.; Weil, M. *Rechargeable Batteries of the Future—The State of the Art from a BATTERY 2030+ Perspective. Adv. Energy Mater.* **2022**, *12*, 2102904.
- (3) Goodenough, J. B.; Kim, Y. *Challenges for Rechargeable Li Batteries. Chem. Mater.* **2010**, *22*, 587–603.
- (4) Hatzell, K. B.; Chen, X. C.; Cobb, C. L.; Dasgupta, N. P.; Dixit, M. B.; Marbella, L. E.; McDowell, M. T.; Mukherjee, P. P.; Verma, A.; Viswanathan, V.; Westover, A. S.; Zeier, W. G. *Challenges in Lithium Metal Anodes for Solid-State Batteries. ACS Energy Lett.* **2020**, *5*, 922–934.
- (5) Ma, J.; Li, Y.; Grundish, N. S.; Goodenough, J. B.; Chen, Y.; Guo, L.; Peng, Z.; Qi, X.; Yang, F.; Qie, L.; Wang, C.-A.; Huang, B.; Huang, Z.; Chen, L.; Su, D.; Wang, G.; Peng, X.; Chen, Z.; Yang, J.; He, S.; Zhang, X.; Yu, H.; Fu, C.; Jiang, M.; Deng, W.; Sun, C.-F.; Pan, Q.; Tang, Y.; Li, X.; Ji, X.; Wan, F.; Niu, Z.; Lian, F.; Wang, C.; Wallace, G. G.; Fan, M.; Meng, Q.; Xin, S.; Guo, Y.-G.; Wan, L.-J. *The 2021 battery technology roadmap. J. Phys. D: Appl. Phys.* **2021**, *54*, 183001.
- (6) Manthiram, A. *A reflection on lithium-ion battery cathode chemistry. Nat Commun* **2020**, *11*, 1550.
- (7) Boebinger, M. G.; Lewis, J. A.; Sandoval, S. E.; McDowell, M. T. *Understanding Transformations in Battery Materials Using in Situ and Operando Experiments: Progress and Outlook. ACS Energy Lett.* **2020**, *5*, 335–345.
- (8) Zhu, J.; Shen, H.; Shi, X.; Yang, F.; Hu, X.; Zhou, W.; Yang, H.; Gu, M. *Revealing the Chemical and Structural Evolution of V2O5 Nanoribbons in Lithium-Ion Batteries Using in Situ Transmission Electron Microscopy. Anal Chem* **2019**, *91*, 11055–11062.
- (9) De Castro, O.; Audinot, J.-N.; Hoang, H. Q.; Coulbary, C.; Bouton, O.; Barrahma, R.; Ost, A.; Stoffels, C.; Jiao, C.; Dutka, M.; Geryk, M.; Wirtz, T. *Magnetic Sector Secondary Ion Mass Spectrometry on FIB-SEM Instruments for Nanoscale Chemical Imaging. Anal Chem* **2022**, *94*, 10754–10763.
- (10) Benayad, A.; Morales-Ugarte, J. E.; Santini, C. C.; Bouchet, R. *Operando XPS: A Novel Approach for Probing the Lithium/Electrolyte Interphase Dynamic Evolution. J Phys Chem A* **2021**, *125*, 1069–1081.
- (11) Masuda, H.; Ishida, N.; Ogata, Y.; Ito, D.; Fujita, D. *In situ visualization of Li concentration in all-solid-state lithium ion batteries using time-of-flight secondary ion mass spectrometry. Journal of Power Sources* **2018**, *400*, 527–532.
- (12) Mathayan, V.; Morita, K.; Tsuchiya, B.; Ye, R.; Baba, M.; Primetzhofer, D. *Sensitive in-operando observation of Li and O transport in thin-film Li-ion batteries. Materials Today Energy* **2021**, *21*, 100844.
- (13) Mathayan, V.; Moro, M. V.; Morita, K.; Tsuchiya, B.; Ye, R.; Baba, M.; Primetzhofer, D. *In-operando observation of Li depth distribution and Li transport in thin film Li ion batteries. Appl. Phys. Lett.* **2020**, *117*, 23902.
- (14) Mirolo, M.; Leanza, D.; Höltzchi, L.; Jordy, C.; Pelé, V.; Novák, P.; El Kazzi, M.; Vaz, C. A. F. *Post Mortem and Operando XPEEM: a Surface-Sensitive Tool for Studying Single Particles in Li-Ion Battery Composite Electrodes. Anal Chem* **2020**, *92*, 3023–3031.

- (15) Otoyama, M.; Kowada, H.; Sakuda, A.; Tatsumisago, M.; Hayashi, A. *Operando Confocal Microscopy for Dynamic Changes of Li⁺ Ion Conduction Path in Graphite Electrode Layers of All-Solid-State Batteries*. *J Phys Chem Lett* **2020**, *11*, 900–904.
- (16) Wood, K. N.; Steirer, K. X.; Hafner, S. E.; Ban, C.; Santhanagopalan, S.; Lee, S.-H.; Teeter, G. *Operando X-ray photoelectron spectroscopy of solid electrolyte interphase formation and evolution in Li₂S-P₂S₅ solid-state electrolytes*. *Nat Commun* **2018**, *9*, 2490.
- (17) Yamagishi, Y.; Morita, H.; Nomura, Y.; Igaki, E. *Visualizing Lithiation of Graphite Composite Anodes in All-Solid-State Batteries Using Operando Time-of-Flight Secondary Ion Mass Spectrometry*. *J Phys Chem Lett* **2021**, *12*, 4623–4627.
- (18) Zhang, C.; Feng, Y.; Han, Z.; Gao, S.; Wang, M.; Wang, P. *Electrochemical and Structural Analysis in All-Solid-State Lithium Batteries by Analytical Electron Microscopy: Progress and Perspectives*. *Adv Mater* **2020**, *32*, e1903747.
- (19) Ihrig, M.; Kuo, L.-Y.; Lobe, S.; Laptev, A. M.; Lin, C.-A.; Tu, C.-H.; Ye, R.; Kaghazchi, P.; Cressa, L.; Eswara, S.; Lin, S.-K.; Guillon, O.; Fattakhova-Rohlfing, D.; Finsterbusch, M. *Thermal Recovery of the Electrochemically Degraded LiCoO₂/Li₇La₃Zr₂O₁₂:Al,Ta Interface in an All-Solid-State Lithium Battery*. *ACS Appl Mater Interfaces* **2023**, *15*, 4101–4112.
- (20) López, I.; Morey, J.; Ledeuil, J. B.; Madec, L.; Martinez, H. *A critical discussion on the analysis of buried interfaces in Li solid-state batteries. Ex situ and in situ / operando studies*. *J. Mater. Chem. A* **2021**, *9*, 25341–25368.
- (21) Blondeau, L.; Surblé, S.; Foy, E.; Khodja, H.; Belin, S.; Gauthier, M. *Are Operando Measurements of Rechargeable Batteries Always Reliable? An Example of Beam Effect with a Mg Battery*. *Anal Chem* **2022**, *94*, 9683–9689.
- (22) Audinot, J.-N.; Philipp, P.; Castro, O. de; Biesemeier, A.; Hoang, Q. H.; Wirtz, T. *Highest resolution chemical imaging based on secondary ion mass spectrometry performed on the helium ion microscope*. *Rep Prog Phys* **2021**, *84*.
- (23) Andersen, D.; Chen, H.; Pal, S.; Cressa, L.; Castro, O. de; Wirtz, T.; Schmitz, G.; Eswara, S. *Correlative high-resolution imaging of hydrogen in Mg₂Ni hydrogen storage thin films*. *International Journal of Hydrogen Energy* **2023**, *48*, 13943–13954.
- (24) Cressa, L.; Fell, J.; Pauly, C.; Hoang, Q. H.; Mücklich, F.; Herrmann, H.-G.; Wirtz, T.; Eswara, S. *A FIB-SEM Based Correlative Methodology for X-Ray Nanotomography and Secondary Ion Mass Spectrometry: An Application Example in Lithium Batteries Research*. *Microsc Microanal* **2022**, *28*, 1890–1895.
- (25) Sui, T.; Song, B.; Dluhos, J.; Lu, L.; Korsunsky, A. M. *Nanoscale chemical mapping of Li-ion battery cathode material by FIB-SEM and TOF-SIMS multi-modal microscopy*. *Nano Energy* **2015**, *17*, 254–260.
- (26) Bernuy-Lopez, C.; Manalastas, W.; Del Lopez Amo, J. M.; Aguadero, A.; Aguesse, F.; Kilner, J. A. *Atmosphere Controlled Processing of Ga-Substituted Garnets for High Li-Ion Conductivity Ceramics*. *Chem. Mater.* **2014**, *26*, 3610–3617.
- (27) Buschmann, H.; Dölle, J.; Berendts, S.; Kuhn, A.; Bottke, P.; Wilkening, M.; Heitjans, P.; Senyshyn, A.; Ehrenberg, H.; Lotnyk, A.; Duppel, V.; Kienle, L.; Janek, J. *Structure and dynamics of the fast lithium ion conductor "Li₇La₃Zr₂O₁₂"*. *Phys Chem Chem Phys* **2011**, *13*, 19378–19392.
- (28) Chen, Y.-T.; Jena, A.; Pang, W. K.; Peterson, V. K.; Sheu, H.-S.; Chang, H.; Liu, R.-S. *Voltammetric Enhancement of Li-Ion Conduction in Al-Doped Li_{7-x}La₃Zr₂O₁₂ Solid Electrolyte*. *J. Phys. Chem. C* **2017**, *121*, 15565–15573.
- (29) Krauskopf, T.; Hartmann, H.; Zeier, W. G.; Janek, J. *Toward a Fundamental Understanding of the Lithium Metal Anode in Solid-State Batteries-An Electrochemo-Mechanical Study on the Garnet-Type Solid Electrolyte Li_{6.25}Al_{0.25}La₃Zr₂O₁₂*. *ACS Appl Mater Interfaces* **2019**, *11*, 14463–14477.

- (30) Kumazaki, S.; Iriyama, Y.; Kim, K.-H.; Murugan, R.; Tanabe, K.; Yamamoto, K.; Hirayama, T.; Ogumi, Z. *High lithium ion conductive Li₇La₃Zr₂O₁₂ by inclusion of both Al and Si. Electrochemistry Communications* **2011**, *13*, 509–512.
- (31) Pesci, F. M.; Brugge, R. H.; Hekselman, A. K. O.; Cavallaro, A.; Chater, R. J.; Agüadero, A. *Elucidating the role of dopants in the critical current density for dendrite formation in garnet electrolytes. J. Mater. Chem. A* **2018**, *6*, 19817–19827.
- (32) Renna, L. A.; Blanc, F.-G.; Giordani, V. *Interface Modification of lithium Metal Anode and Solid-state Electrolyte with Gel Electrolyte. J. Electrochem. Soc.* **2020**, *167*, 70542.
- (33) Vadha, P.; Hu, J.; Johnson, M. J.; Stocker, R.; Braglia, M.; Brett, D. J. L.; Rettie, A. J. E. *Electrochemical Impedance Spectroscopy for All-Solid-State Batteries: Theory, Methods and Future Outlook. ChemElectroChem* **2021**, *8*, 1930–1947.
- (34) Vivier, V.; Orazem, M. E. *Impedance Analysis of Electrochemical Systems. Chem Rev* **2022**, *122*, 11131–11168.
- (35) Wang, C.; Fu, K.; Kammampata, S. P.; McOwen, D. W.; Samson, A. J.; Zhang, L.; Hitz, G. T.; Nolan, A. M.; Wachsman, E. D.; Mo, Y.; Thangadurai, V.; Hu, L. *Garnet-Type Solid-State Electrolytes: Materials, Interfaces, and Batteries. Chem Rev* **2020**, *120*, 4257–4300.
- (36) Daubinger, P.; Göttlinger, M.; Hartmann, S.; Giffin, G. A. *Consequences of Different Pressures and Electrolytes on the Irreversible Expansion of Lithium Metal Half Cells. Batteries & Supercaps* **2022**.
- (37) Huang, Y.; He, Y.; Sheng, H.; Lu, X.; Dong, H.; Samanta, S.; Dong, H.; Li, X.; Kim, D. Y.; Mao, H.-K.; Liu, Y.; Li, H.; Wang, L. *Li-ion battery material under high pressure: amorphization and enhanced conductivity of Li₄Ti₅O₁₂. Natl Sci Rev* **2019**, *6*, 239–246.
- (38) Müller, V.; Scurtu, R.-G.; Memm, M.; Danzer, M. A.; Wohlfahrt-Mehrens, M. *Study of the influence of mechanical pressure on the performance and aging of Lithium-ion battery cells. Journal of Power Sources* **2019**, *440*, 227148.
- (39) Sakka, Y.; Yamashige, H.; Watanabe, A.; Takeuchi, A.; Uesugi, M.; Uesugi, K.; Orikasa, Y. *Pressure dependence on the three-dimensional structure of a composite electrode in an all-solid-state battery. J. Mater. Chem. A* **2022**, *10*, 16602–16609.
- (40) Schiele, A.; Hatsukade, T.; Berkes, B. B.; Hartmann, P.; Brezesinski, T.; Janek, J. *High-Throughput in Situ Pressure Analysis of Lithium-Ion Batteries. Anal Chem* **2017**, *89*, 8122–8128.
- (41) Ferrovac AG. <https://www.ferrovac.com/>.
- (42) Cressa, L.; Sun, Y.; Andersen, D.; Gerard, M.; Castro, O. de; Kopljar, D.; Nojabae, M.; Friedrich, K. A.; Schmitz, G.; Wirtz, T.; Eswara, S. *Toward Operando Structural, Chemical, and Electrochemical Analyses of Solid-State Batteries Using Correlative Secondary Ion Mass Spectrometry Imaging. Anal Chem* **2023**.
- (43) Zhang, X.; Oh, T.-S.; Fergus, J. W. *Densification of Ta-Doped Garnet-Type Li_{6.75}La₃Zr_{1.75}Ta_{0.25}O₁₂ Solid Electrolyte Materials by Sintering in a Lithium-Rich Air Atmosphere. J. Electrochem. Soc.* **2019**, *166*, A3753–A3759.
- (44) Jiang, Y.; Zhou, Y.; Hu, Z.; Huang, Y.; Zhu, X. *MgO or Al₂O₃ crucible: Which is better for the preparation of LLZ-based solid electrolytes? Ceramics International* **2020**, *46*, 3367–3373.
- (45) Ganesh Kumar, K.; Balaji Bhargav, P.; Balaji, C.; Nafis, A.; Aravindh, K.; Ramasamy, P. *Effect of Sintering on Structural Modification and Phase Transition of Al-Substituted LLZO Electrolytes for Solid State Battery Applications. Journal of Electrochemical Energy Conversion and Storage* **2021**, *18*.
- (46) Schindelin, J.; Arganda-Carreras, I.; Frise, E.; Kaynig, V.; Longair, M.; Pietzsch, T.; Preibisch, S.; Rueden, C.; Saalfeld, S.; Schmid, B.; Tinevez, J.-Y.; White, D. J.; Hartenstein, V.; Eliceiri, K.; Tomancak, P.; Cardona, A. *Fiji: an open-source platform for biological-image analysis. Nat Methods* **2012**, *9*, 676–682.

- (47) Sigmund, P. *Theory of Sputtering. I. Sputtering Yield of Amorphous and Polycrystalline Targets*. *Phys. Rev.* **1969**, *184*, 383–416.
- (48) Arredondo, R.; Oberkofler, M.; Schwarz-Selinger, T.; Toussaint, U. von; Burwitz, V. V.; Mutzke, A.; Vassallo, E.; Pedroni, M. *Angle-dependent sputter yield measurements of keV D ions on W and Fe and comparison with SDTrimSP and SDTrimSP-3D*. *Nuclear Materials and Energy* **2019**, *18*, 72–76.
- (49) Ost, A. D.; Wu, T.; Höschel, C.; Mueller, C. W.; Wirtz, T.; Audinot, J.-N. *4D Surface Reconstructions to Study Microscale Structures and Functions in Soil Biogeochemistry*. *Environ Sci Technol* **2021**, *55*, 9384–9393.
- (50) Stepanova, M.; Dew, S. K.; Soshnikov, I. P. *Sputtering from ion-beam-roughened Cu surfaces*. *Phys. Rev. B* **2002**, *66*.
- (51) Warmoltz, N.; Werner, H. W.; Morgan, A. E., *The Bombardment Angle Dependence of the Sputtering and Secondary Ion Yield for Oxygen Ion Bombardment of Silicon*. In *Secondary Ion Mass Spectrometry SIMS II*; Goldanskii, Vitalii I.; Gomer, Robert; Schäfer, Fritz Peter; Toennies, J. Peter; Benninghoven, A.; Evans, C. A.; Powell, R. A.; Shimizu, R.; Storms, H. A., Eds.; Springer Berlin Heidelberg: Berlin, Heidelberg, 1979.
- (52) Tetsuya, M.; Yoshikazu, H. *The effect of low glancing angle sputtering on depth resolution in secondary ion mass spectrometry*. *Nuclear Instruments and Methods in Physics Research Section B: Beam Interactions with Materials and Atoms* **1988**, *33*, 556–559.
- (53) Ost, A. D. *INVESTIGATION OF SURFACE SPUTTERING AND IONIZATION PROCESSES UNDER NON-REACTIVE LIGHT ION IRRADIATION: TOWARDS 4D SIMS IMAGING*, 07 December 2022.
- (54) Wood, K. N.; Kazyak, E.; Chadwick, A. F.; Chen, K.-H.; Zhang, J.-G.; Thornton, K.; Dasgupta, N. P. *Dendrites and Pits: Untangling the Complex Behavior of Lithium Metal Anodes through Operando Video Microscopy*. *ACS Cent Sci* **2016**, *2*, 790–801.
- (55) Porz, L.; Swamy, T.; Sheldon, B. W.; Rettenwander, D.; Frömling, T.; Thaman, H. L.; Berendts, S.; Uecker, R.; Carter, W. C.; Chiang, Y.-M. *Mechanism of Lithium Metal Penetration through Inorganic Solid Electrolytes*. *Adv. Energy Mater.* **2017**, *7*, 1701003.
- (56) Ren, Y.; Shen, Y.; Lin, Y.; Nan, C.-W. *Direct observation of lithium dendrites inside garnet-type lithium-ion solid electrolyte*. *Electrochemistry Communications* **2015**, *57*, 27–30.
- (57) Sudo, R.; Nakata, Y.; Ishiguro, K.; Matsui, M.; Hirano, A.; Takeda, Y.; Yamamoto, O.; Imanishi, N. *Interface behavior between garnet-type lithium-conducting solid electrolyte and lithium metal*. *Solid State Ionics* **2014**, *262*, 151–154.
- (58) Umegaki, I.; Higuchi, Y.; Kondo, Y.; Ninomiya, K.; Takeshita, S.; Tampo, M.; Nakano, H.; Oka, H.; Sugiyama, J.; Kubo, M. K.; Miyake, Y. *Nondestructive High-Sensitivity Detections of Metallic Lithium Deposited on a Battery Anode Using Muonic X-rays*. *Anal Chem* **2020**, *92*, 8194–8200.
- (59) Jalem, R.; Rushton, M.; Manalastas, W.; Nakayama, M.; Kasuga, T.; Kilner, J. A.; Grimes, R. W. *Effects of Gallium Doping in Garnet-Type $\text{Li}_7\text{La}_3\text{Zr}_2\text{O}_{12}$ Solid Electrolytes*. *Chem. Mater.* **2015**, *27*, 2821–2831.
- (60) Ziegler, J. F.; Ziegler, M. D.; Biersack, J. P. *SRIM – The stopping and range of ions in matter (2010)*. *Nuclear Instruments and Methods in Physics Research Section B: Beam Interactions with Materials and Atoms* **2010**, *268*, 1818–1823.
- (61) Eswara, S.; Pshenova, A.; Lentzen, E.; Nogay, G.; Lehmann, M.; Ingenito, A.; Jeangros, Q.; Haug, F.-J.; Valle, N.; Philipp, P.; Hessler-Wyser, A.; Wirtz, T. *A method for quantitative nanoscale imaging of dopant distributions using secondary ion mass spectrometry: an application example in silicon photovoltaics*. *MRS Communications* **2019**, *9*, 916–923.
- (62) Usiobo, O. J.; Kanda, H.; Gratia, P.; Zimmermann, I.; Wirtz, T.; Nazeeruddin, M. K.; Audinot, J.-N. *Nanoscale Mass-Spectrometry Imaging of Grain Boundaries in Perovskite Semiconductors*. *J. Phys. Chem. C* **2020**, *124*, 23230–23236.

CHAPTER 3

1. CHAPTER 1 Background
2. CHAPTER 2 Correlative SEM/SIMS
3. CHAPTER 3 X-ray Based Correlative Approaches
 - 3.1. Motivation
 - 3.2. μ CT for Solid State Electrolyte
 - 3.2.1. μ CT Analysis
 - 3.2.2. SIMS Analysis
 - 3.2.3. Results & Discussion
 - 3.3. NanoCT for Cathode Material
 - 3.3.1. Sample preparation
 - 3.3.2. NanoCT Analysis
 - 3.3.3. SIMS Analysis
 - 3.3.4. Results & Discussion
 - 3.3.5. Conclusion
 - 3.4. EDX & WDXS for composite LLZO-Cathode
 - 3.4.1. Sample preparation
 - 3.4.2. EDX Analysis
 - 3.4.3. WDXS Analysis
 - 3.4.4. SIMS Analysis
 - 3.4.5. Results & Discussion
 - 3.4.6. Case Study
 - 3.5. Closing Remarks

3. X-ray based Correlative Approaches

3.1 Motivation

In the previous chapters we saw and discussed how powerful correlative SEM/SIMS can be when studying solid-state Li-ion battery materials. Nonetheless, as this is a pure surface sensitive technique (for structural and chemical analysis), X-ray based analysis can serve as complementary technique. For example, in this chapter μ CT is used to reconstruct 3D volumes of LLZO samples to study porosities, and nanoCT (high resolution XCT inside a SEM) in combination with SIMS is used to study cathodic material. Additionally, a correlative EDX, WDXS and SIMS approach is demonstrated to investigate the complex 3D solid-electrolyte-cathode interface (LLZO/LCO), this is rounded up by a case study.

These examples prove that X-ray based techniques can be an excellent complementary technique to SEM/SIMS, opening doors for many interesting studies including 3D bulk information (nanoCT & μ CT), and for chemical quantification (EDX & WDXS). On top of that, the combination of X-ray based techniques with SIMS allows to study all components of an ASSB from the anode through solid electrolyte to the cathode.

3.2 μ CT for Solid State Electrolyte Analysis

3.2.1 μ CT Analysis

Micro-computed X-ray Tomography (μ CT) is a non-destructive analysis method used to visualize the bulk structures of solid objects by generating 3D reconstruction of the microstructure. μ CT testing was performed to visualize the internal structure of the solid electrolyte material, revealing density contrast at the micron scale. To this end, an X-ray cone beam equipment EasyTom 160 from RX Solutions (Chavanod, France) with a voltage of 60 kV between anode (=tungsten target) and cathode (=cone), and 200 mA with a micro-focused tube (tungsten filament, small focus spot mode), were used. The generated polychromatic X-rays are in an energy range between 58 keV¹. The source-to-detector distance (SDD) and the source-to-object distance (SOD) were set to 422.5 mm and 3.8 mm, respectively, enabling to get a voxel size of around 1 μ m. The detector was a 16-bit flat panel imager with a total pixel area of 1920 pixels \times 1536 pixels. The frame rate was set to 0.5 s⁻¹ to record one projection. 1440 projections were recorded over 360° with a step of 0.25°. The 3D reconstruction of the sample volume into stacked slices has been conducted with the software Xact64 (RX Solutions, Chavanod, France) after applying a sample movement correction (spot deviation module), a system misalignment correction (geometry correction module) and a ring filter (5 pixels) to the 1440 projections. The analysis of the stacked slices was conducted with the software Avizo (Konrad-Zuse-Zentrum Berlin/FEI SAS-Thermo Fisher Scientific, Waltham, MA, United States). The following procedure was applied:

median filter (3D mode) to facilitate the segmentation, grey-level segmentation to isolate the pores, quantification of the pores.

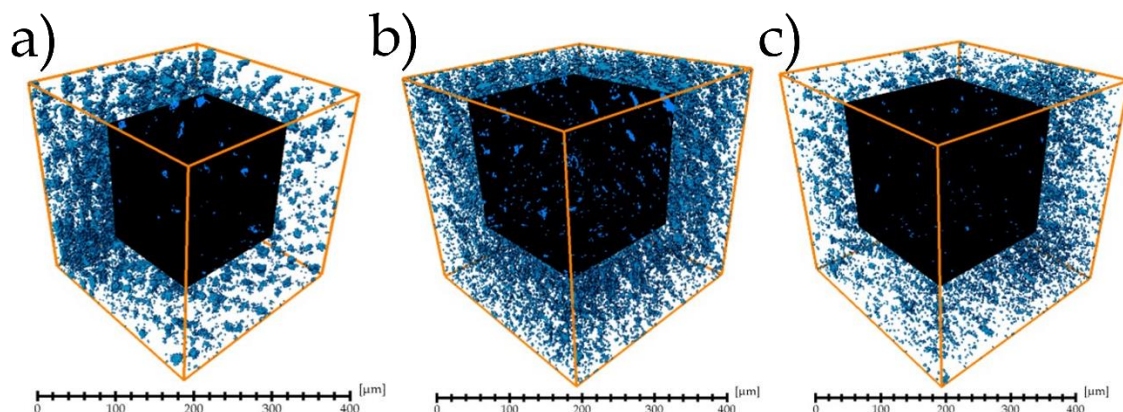


Figure 1: Visualized 3D porosities of a) & b) two pristine LLZO samples and c) of a short-circuited LLZO sample.

Table 1: Summary of the μ CT porosity analysis.

	a) Pristine 1	b) Pristine 2	c) Short-circuit	Unit
Resolution	1.01	0.89	1.12	μm
Voxels	$300 \times 300 \times 300$	$300 \times 300 \times 300$	$300 \times 300 \times 300$	/
Volume	27.8×10^6	19.0×10^6	38.1×10^6	μm^3
Porosity	2.85	2.75	1.06	%

The LLZO samples were synthesized in similar ways than described in Chapter 2²⁻⁴. Two pristine samples and one short-circuited sample were analysed, and their porosities were compared (Figure 1 & Table 1). Preliminary tests hypothesized that the porosity fraction of the pristine samples should be below 5%. The first sample was analysed with a resolution of 1.01 μm and for the data evaluation a representative volume was chosen ($300 \times 300 \times 300$ voxels $\rightarrow 27.8 \times 10^6 \mu\text{m}^3$). This sample revealed a porosity fraction of 2.85%. The second sample was measured with a μ CT resolution of 0.89 μm ($300 \times 300 \times 300$ voxels $\rightarrow 19.0 \times 10^6 \mu\text{m}^3$) and presented a porosity fraction of 2.75%. The third experiment was performed with a sample which had been synthesized and prepared the same way as the two previous ones, but additionally it had been assembled between two Li-foils and cycled until it failed. Subsequently the symmetric cell has been disassembled (removal of the Li-foils on both sides) before it was analysed via μ CT. This short-circuited LLZO pellet was measured with a resolution of 1.12 μm ($300 \times 300 \times 300$ voxels $\rightarrow 38.1 \times 10^6 \mu\text{m}^3$) and unravelled a porosity fraction of 1.06%. Porosities smaller than the resolution, stay undetected, hence the real porosity fraction might slightly deviate from the values we obtained. By comparing the porosities of the pristine samples with the one of the failed sample, we notice that the short-circuited sample shows lower porosity, this could be related to

structural and/or compositional changes which occur as a consequence of cycling. The hypothesis is, that Li-dendrites might nucleate at multiple regions and grow through the electrolyte filling pores and intergranular cavities with Li-rich dendritic structures.

3.2.2. SIMS Analysis

SIMS imaging was performed using a Thermo Fisher Scios DualBeam FIB-SEM equipped with an in-house developed double-focusing magnetic sector SIMS system, as described in Chapter 2⁵. The FIB consists of a gallium liquid metal ion source producing $^{69}\text{Ga}^+$ primary ions. The secondary ions that were collected and imaged are: $^7\text{Li}^+$, $^{139}\text{La}^+$, and $^{155}\text{LaO}^+$. The SIMS measurements were carried out with a primary ion beam energy of 30 keV, a beam current of 0.5 nA, and dwell time of 0.5 ms per pixel. The images were recorded with a resolution of 512×512 pixels and fields of view between 40×40 and 50×50 μm . To extract positive secondary ions, the sample was biased to +500 V, which resulted in a primary ion impact energy of 29.5 keV. Data analysis was performed using the free software ImageJ⁶.

The same short-circuited sample as the one analysed by μCT was analysed via SIMS. In order to study the bulk via SIMS, the pellet was physically cracked to expose inner structures to the surface (as described under "Sample Preparation" in Chapter 2).

3.2.3. Results & Discussion

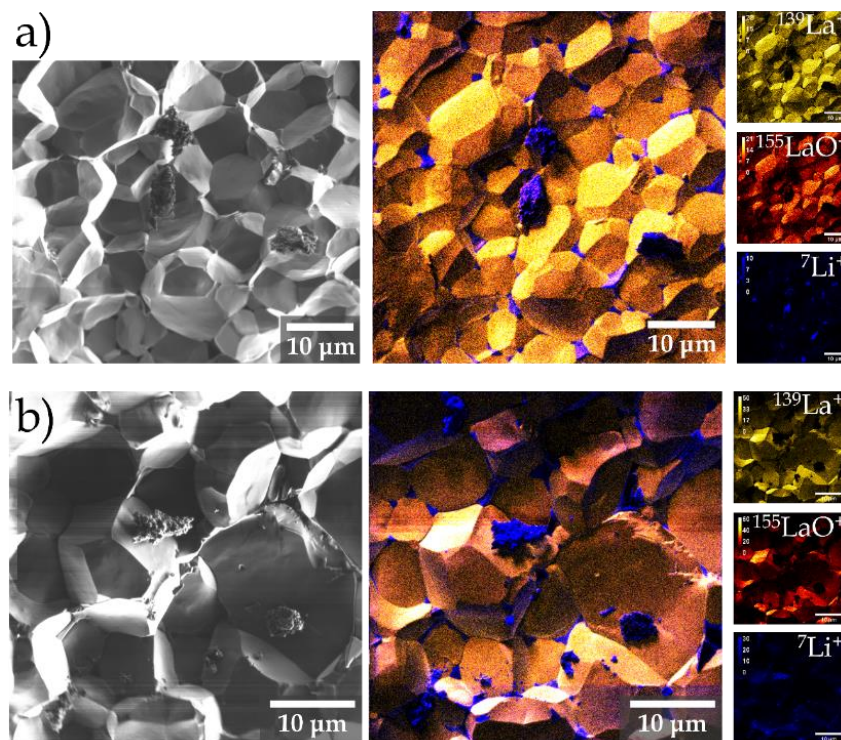


Figure 2: Correlative SE and SIMS chemical imaging of short circuited LLZO samples. In a) SE image, merged chemical image and the individual images of $^7\text{Li}^+$ (blue), $^{139}\text{La}^+$ (yellow) and $^{155}\text{LaO}^+$ (red) with a FOV of 51.8 μm . b) shows a further region of the same sample with a FOV of 41.4 μm .

Indeed, we expect to see similar Li-depositions in the short-circuited sample as the one we were able to observe in the former chapter. Consequently, we performed SEM/SIMS analysis to see if pores and cavities contain Li-accumulations after cycling. Figure 2 shows two correlative SE images and merged SIMS chemical maps of ${}^7\text{Li}^+$ (blue), ${}^{139}\text{La}^+$ (red) and ${}^{155}\text{LaO}^+$ (yellow), and the three individual channels. As expected, Li seems to accumulate at grain-boundaries and into pores.

From this experiment we can draw the following conclusions:

- Reproducibility of the observed dendrite formations in Chapter 2 where the sample was cycled inside the FIB-SEM-SIMS instrument and in this chapter the sample was cycled with similar conditions in a Swagelok cell.
- The density measurements of pristine LLZO samples revealed a porosity of $\sim 2.8\%$.
- The volume occupied by the dendrites is $\sim 55\%$ of the initial porosity fraction. This gives us a rough estimation of the extent of dendrite formation in dense ($>95\%$) LLZO based batteries.

In the following subchapter, we will use a modified version of μCT , namely nanoCT which is basically the same technique, but instead to be a standalone instrument, a FIB/SEM has been modified in order to perform CT analysis within the microscope and with nanometer-scale resolution.

3.3. NanoCT for Cathode Material

Nano-computed tomography (nanoCT), similar to μCT , is a non-destructive technique used for three-dimensional structural imaging of materials. While SIMS can be used either as a standalone instrument or as an add-on module to a FIB instrument, CT is typically a standalone instrument. However, recent studies by Lutter et al.⁷⁻⁹ demonstrated the integration of a compact nanoCT module within a modified SEM instrument. The integration of both nanoCT and SIMS modules within a conventional lab-scale FIB-SEM instrument would greatly enhance its capabilities in terms of sample preparation and materials characterization.¹⁰⁻¹⁵ With the goal to combine both complementary techniques an ex-situ proof-of-concept nanoCT-SEM-SIMS workflow has been developed.

3.3.1 Sample preparation

The sample used in this study is a cathode material obtained from a commercial lithium-ion battery (LIB) cell manufactured by Kokam (product ID: SLPB 353452)¹⁶.

The battery is in the form of a pouch cell, weighing approximately 12 g and having a capacity of around 580 mAh. The cathode material is a blend consisting of two active materials (AMs), namely LiCoO_2 (LCO) and LiNiCoAlO_2 (NCA), along with a carbon black binder phase. The binder component is composed of polyvinylidene fluoride (PVDF P5130), which is commonly used in the production of composite electrodes due to its favourable chemical stability, and carbon (C) black, which acts as a conductive additive¹⁷.

The combination of nanoCT and SIMS presents a challenge in terms of sample preparation due to the conflicting requirements¹⁸ for sample shape. NanoCT typically requires a rod-like sample holder with the sample positioned at the tip. This setup ensures a substantial distance between the X-ray source and the sample stage, minimizing the risk of collision. The sample needs to be placed horizontally between the X-ray source and the detector (Figure 3a). In SEM-based CT, the X-ray source-sample distance is only a few hundred micrometres (Figure 3b). On the other hand, SIMS works best with a planar sample surface, which ensures a uniform electric field for secondary ion extraction.

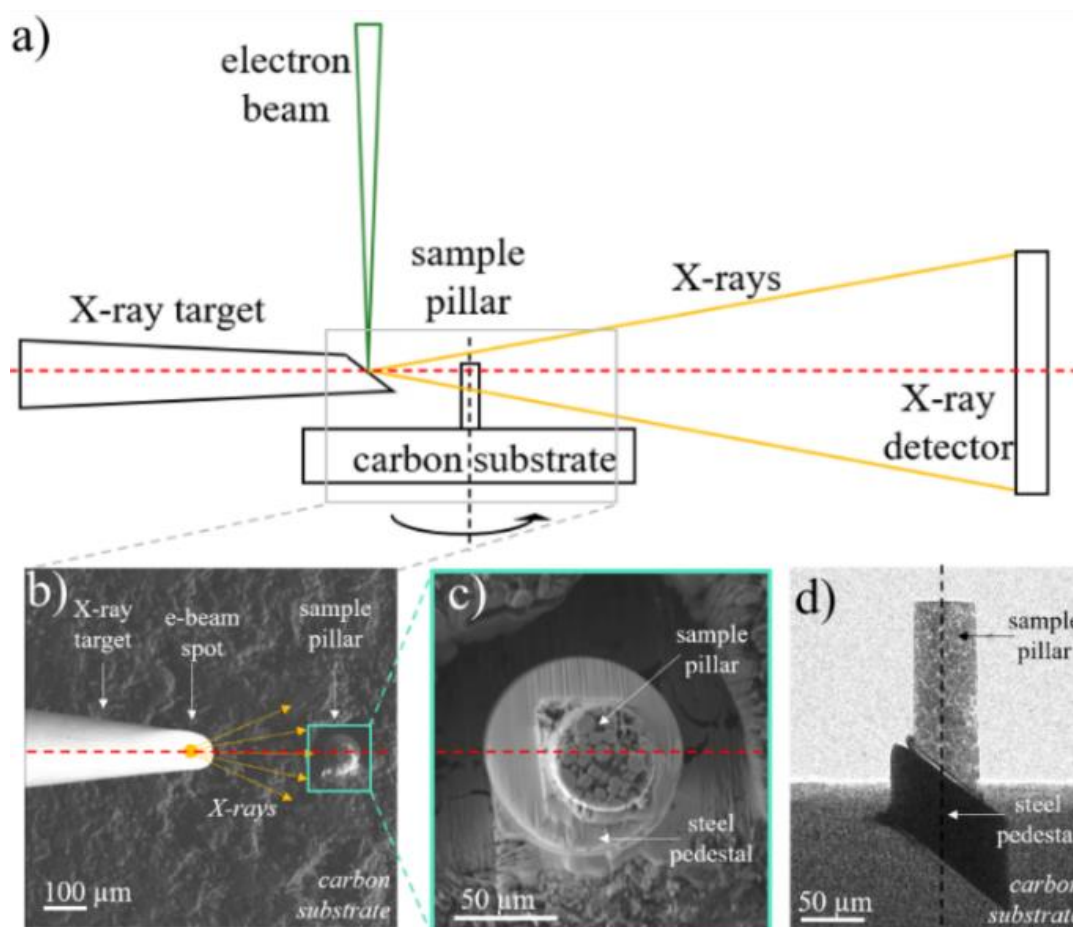


Figure 3: a) Schematic illustration of XRM-II nanoCT setup. b) Top view SEM image showing the X-ray target and the sample pillar. c) Top view SEM image of the sample pillar and the steel pedestal. d) Side view nanoCT slice of the substrate-pedestal-sample arrangement.¹⁹

Considering these contrasting requirements, the decision was made to deviate from a typical nanoCT sample holder rod. Instead, the sample was placed on a planar substrate. Carbon was chosen as the substrate material because it emits low-energy X-rays when exposed to stray electrons. This choice improves the contrast in the CT image.

Upon this substrate, a microscale pillar of the sample material is placed. The height of the pillar needed to be minimized for SIMS while still ensuring that the X-ray target could be positioned directly in front of the sample pillar without touching the carbon surface (Figure 3 a and b). Consequently, the objective was to obtain a pillar height of approximately 150 to 200 μm . To ensure stability, a steel pedestal was positioned on the substrate, and the sample pillar was attached to it using platinum deposition facilitated by FIB (Figure 3 c depicts a top-view SEM image of the sample pillar-pedestal configuration).

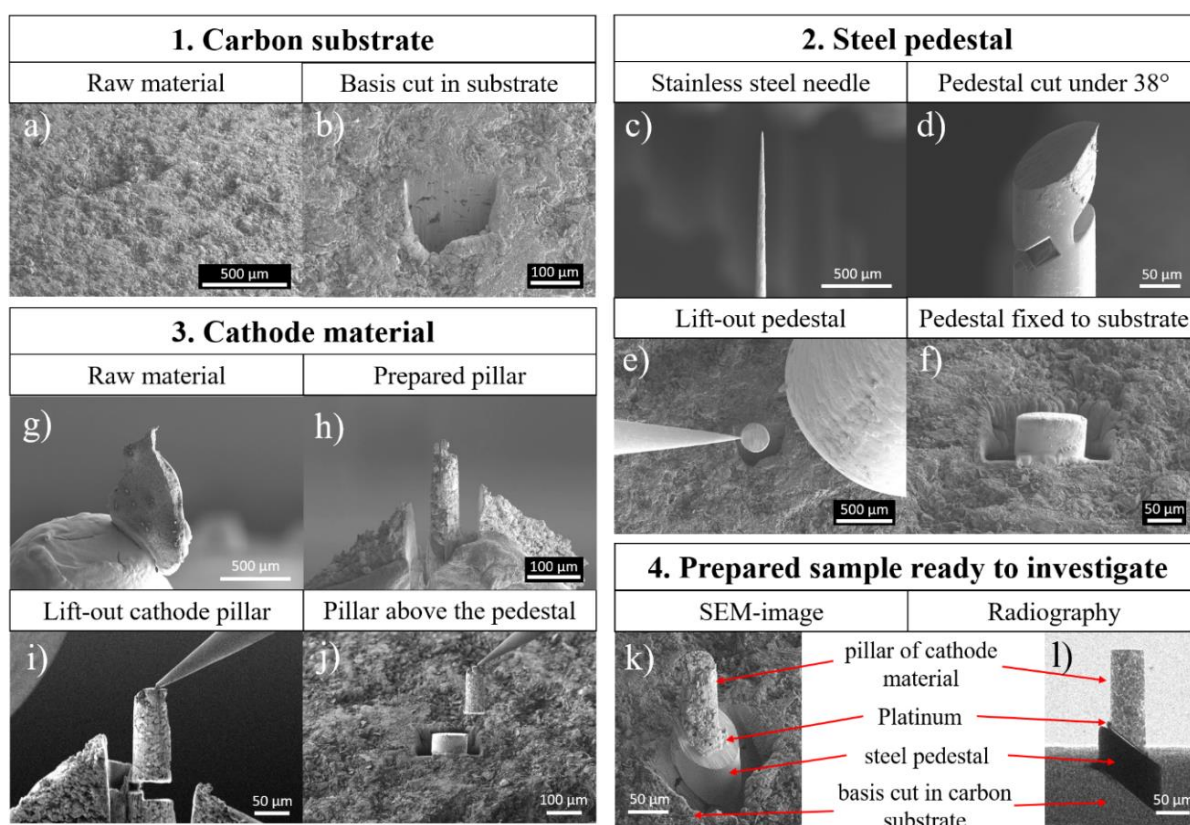


Figure 4: Step 1: a) Carbon substrate. b) Cut a sloped surface, 38°, of ~150 μm width; Step 2: c) Stainless steel needle as received. d) Preparation of pedestal for transfer to carbon substrate. Cuts under 38° angle relative to the needle axis to match the angle of target area on the carbon substrate. Only a small connection to the needle is left until the micromanipulator is attached for transfer. e) Micromanipulator with pedestal hovering above the carbon substrate target area. Gas injection needle (GIS) for platinum precursor coming from the right side. f) Pedestal positioned and fixed to the carbon substrate; Step 3: g) Cathode material glued to a pin. h) Pillar cut from the cathode material ready for lift-out. i) Pillar fixed to the micromanipulator and cut free on the bottom. GIS coming from the left side due to image scan rotation. j) Manipulator with pillar hovering above the pedestal; Step 4: k) SEM image of the final assembly carbon substrate – steel pedestal – cathode material pillar. l) X-ray transmission image of the assembly. Steel pedestal is clearly visible due to atomic number contrast.

Preparation of the sample material including lift-out and transfer to the substrate was carried out in a Xenon (Xe)-Plasma FIB (Thermo Fisher Helios PFIB G4 CXe) equipped with a micromanipulator (Kleindiek MM3A). The advantage of a Xe-Plasma FIB over the widespread Ga-FIB lies in the larger beam current, allowing to keep milling times for large volumes in a useful range. For practical reasons of geometry inside the FIB-SEM it was not possible to cut the pillar perpendicular to its vertical axis and fix it onto the carbon substrate. Instead, cutting was performed under an angle of 38° which is the angle of the ion beam against the stage plane of the instrument used in this study. The preparation consists of three steps (see Figure 4):

1. Cut a plane of $\sim 150 \times 150 \mu\text{m}^2$ under an angle of 38° into the surface of the carbon substrate (Figure 3 a & b).
2. For stability reasons and to make the pillar stand out of the surface, a pedestal was cut from a thin needle of stainless steel with $\sim 100 \mu\text{m}$ diameter. The needle was placed upright on a holder without pre-tilt and no stage tilt was used for the cutting so the angle of the cut face on both ends was again 38° (Figure 3 c & d). This piece was transferred to the previously cut angled area of the substrate using the micromanipulator and fixed with ion beam induced platinum deposition (Figure 3 e & f). The process was adapted from the well-established FIB lift-out preparation of TEM samples.
3. A pillar with a diameter of $50 \mu\text{m}$ was prepared from the sample volume with annular milling using Xe ion beam currents from $2.5 \mu\text{A}$ down to 60nA (Figure 3 g & h). The top edge of the pillar was fixed to the micromanipulator with ion beam induced platinum deposition and cut free from the sample under an angle of 38° , matching the angle of the steel pedestal on the carbon substrate (Figure 3 i). After transfer to the substrate, the pillar was attached to the pedestal using FIB-based deposition and cut free from the manipulator tip (Figure 4 j & k) using ion beam. To increase mechanical stability, further deposition was carried out around the circumference of the pillar.

3.3.2. NanoCT Analysis

The Procon XRM-II nanoCT system utilizes a JEOL JSM-7900F scanning electron microscope (SEM) that is equipped with an X-ray target manipulator and a photon-counting X-ray detector called ADVACAM WidePIX. Alongside electron imaging capabilities, the system incorporates an EDAX EDX detector (Element with APEX software) for chemical analysis of the sample. In the nanoCT mode, a focused electron beam is directed to the tip of an X-ray target, causing the emission of an X-ray

spectrum. This emitted spectrum is then utilized to capture a radiographic image, as depicted in Figure 3.

The energy spectrum of generated X-rays is determined by the choice of target material, and the absorption of X-rays within the sample primarily depends on the atomic numbers of the constituent elements. Consequently, selecting an appropriate target material based on the major elements present in the sample is crucial for achieving optimal image quality. In this study, the chosen cathode material consists of elements such as cobalt (Co) and nickel (Ni), which exhibit high X-ray attenuation coefficients. Therefore, tungsten was selected as the target material. Tungsten has a characteristic $L\alpha$ X-ray energy of 8.4 keV and produces an X-ray spectrum with relatively higher mean energy compared to other target materials like chromium or copper. This characteristic makes tungsten well-suited for imaging materials with high X-ray absorption. Given that the SEM images displayed morphological features on a scale of a few microns, a bulk target was chosen for the experiment.

The geometry of a bulk target is characterized by a tilted surface that has a volume larger than the interaction volume of the incident electrons in the target material. Additionally, the use of a bulk target helps minimizing scatter radiation compared to other target shapes because no electrons pass through the target to reach the stage surface. By using 30 keV electrons and a beam current of 400 nA, the bulk target produces a high photon flux and provides a spatial resolution of approximately 250 nm, which is sufficient to capture the morphology of the cathode sample. Spatial resolution in X-ray CT is influenced by a variety of factors like hardware components (source, detector, stage ...), acquisition parameter and mathematical volume reconstruction. Since 3D spatial resolution can only be determined with suitable test objects, which are not available for nano-CT, the spatial resolution is estimated to about 250 nm. To take advantage of the entire detector width, the images of the nano-CT scan were acquired with a sampling rate of 50 nm. As a consequence, the Nyquist criterion (2,3 pixels are needed to resolve a feature: $2,3 \times 50 \text{ nm} = 115 \text{ nm}$ resolution) will not limit the spatial resolution.

To conduct the CT measurement, it was necessary to align the X-ray focal spot, with the sample and the centre of the X-ray detector on a horizontal plane (Figure 3). Consequently, the target was positioned directly above the carbon disk at a height of approximately 100 μm . This arrangement allowed for sample rotation without any



Figure 5: QR-code showing a video of the by nanoCT reconstructed volume.

contact between the sample and the target. The sample pillar was placed at a distance of 400 μm from the focused electron beam spot on the target.

During imaging, the emitted X-rays travelled through the sample, undergoing attenuation, and ultimately reached the X-ray detector. To obtain the 3-dimensional information, the sample, in the form of a microscale pillar, was incrementally rotated in small angular steps of 0.3° around its main axis^{20,7}. A radiograph was captured for each rotation angle. In total, 1,200 projections were acquired, with an exposure time of 90 s for each projection.

Following the data acquisition, the projections were utilized to reconstruct a 3D volume of the object using a regularized simultaneous algebraic reconstruction technique (ImageJ⁶ & AVIZO version 2021.1., Thermo Fisher). Specific geometry correction for the XRM-II nanoCT setup was applied during the reconstruction process, revealing the microstructure of the cathode material.²¹

Figure 6 showcases examples of reconstructed slices obtained from the nanoCT measurement, alongside SEM images. Additionally, a video of the reconstructed volume is available through scanning the QR code shown in Figure 5.

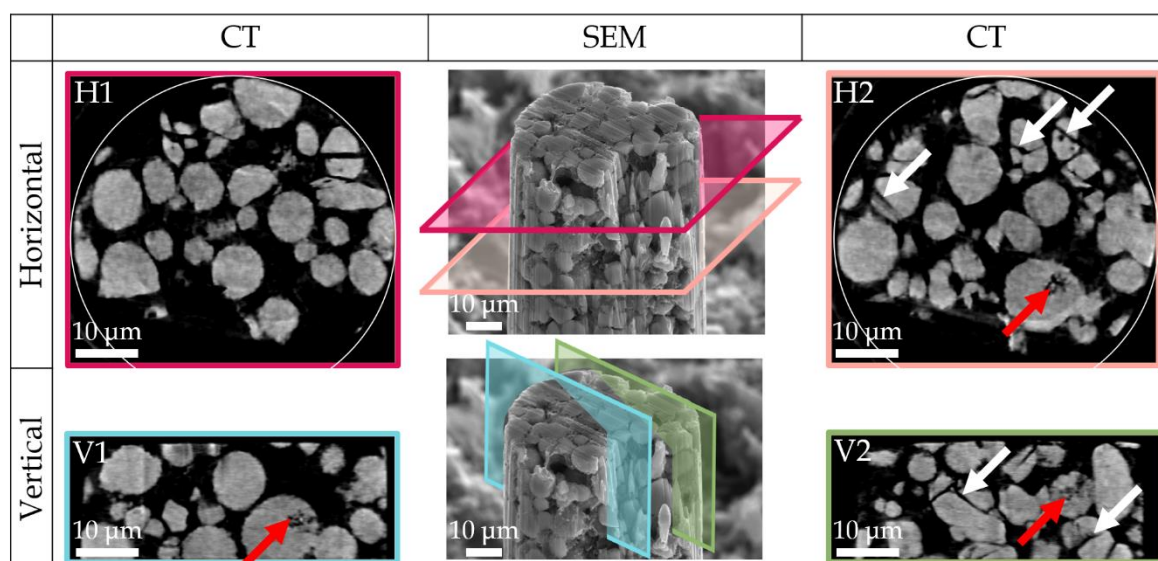


Figure 6: Example of reconstructed slices from nanoCT measurement of the cathode sample. The left and right columns depict two horizontal (H1, H2) and two vertical (V1, V2) slices of the reconstructed volume from nanoCT. The column in the middle shows an SE-SEM image with the approximate positions of H1, H2 planes, and the same image is reproduced below it to indicate the V1 and V2 planes. Possible degradation products are visually inspected and are highlighted in H2, V1 and V2: red arrows = micropores; white arrows = cracks.¹⁹

3.3.3. SIMS Analysis

SIMS imaging was performed using a Thermo Fisher Scios DualBeam FIB-SEM equipped with an in-house developed double-focusing magnetic sector SIMS system

which allows the detection of multiple masses in parallel ^{5,22}. The FIB consists of a gallium liquid metal ion source producing $^{69}\text{Ga}^+$ primary ions. The secondary ions that were collected and imaged are: $^7\text{Li}^+$, $^{27}\text{Al}^+$, $^{58}\text{Ni}^+$, and $^{59}\text{Co}^+$. The SIMS measurements were carried out with the primary ions of 30 keV, a current of 50 pA, and dwell times between 0.55 and 1.20 ms. The images were recorded with a resolution of 512×512 pixels and FOVs between 10 and $45 \mu\text{m}$. To extract positive secondary ions, the sample stage was biased to +500 V which resulted in a primary ion impact energy of 29.5 keV. Data analysis was performed using the free software ImageJ ⁶ and AVIZO (Version 2021.1., Thermo Fisher).

An exemplary correlative SEM-SIMS analysis is shown in Figure 7 with SIMS chemical maps of the raw cathode sample (before milling to pillar shape). $^7\text{Li}^+$ (green), $^{27}\text{Al}^+$ (blue), $^{58}\text{Ni}^+$ (yellow), $^{59}\text{Co}^+$ (red). The image on the top right represents an SEM secondary electron image of the same ROI and the image on the bottom right is an overlap of the four individual elemental maps. It is recognisable, that while Li and Co are present within all the particles, Al and Ni are only detected in some specific active material (AM) particles. This is perfectly aligned with our expectations as both AMs LCO and NMC both contain Li and Co, however only NCA is partly composed of Al and Ni.

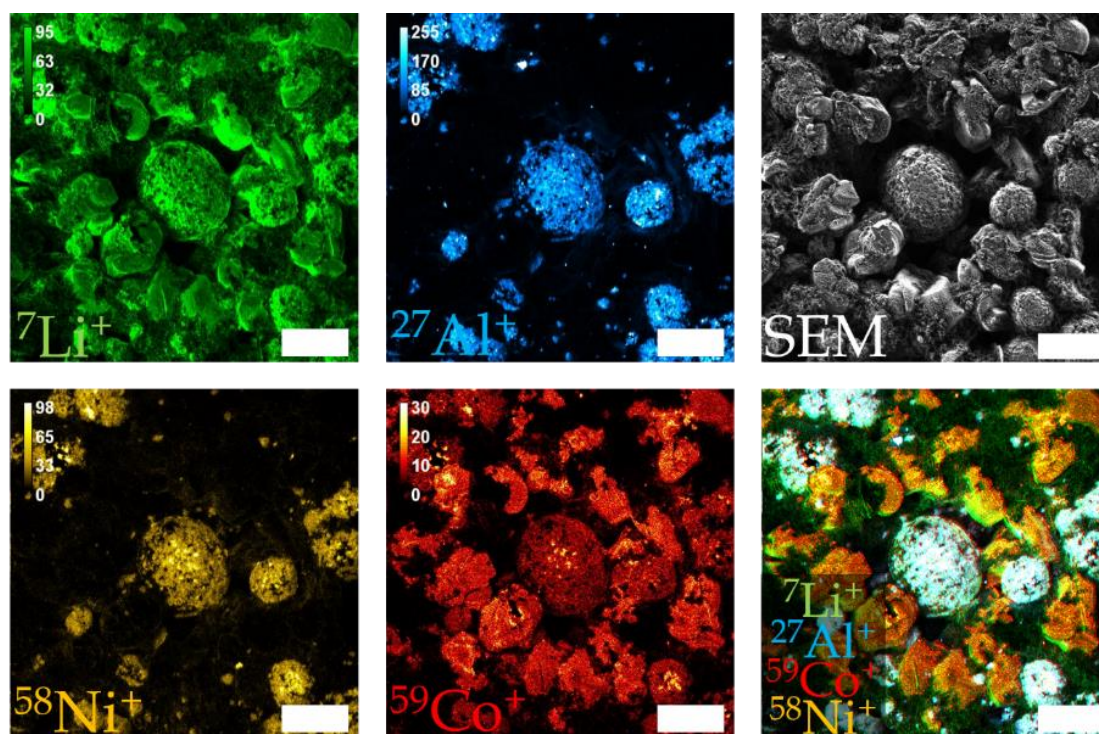


Figure 7: SIMS chemical maps of the raw cathode sample (prior to milling to pillar shape). $^7\text{Li}^+$ = green, $^{27}\text{Al}^+$ = blue, $^{58}\text{Ni}^+$ = yellow & $^{59}\text{Co}^+$ = red. The image on the top right represents an SEM secondary electron image of the same ROI and the image on the bottom right is an overlap of the four individual elemental maps. (scale bar = $10 \mu\text{m}$)

3.3.4. Results & Discussion

In the subsequent analysis, we present a selection of reconstructed slices obtained from the nanoCT measurements (Figure 6). Additionally, a video displaying the complete reconstructed volume is available through the QR code shown in Figure 5. It is important to emphasize that in ex-situ workflows, locating the exact same ROI after transferring samples between instruments can be extremely challenging and, in some cases, not feasible. The afore-mentioned sample preparation protocol allows to perform correlative nanoCT and SIMS on the exact same unmodified (neither structurally nor chemically) ROI. This unique capability allows for the examination of the precise sample volume using nanoCT, which provides a comprehensive two- and three-dimensional overview of the sample volume with a moderate resolution. Moreover, it facilitates the identification of internal features such as damaged particles or particle-internal pores that can subsequently be probed locally using SIMS for chemical analysis. This ensures that the analysis is conducted on the exact same sample volume, providing valuable insights into the inner structure of the sample. The spatial resolution of the nanoCT is determined in the reconstructed slices by calculating the full-width at half-maximum of the line spread function resulting from the differentiation of the edge-response function between sample volume and background (vacuum) resulting in $224 \text{ nm} \pm 23 \text{ nm}$ ²³. The evaluated area is an object edge of the sample pillar, which is prepared by FIB, showing a surface roughness smaller than the expected spatial resolution.

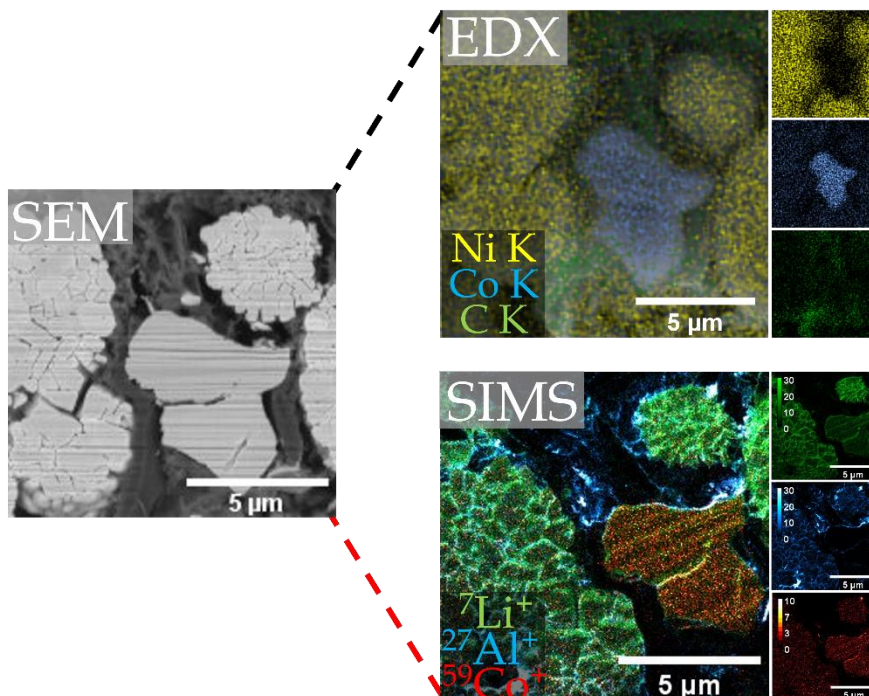


Figure 8: Correlative SEM, EDX and SIMS images of the same ROI. The EDX elemental maps of Ni (yellow), Co (blue) and C (green) elucidate the identity of the particles. The correlative SIMS images showing the chemical distributions of ${}^7\text{Li}^+$ (green), ${}^{27}\text{Al}^+$ (blue) and ${}^{59}\text{Co}^+$ (red) reveal further details due to its capability of detecting Li and nm-scaled lateral resolution. (scale bar = 5 μm)

The reconstructed volume is highlighted in Figure 6, showing two horizontal (H1, H2) and two vertical (V1, V2) reconstructed slices. In H2 and V2, we draw attention to the identification of potential ROIs, particularly anomalous microstructural features, by means of visual inspection. These features, along with possible degradation products, are carefully examined, and specific areas for subsequent SIMS imaging are selected. Within H2 and V2, particle internal micro-pores are indicated by red arrows, while cracks are pointed out by the white arrow.

For a more detailed morphological analysis, a higher lateral resolution is necessary. To achieve this, regular SE imaging in an SEM is employed. This technique not only reveals nm-scaled features but also allows imaging of the carbon-based binder material, which cannot be detected by nanoCT with the selected target.

A definitive distinction between LCO and NCA cannot be made based on common nanoCT or SE images (Figure 6, Figure 9 a & b, g & h). For that reason, EDX elemental maps of Ni, Co and C have been performed in addition to XRM-II nanoCT to elucidate the identity of the particles. Figure 8 shows a correlative SEM, EDX and SIMS images of the same ROI. The EDX elemental maps of Ni (yellow), Co (blue) and C (green) elucidate the identity of the particles, as only NCA contains Ni. Ultimately, the major limitation of EDX is that it is not surface sensitive, and that the analysis of Li is still not feasible for common EDX systems. Hence, correlative SIMS images show the chemical distributions of ${}^7\text{Li}^+$ (green), ${}^{27}\text{Al}^+$ (blue) and ${}^{59}\text{Co}^+$ (red) revealing further details due to its nm-scaled lateral resolution and its capability of detecting low-Z elements such as Li.

Figure 9 a–f presents the correlative nanoCT, SE-SEM, and SIMS images of an intact NCA particle. The nanoCT image (Figure 9 a) lacks detailed features, making it challenging to differentiate from LCO. In contrast, the SE image (Figure 9 b) displays the particle's intricate morphology, characterized by numerous nm-scaled primary grains that aggregate into larger secondary particles in the μm -range. Additionally, SEM reveals the presence and distribution of the binder material, which remains invisible in the nanoCT image.

The SIMS image (Figure 9 c) shows an overlap of the individual chemical maps (Figure 9 d–f) of ${}^7\text{Li}^+$ (green), ${}^{27}\text{Al}^+$ (blue), and ${}^{59}\text{Co}^+$ (red). The ${}^7\text{Li}^+$ signal is detected throughout the NCA particles, while the carbon-binder shows no presence of Li. An unexpected high amount of Al is detected not only in the grain boundaries of the NCA primary grains but also appears to have diffused into the binder phase.

The example presented in Figure 9 g–l reinforces the earlier statement that a definitive differentiation of the AM is not achievable based on nanoCT data alone (Figure 9 g). However, the SE image (Figure 9 f) allows for the identification due to morphological distinctions between NCA and LCO. The SIMS data demonstrates that Li is

exclusively detected in the AM (Figure 9 i, j), while its concentration in the binder material falls below the SIMS detection limit.

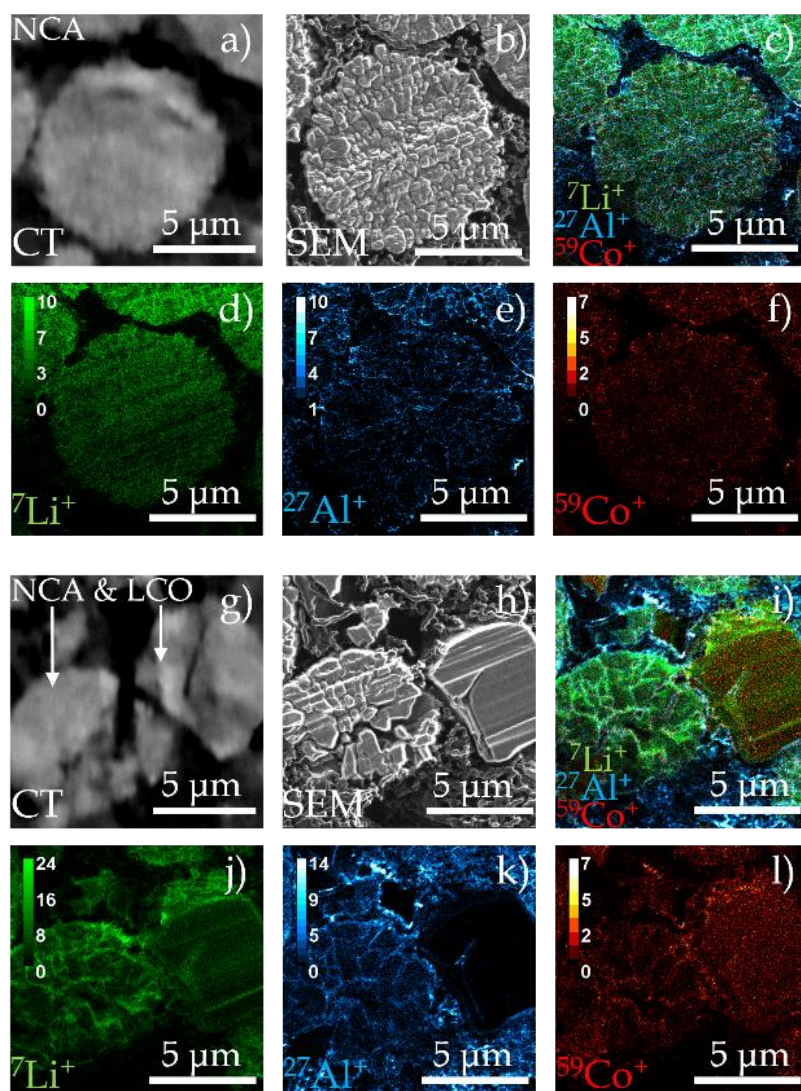


Figure 9: Correlative CT, SEM and SIMS images of an intact NCA particle (a-f). The 1st row shows in a) a reconstructed slice from nanoCT, b) an SE image and c) the overlay of three SIMS channels, whereas the 2nd row depicts the chemical images of the single SIMS channels (d-f). The correlative analysis of adjacent damaged NCA and LCO is shown in g-l. The AM particles presenting cracks have been exposed to the surface by local FIB-milling. Both, the intact NCA particle in a) and the adjacent damaged NCA and LCO in b) have been analysed at an approximate depth of 1.5 μm from the top of the sample pillar. The SIMS elemental mappings represent ${}^7\text{Li}^+$ (green), ${}^{27}\text{Al}^+$ (blue) and ${}^{59}\text{Co}^+$ (red). The intensity bars in the individual SIMS images represent the detected secondary ions per pixel for a certain current and dwell time. (scale bar = 5 μm)¹⁹

Regarding the distribution of Al (Figure 9 k), this specific example further supports the previous observation that Al tends to accumulate in internal grain-boundaries of NCA and diffuses into the binder phase. Notably, no Al was detected on the LCO particle, which aligns perfectly with our expectations, given that the particle's chemical composition is Al-free.

Previous Figure 7 showing SIMS elemental maps of the raw sample material (underwent no sample preparation) elucidates only very few Al within the binder phase, hence we cannot completely rule out, that the Al (re)distribution is a consequence of sample preparation or different factors like aging.

3.3.5. Conclusion

To sum up, first, nanoCT in a FIB-SEM was used to get a complete 2- and 3D representation of the sample to reveal its morphology and to image defects of the microstructure. The big advantage of nanoCT is that relatively large volumes (multiple μm^3) can be reconstructed and its non-destructive nature, has the benefit that the sample can be scanned to identify ROIs (e.g. damaged AMs) for further investigations without being altered. Subsequently, *in-situ* EDX and *ex-situ* SEM/SIMS was performed revealing chemical distributions and sub-micron nanostructures (e.g. NCA primary grains).

The complementary nature of nanoCT and SIMS makes a correlative approach highly appealing. This study demonstrates the feasibility and compatibility of conducting a correlative nanoCT-SIMS analysis using FIB-SEM instruments. The successful demonstration of this *ex-situ* approach not only proves its feasibility but also highlights the considerable advantages of integrating both techniques into a single FIB-SEM instrument.

For example, our innovative correlative analysis method offers an unprecedented opportunity to investigate Li-rich dendritic structures in battery materials. Such structures can form during cycling processes (as discussed in Chapters 2 and 4) and pose significant safety risks (e.g., short circuits) while also adversely affecting electrochemical performance by inactivating Li. By correlating the morphology (via nanoCT/SEM) with chemical composition through SIMS imaging, we can potentially uncover the mechanisms behind dendrite formation and propagation (as explored by ²⁴⁻²⁷). This integrated approach holds great promise in advancing our understanding of these crucial processes in battery materials.

There are several options available to accelerate both sample preparation and the analysis workflow. Firstly, opting for a plasma or laser FIB instead of a conventional FIB would significantly reduce the sample preparation time. Secondly, there are various methods to accelerate the analysis workflow, but many of them involve a trade-off in resolution. For instance, in nanoCT measurements, the process could be accelerated by reducing the number of projections, increasing the rotation angle between measurements, and/or reducing the exposure time. Similarly, for SIMS analysis, speeding up the process could be achieved by increasing the primary ion current, reducing the dwell time, and/or decreasing the number of pixels.

However, it is crucial to note that altering these analysis parameters has an impact on the resolution. Therefore, finding a balance between accelerating the process and maintaining a resolution that is adequate for the analysis purpose is essential within a reasonable time frame.

From this subchapter we can draw the following conclusions:

- Introduction of a methodology that combines FIB-SEM, X-ray nanoCT, and SIMS techniques for a comprehensive analysis of battery materials (e.g. cathodic AM). This integration allows for precise sample characterization, high resolution imaging, three-dimensional reconstructions, and chemical composition analysis.
- The results elucidate that Al, initially only present in the NCA phase, tends to accumulate in internal grain-boundaries of primary NCA particles and diffuses into the binder phase. No Al at all is detected in the LCO phase.
- To sum up, we have successfully shown that sophisticated correlative analysis, involving the combination of nanoCT-SIMS, can be carried out on readily available FIB-SEM instruments, eliminating the need for specialized standalone equipment. This broadens the scope of research possibilities, allowing us to address longstanding questions that demand correlative analysis encompassing both structural and chemical investigations from the μm to nm scales.

3.4. EDX & WDXS for composite LLZO-Cathode

In the previous subchapters, we used X-ray based techniques to study the porosity of solid electrolyte via μCT and correlative nanoCT was used to analyse cathode material structurally as well as chemically¹⁹. This subchapter focusses on the 3D cathode/solid electrolyte interface, which represents the region between cathode and SE where both components gradually merge. This 3D structure is important, because it may increase the effective contact surface between cathode and SE by orders of magnitude and by that enhances the charge transfer rate when stripping and plating. Consequently, the cyclability and lifetime of the battery are increased.^{28,29,27}

By analysing an LCO/LLZO heterointerface at different stages (uncycled, cycled, & recovered), we aimed to study the electrochemical degradation as well as the thermal recovery quantitatively and qualitatively.

The presented workflow shows an unprecedented correlative analysis of the complex 3D LCO/LLZO heterointerface. The chapter ends with a case study focussing on the

degradation and recovery of the LCO/LLZO interface and proposes a comprehensive mechanism.

3.4.1. Sample Preparation

This sample has been synthesized by another method than the previous ones (μ CT & nanoCT). Details on the synthesis of the LLZO:Al,Ta ($\text{Li}_{6.45}\text{Al}_{0.05}\text{La}_3\text{Zr}_{1.6}\text{Ta}_{0.4}\text{O}_{12}$) solid electrolyte and preparation of the LCO-LLZO:Al,Ta mixture can be found elsewhere³⁰⁻³⁵.

The samples for this analysis were polished with SiC sandpaper up to #4000 followed by water free diamond suspension (3 μm).

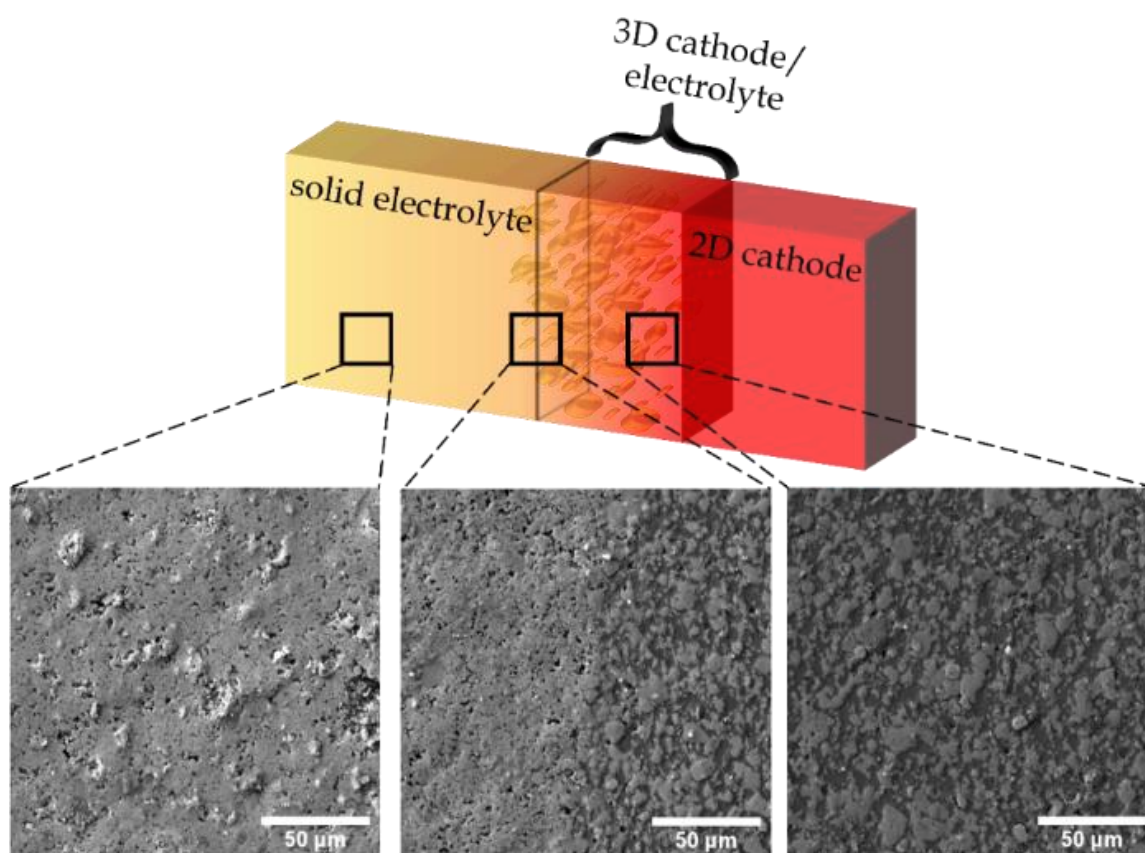


Figure 10: Schematics of of the $\text{LiCoO}_2/\text{Li}_7\text{La}_3\text{Zr}_2\text{O}_{12}:\text{Al},\text{Ta}$ sample and its heterointerface with corresponding SEM images of a) LLZO:Al,Ta b) the interface of SE and the 3D cathode/electrolyte structure, and c) of the 3D cathode/electrolyte.

Figure 10 shows a schematic of the $\text{LiCoO}_2/\text{Li}_7\text{La}_3\text{Zr}_2\text{O}_{12}:\text{Al},\text{Ta}$ sample and its heterointerface with corresponding SEM images of a) LLZO:Al,Ta b) the interface of pure LLZO and the 3D LLZO/LCO phase, and c) of the 3D cathode/electrolyte.

Subsequently, non-destructive chemical characterization analysis via EDX & WDXS were performed to study the heterointerface and its degradation mechanism.

3.4.2. EDX Analysis

EDX analyses was performed with a 50 mm² Xmax spectrometer (Oxford Instruments, Abington, UK), connected to a Helios Nanolab SEM 650 microscope (FEI, Eindhoven, The Netherlands).

3.4.3. WDXS Analysis

WDXS measurements have been performed on a Hitachi SU-70 equipped with a wavelengths dispersive X-ray detector system named “Wave Spectrometer” (Oxford Instruments, Abington, UK) supplied with the following analytical crystals Lithium Fluoride (LiF), Pentaerythritol (PET), Thallium acid phthalate (TAP), layered synthetic microstructure (LSM80N) and LSM200 for calibration. The accelerating voltage for the electron beam was 20 kV, the beam current 8.42 nA, and the peak dwell time was set to 60 s. The elements which were analysed are Ta, Co, La, Zr, Al, and O (standards measurements were performed with Ta→Ta L_α, Co→Co K_α, La→LaB₆ L_α, Zr→Zr L_α, Al→Al₂O₃ K_α, O→Al₂O₃ K_α all with 20 keV electron beam).

3.4.4. SIMS Analysis

SIMS images are recorded with an accelerating energy of the primary ions of 30 keV and currents between 0.3-0.5 nA. The sample stage is biased to a potential of +500 V, resulting in a primary ion impact energy of 29.5 keV. The measurements are performed in positive mode and the detected masses are ²⁷Al⁺, ⁵⁹Co⁺ and ¹³⁹La⁺. The image resolution is 512×512 pixels and the dwell times per pixel are between 750 and 1000 μs. Data analysis was performed using the free software Fiji (ImageJ)⁶.

3.4.5. Results & Discussion

Table 2: Summary of the EDX and WDXS results on different locations. Column named “LLZO” and “LCO” represent measurements on the pure phase, and “LLZO/LCO” was data recorded on the interface of LLZO particles embedded in the LCO phase. All values are indicated in atomic-%. LLZO 1 & LLZO 2 represent two different measurements on different areas of the sample but within the same phase, the same is true for LCO 1 & LCO 2.

	EDX					WDXS		
	LLZO 1	LLZO 2	LLZO/ LCO	LCO 1	LCO 2	LLZO	LLZO/ LCO	LCO
La	21.1	29.8	11.5	1.5	13.2	28.4	30.2	0.6
Zr	11.5	10.7	5.6	0.1	4.8	11.4	11.0	0.0
O	61.6	52.9	67.6	45.9	33.2	57.3	54.1	52.2
Al	2.9	3.1	1.7	1.1	1.0	0.1	0.4	0.2
Ta	2.6	3.2	1.4	0.2	1.4	2.4	2.3	0.0
Co	0.3	0.3	12.2	51.2	46.4	0.4	2.0	47.0

Table 2 shows the quantitative results (in atomic-%), which were taken via EDX and WDXS at different locations of the sample. Measurements were performed on the pure LLZO:Al,Ta phase (LLZO 1 & LLZO 2), on the pure LCO (LCO 1 & LCO 2), and on

the interface of LLZO-particles embedded in the 3D LCO (LLZO/LCO) matrix. While via EDX we detect reasonable proportions regarding the atomic-% within the LLZO phase (LLZO 1 & 2), it is also noticeable that within the LCO phase (LCO 1 & LCO 2), the interpretation of the quantitative analysis is not straight forward. LCO 1 elucidates very low values for all the elements present in LLZO and high O and Co atomic-%, which seems to be plausible, considering a rather large interaction volume. However, LCO 2 shows considerably high atomic-% especially of La, Zr and Ta compared to LCO 1. This could be due to the fact, that EDX is not very surface sensitive with an interaction depth of the electrons in the μm -range, hence generating X-rays from subsurface regions which possibly could include the LLZO phase.

Figure 11 shows a chemical map obtained by EDX with Al (red), Co (blue) and La (green). The chemical map shows the interface between pure LLZO and the LCO/LLZO phase. EDX can be useful for analysing and mapping abundant elements, however for trace or dopant-level elements, the technique is not very performant. While EDX is in many cases a very powerful technique, the large interaction volume as well as the low sensitivity of the technique makes it in this case not accurate enough. The EDX values in Table 2 give quantitative approximations, however for a detailed study on dopants a higher detection limit is needed. It is clearly noticeable, that the atomic-% detected for the dopants (Al and Ta) are clearly above the expected concentration. EDX has a typical detection limit of ~ 0.1 at.-%, while WDXS has a detection limit of ~ 0.005 at.-% (= 50 ppm). WDXS measurements provided more precise atomic-% of all elements of the pure LLZO and the pure LCO phase.

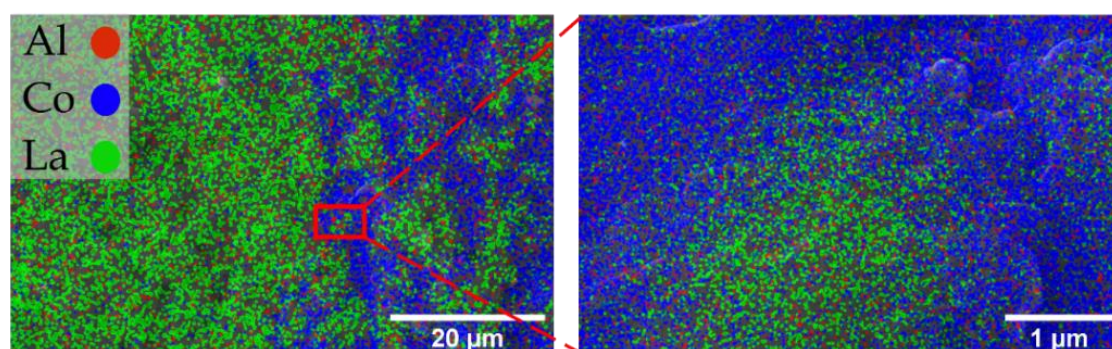


Figure 11: Chemical mapping performed via EDX. (La = green; Co = blue; Al = red)

Based on the WDXS data (Table 2), we can conclude that the trends of the quantitative analysis seem to be correct with high La, Zr, O, (dopant level: Ta) at.-% for the LLZO phase and, on the other hand, high Co and O concentration (i.e. low La, Zr, Ta at.-%) for the LCO phase. Only Al does not really fit into the trend and seems to be two times more concentrated in LCO (0.2 at.-%) than in LLZO (0.1 at.-%), and even more

abundant in the LLZO/LCO interface region (0.4 at.-%). This observation is a subtle indication that Al could potentially diffuse out of LLZO towards the LCO/LLZO interface maybe into LCO. However, those quantitative values are per se not enough convincing to make strong statements or interpretations, hence SIMS analysis will be required to study in detail whether Al diffusion occurs.

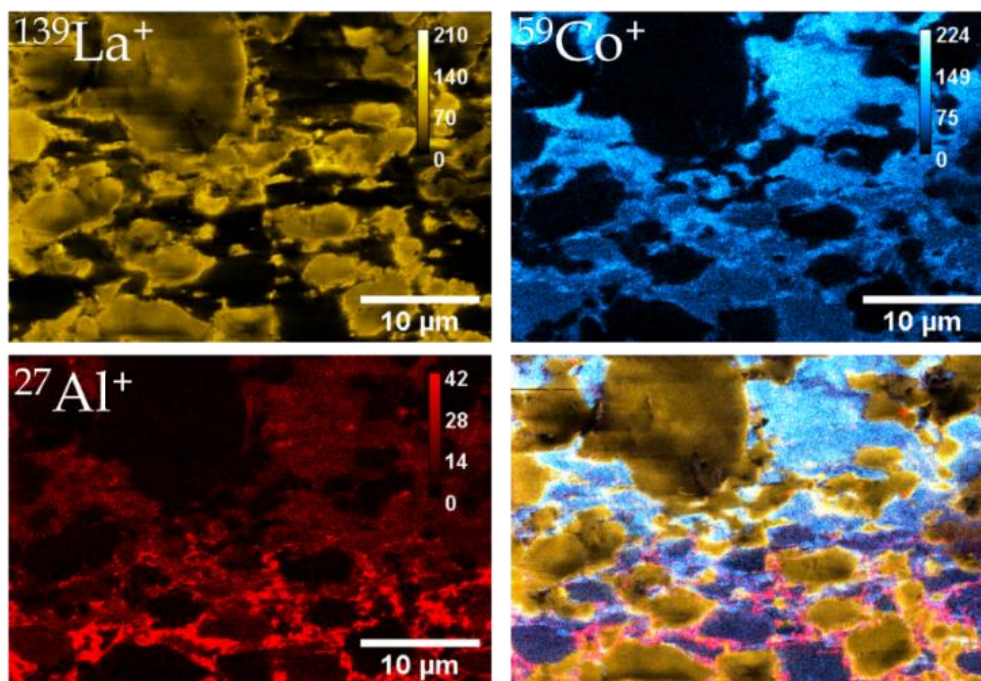


Figure 12: SIMS chemical maps on a FOV of 38 μm with $^{139}\text{La}^+$ in yellow, $^{59}\text{Co}^+$ in blue, $^{27}\text{Al}^+$ in red and an overlap of the three channels.

Figure 12 shows preliminary results taken via SIMS chemical imaging of $^{27}\text{Al}^+$ (red), $^{59}\text{Co}^+$ (blue) and $^{139}\text{La}^+$ (yellow) respectively. The FOV is 38 μm which is rather large, and we can see a multitude of LLZO grains (yellow) embedded in the LCO phase (blue). The Al distribution however seems to support former hypothesis about Al diffusion, based on the WDXS data.

As the FOVs of the chemical maps in Figure 12 are too large for a precise analysis, the experimental parameters were tuned to recorded chemical maps with smaller FOVs. Figure 13 shows chemical maps of $^{27}\text{Al}^+$ (red), $^{59}\text{Co}^+$ (blue) and $^{139}\text{La}^+$ (yellow) respectively, with a FOV of 8 μm . The fourth image shows the merged image of the three channels. The LLZO and the LCO phase are separated sharply, more interesting however, is the distribution of Al which is barely detectable in the LLZO phase and mainly present in LLZO/LLZO grain boundaries as well as in the LLZO/LCO interface. Up to here, we can conclude that the WDXS measurements provided a very important hint regarding the Al distribution, and that the initial hypothesis of Al accumulation at the LLZO/LCO interface got confirmed by SIMS imaging.

Consequently, the question rises whether the Al diffusion has an influence on the electrochemical performance and if/how the Al redistributes when cycling the

battery. This chapter will be rounded up with a case study, which was complemented with two additional samples which have been synthesized the same way as the sample analysed before in this chapter (with EDX, WDXS, and SIMS), but underwent different processes (cycling, recovering).

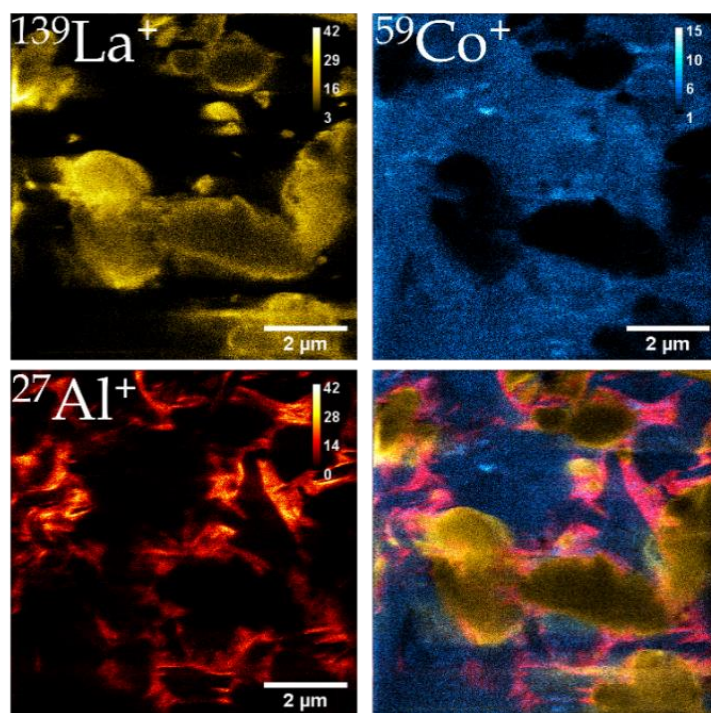


Figure 13: SIMS chemical maps on a FOV of $8\ \mu\text{m}$ with $^{139}\text{La}^+$ in yellow, $^{59}\text{Co}^+$ in blue, $^{27}\text{Al}^+$ in red and an overlap of the three channels. The small FOV allows to precisely map the Al distribution on the LCO/LLZO interfaces. (scale bar = $2\ \mu\text{m}$)

3.4.6. Case Study

The following case study is based on a published work co-authored by me and led by Dr. Martin Ihrig³². The initial WDXS SIMS data provided important hints regarding the Al distribution and redistribution, which could in the following be proven by other microstructural analysis and the understanding was further deepened by simulations. The electrochemical characterisation shown in Figure 14 and the microstructural analysis in Figure 15 have been performed by different authors of this study and are taken with permission from the authors and publisher (reprinted from ³² according to the terms of the CC-BY 4.0 license).

Introduction:

All-solid-state batteries are promising candidates to power the upcoming energy transition. Unfortunately, they still suffer from performance degradation during cycling^{36–40}. In this study it has been identified that amorphization of the LLZO/LCO heterointerface and Al redistribution²⁷ are at the origin of performance degradation⁴¹. The heterointerface has been structurally and chemically analysed and based on the

acquired understanding, this study elucidates a method to recover ~80% of the initial storage capacity through thermal recovery.

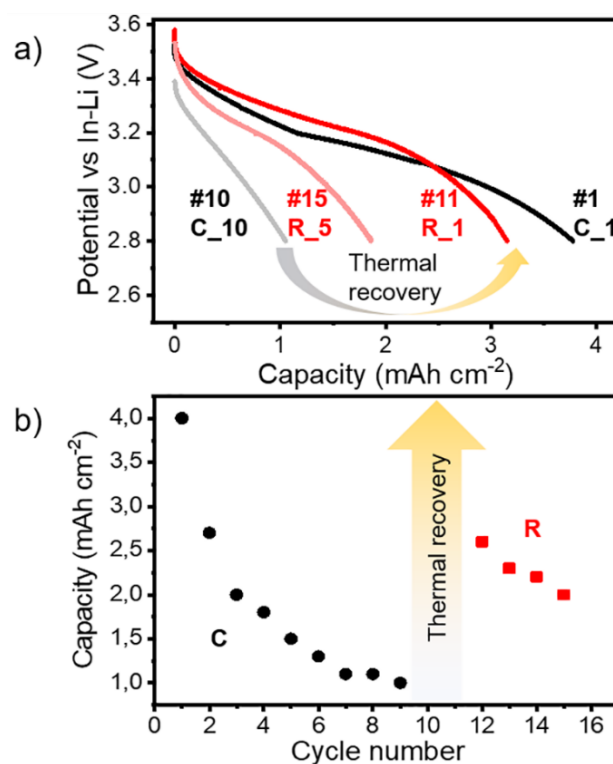


Figure 14: (a) Discharge curves of an ASSB with a composite LCO/LLZO:Al,Ta cathode. The capacity of the ASSB decays rapidly, but thermal recovery (annealing) restores most of the initial capacity. The capacities of each cycle are shown in panel b. (taken from ³²)

Details on the materials synthesis and preparation of the half-cells, the full cell fabrication ³⁰⁻³⁵, the electrochemical characterization as well as the thermal recovery can be found elsewhere³². Experimental detail regarding the microstructural analysis (TEM & SAED), as well as for SIMS analysis can be found in the published work³².

Results:

The first sample is a pristine LLZO/LCO sample (Figure 12 & Figure 13), the second sample has been prepared exactly the same way but underwent 10 cycles (C_x) and the third one was first cycled (10 cycles) and subsequently annealed which acts as recovery (R_x) treatment after cycling. (The “x” indicates the number of cycles.)

Discharge curves reveal that the uncycled cell exhibit good electrochemical activity and a high areal capacity of about 4 mAhcm⁻² in the first cycle (Figure 14 a,b, C₁). Nevertheless, after undergoing multiple cycles, a significant reduction in capacity is observed, resulting in a mere 1 mAhcm⁻² after only 10 cycles (Figure 14 a,b, C₁₀).

The ionic conductivity of LLZO is particularly sensitive to change in the crystal structure, this leads to an increase in interfacial resistance and a capacity reduction.

The primary cause for the deterioration of cell performance during cycling could be amorphization of LLZO:Al,Ta, consequently we hypothesized that the performance could be revived by recrystallizing LLZO:Al,Ta through a similar annealing process employed for crystallizing of the initial synthesis of LLZO:Al,Ta/LCO.

After thermal recovery, the initial discharge exhibited an areal capacity of 3.1 mAh cm⁻², indicating that approximately 80% of the original capacity of the composite LCO-LLZO:Al,Ta cathode could be recovered (Figure 14 a, b, R_1).

To gain a thorough comprehension of the degradation and thermal recovery mechanisms, along with the processes involved during electrochemical cycling and annealing recovery, it is crucial to analyse the composite LCO-LLZO:Al,Ta cathode and its interface after each treatment stage. Consequently, microstructural analysis via TEM, SAED and SIMS is performed to obtain a deeper understanding of the thermal recovery and its underlying mechanism. The exact locations of the TEM and SAED analysis (Figure 15) can be seen in Figure 18 in the annexe 2.

TEM and TEM-SAED, reveals that the uncycled state had sharp LCO/LLZO:Al,Ta interfaces (Figure 15 a) and clear diffraction patterns of LCO and LLZO:Al,Ta phases (Figure 15 b–d) can be observed. After cycling (C_10), the interface appears different and less sharp (Figure 15 e). A brighter contrast is observed on the LLZO:Al,Ta side of the LCO/LLZO:Al,Ta interface, and it looks as if an interface layer has formed (Figure 15 e, marked with red lines). A less defined SAED pattern, indicates a loss of crystallinity at the LCO/LLZO:Al,Ta interface (Figure 15 c, g), while the bulk LLZO:Al,Ta and LCO areas (about 1 μm away from the interface) appear quasi unchanged (Figure 15 b,d,f,h).

The same analysis was then performed on a sample after thermal recovery (Figure 15 i, j, k, l) at similar locations (LLZO:Al,Ta bulk, LLZO:Al,Ta, and LCO) as for the previous two samples. An unregular brighter contrast within the LLZO:Al,Ta is still visible when imaging with high-resolution TEM (Figure 15 i), which indicates that an interfacial layer between LCO and LLZO:Al,Ta remains even after annealing.

Within the LLZO:Al,Ta bulk the same distinct spots can be observed for the three samples (Figure 15 b,f,j), meaning that no significant structural change occurred. On the other hand if we compare the SAED taken on the LCO/LLZO:Al,Ta interface (Figure 15 c,g,k), it becomes obvious, that the cycled sample lost crystallinity which could be partly recovered by annealing. The blurry rings which are still visible after heat recovery indicate that the initial crystallinity may not be fully reestablished (Figure 15 k). This could partly explain why the heat treatment could not recover the original capacity (Figure 14 C_1 vs. R_1)

TEM images on the cycled sample reveal a contrast change at the grain boundary and a slightly inhomogeneous contrast within LLZO:Al,Ta. The observed change in

contrast must be a consequence of cycling as it is not visible in the uncycled state. After thermal recovery we can clearly see, that the grain boundary appears in a brighter contrast, however it is unclear if this change in contrast is related to the LCO, LLZO:Al,Ta or both.

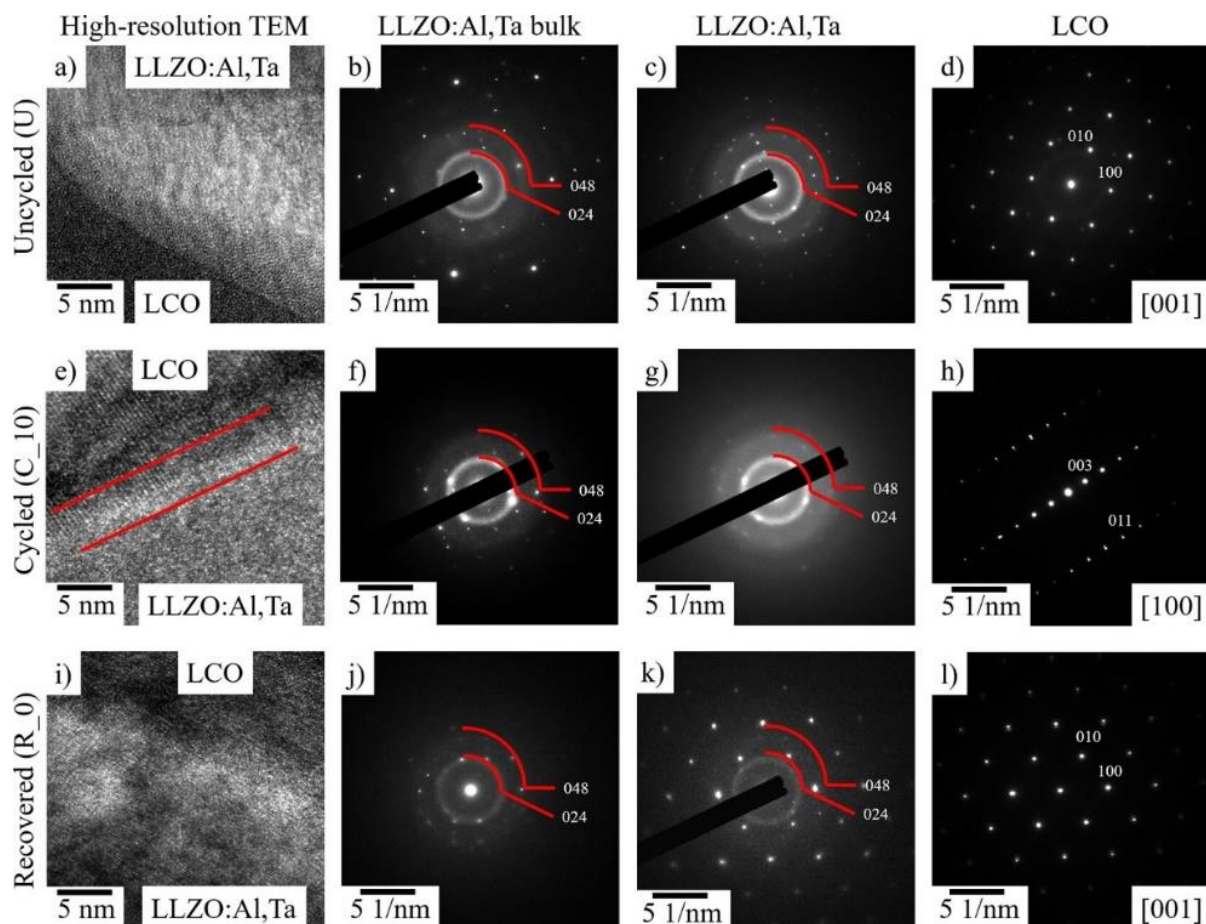


Figure 15: High-resolution TEM and SAED patterns of an uncycled (a–d), cycled (10 cycles, e–h), and recovered (i–l) LCO/LLZO:Al,Ta interface. In panel e, the formed interfacial layer between LCO and LLZO:Al,Ta is marked by red lines. The SAED of LLZO:Al,Ta bulk and LCO are measured around 1 μm away from the interface while LLZO:Al,Ta is measured at the LCO/LLZO:Al,Ta interface. (taken from ³²)

TEM images on the cycled sample reveal a contrast change at the grain boundary and a slightly inhomogeneous contrast within LLZO:Al,Ta. The observed change in contrast must be a consequence of cycling as it is not visible in the uncycled state. After thermal recovery we can clearly see, that the grain boundary appears in a brighter contrast, however it is unclear if this change in contrast is related to the LCO, LLZO:Al,Ta or both.

Contrast changes in the TEM images must be the consequence of either 1) thickness variations, which could be excluded due to a homogeneous lamella thickness; 2) different lattice orientation; or 3) local alterations of the atomic number (Z-dependence), meaning that element diffusion must have occurred. While cycling the difference in electrochemical potential can be the driving force for diffusion, however

during annealing (recovery) the driving force for element diffusion can only be the chemical potential between the most stable configurations. The elements which are most mobile and could undergo diffusion in this system are Li and Al.⁴²

To investigate the elemental distribution and how it changes due to diffusion, high-resolution, high-sensitivity SIMS is performed. The three samples (U, C_10, R_0) are analysed and Figure 16 shows the combined elemental maps (Figure 16 a, d, g) of Al (red), Co (blue) and La (yellow).

The chemical map of the uncycled sample in Figure 16 a-c shows that Co and La are strictly separated and only being detected within the grains of LCO and LLZO:Al,Ta, respectively. While WDXS measurements indicated (see Table 2), that Al might have accumulated and be enriched in the interface regions, Figure 16 a) clearly confirms this initial hypothesis. The SIMS line profiles (Figure 16 a-c) shows in b) an obvious increase of Al in the interface region, as well as a strong increase at LCO/LCO grain boundaries in c). All line profiles have been normalised for a qualitative evaluation; unfortunately, direct absolute quantification based on the signal intensities is not possible due to matrix effects.

The SIMS images of the cycled sample (Figure 16 d-f) clearly show an alteration of the Al distribution. Al is now broadly distributed in the LCO phase. While in some regions it seems as if the Al distribution would be homogenous, it is still visible that the signal is higher on the interfaces. However, some individual LCO grains contain no Al at all see in Figure 16 d) (white circle) and f) (line profile). Hence, we conclude that Al first diffuses to the LLZO:Al,Ta/LCO interface before it diffuses into grain boundaries. And in a second step during electrochemical charging/discharging, Al seems to diffuse almost homogeneously into the LCO phase.

The recovered sample (Figure 16 g-i) shows an important difference of the Al distribution compared to the cycled sample. Now, Al is distributed even more homogeneously through the LCO phase, especially on the inside of larger grains and on interfaces (LCO/LCO and LCO/LLZO). However, as already observed in the cycled sample, also the recovered state shows isolated Al-free LCO grains.

According to the SIMS analysis provided in this study, the presence of Al in the LCO-phase in the cycled and recovered samples is strong evidence that the electrochemically driven diffusion of Al-ions into LCO occurs during cycling and is not fully reversed by thermal recovery. Hence, the amount of diffused Al-ions, the site they occupy in the LCO lattice, and the structure of the resulting LCO phases may be different after different treatment steps (pristine, cycled, recovered).

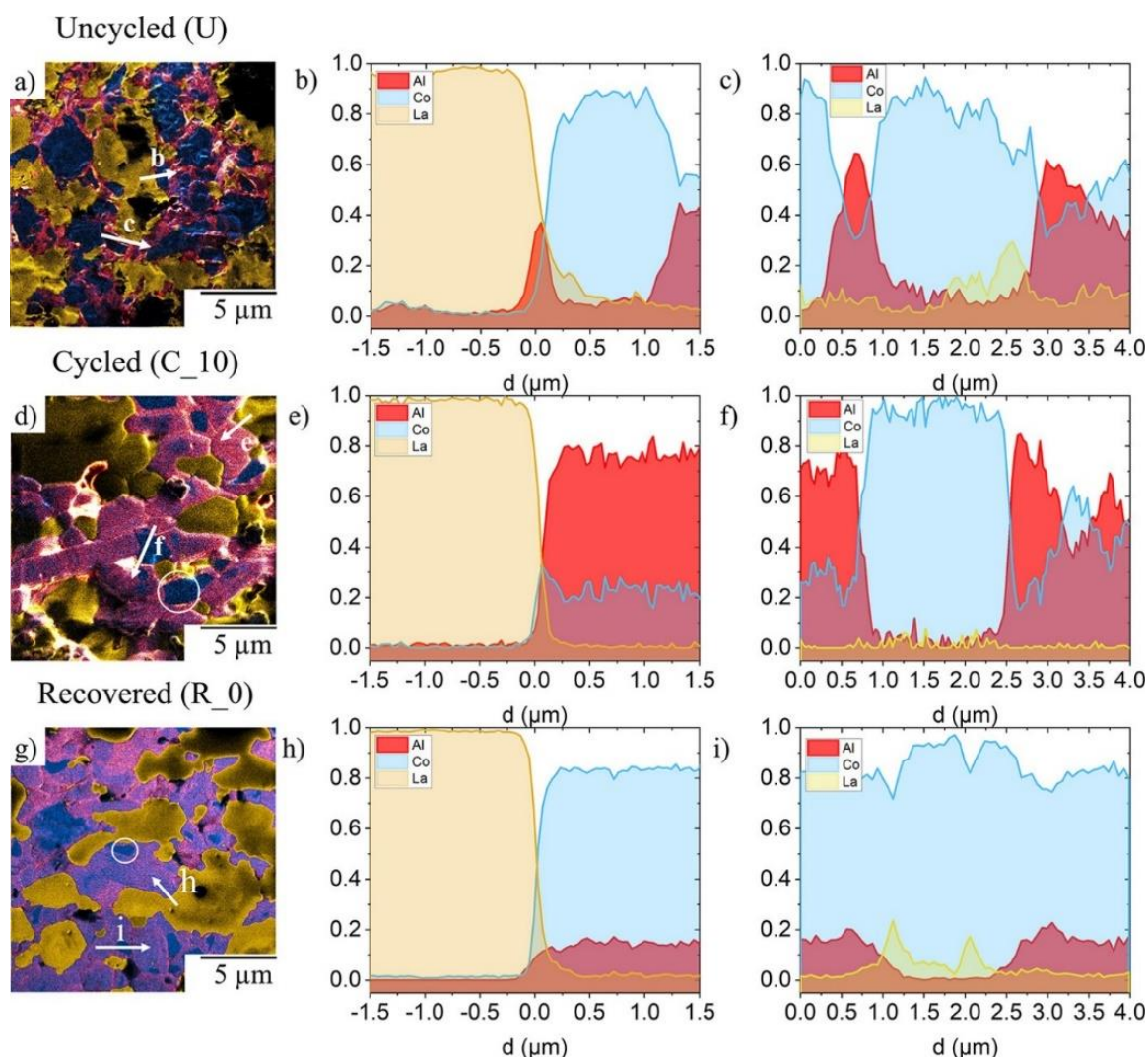


Figure 16: Elemental mappings with SIMS analysis for La (yellow), Al (red), and Co (blue) for the (a) uncycled, (d) cycled (10 cycles), and (g) recovered state. (The single elemental mappings are found in Figure S3.) Across the LCO/LLZO:Al,Ta interface (b, e, and h) and across the LCO/LCO interface (c, f, and i), SIMS line profiles have been prepared and the count for the La, Co, and Al signal is shown in relation to the combined elemental count in panels b and c for the uncycled, panels e and f for cycled, and panels h and i for the recovered state. The arrows in panels a, d, and g show the location and the direction of the SIMS line profiles.³²

Calculations to estimate the thermodynamically favourable sites for Al substitution have been performed. As different states of charge represent different vacant or occupied sites for Al substitution, two states were considered: the fully charged ($\text{Li}_{0.5}\text{CoO}_2$) and the discharged (LiCoO_2) LCO state. For the Al-Li substitution the possibility of two different sites was taken into account, e.g. the octahedral (octa. Li) or the tetrahedral (tetra. Li) site. The calculated formation energies can be found in Table 3. In the charged state, the formation energy for Al-ions substituted at the octahedral Li site of LCO is negative. And positive formation energies were found for all the other possible substitutions, indicating thermodynamic instability of such substitutions. Consequently, Al should preferentially diffuse into charged LCO and

occupy the octahedral Li sites. On the other hand, for the discharged state of LCO, a positive formation energy is found for all possible Al substitution sites, but by comparing the values we see that the formation energy for Al substituting Co sites is significantly lower than that for Li sites. For high-temperature sintering this has been frequently reported and experimentally confirmed.^{27,34,39} Based on the literature and the SIMS data (Figure 16 g–i), we can conclude that although it is thermodynamically unfavourable, some Al substitution remains even in the discharged state of LCO after high-temperature heat treatment (thermal recovery) and could explain why the lost capacity could not be restored to 100%.

Table 3: Overview of the Calculated Formation Energies for Al-Substituted into LCO ($\text{Li}_{27}\text{Co}_{27}\text{O}_{54}$) in the Li and Co Site in the Charged and Discharged State. Details can be found in ³².

fully charged ($\text{Li}_{15}\text{Co}_{27}\text{O}_{54}$) (eV/vacancy)			discharged ($\text{Li}_{27}\text{Co}_{27}\text{O}_{54}$) (eV/vacancy)		
Al (octa. Li)	Al (tetra. Li)	Al (Co)	Al (octa. Li)	Al (tetra. Li)	Al (Co)
$\text{Li}_{15}\text{AlCo}_{27}\text{O}_{54}$	$\text{Li}_{15}\text{AlCo}_{27}\text{O}_{54}$	$\text{Li}_{15}\text{Co}_{26}\text{AlO}_{54}$	$\text{Li}_{24}\text{AlCo}_{27}\text{O}_{54}$	$\text{Li}_{24}\text{AlCo}_{27}\text{O}_{54}$	$\text{Li}_{27}\text{Co}_{26}\text{AlO}_{54}$
-0.9	7.08	0.03	11.37	14.75	3.64

Based on the experimental evidence from TEM & SIMS, thermodynamic calculations, (and Raman spectroscopy data which is not presented in this case study, details can be found elsewhere³²) the following degradation and recovery mechanism can be presented:

- 1) Diffusion of Al-ions during sintering: In the context of Al-doped LLZO, it is well-documented that Al tends to migrate towards grain boundaries when exposed to high temperatures. In a composite system involving like LLZO:Al,Ta/LCO, it is observed that aluminum ions primarily diffuse into the interface between LCO and LLZO:Al,Ta, as well as into the grain boundaries within LCO. It is reasonable to assume that the resulting phase maintains adequate ionic conductivity, as the introduction of Al into LCO does not appear to have a substantial impact on the electrochemical properties.
- 2) Electrochemically driven diffusion of Al-ions: Thermodynamic calculations suggest that the diffusion of Al-ions into charged (delithiated) LCO is energetically favourable. This diffusion appears to be quite pronounced, as evidenced by SIMS. Since the thermodynamic calculations indicate that this diffusion primarily occurs along the lithium sites, the introduced Al ions obstruct the pathways for lithium-ion diffusion. Consequently, this obstruction leads to reduced ionic conductivity and electrochemical performance.

Simultaneously, the diffusion of Al from LLZO:Al,Ta results in the destabilization of the conductive cubic phase. This destabilization leads to the

formation of disordered or amorphous LLZO:Al,Ta, which also exhibits low ionic conductivity. Therefore, both of these factors contribute to the observed increase in resistance, and ultimately lead to a decrease in capacity over cycling.

- 3) Reorganisation of the Al distribution during thermal recovery: The thermodynamic calculations indicate that substituting Al in LCO is not energetically favourable in the discharged state. Consequently, during heat treatment in the discharged state, Al tends to be released from LCO. Nevertheless, as experimentally revealed, some Al ions remain trapped within the LCO structure, even after thermal recovery through annealing. These trapped Al ions most likely migrate from lithium sites to cobalt sites within the LCO structure. This migration results in the recovery of less than 100% of the initial capacity. However, it's worth noting that the internal resistance of the cell is nearly fully restored (~80%) after this thermal treatment. This suggests that both the obstruction of Li-ion diffusion pathways caused by Al on lithium sites within LCO as well as the amorphization of LLZO:Al,Ta are partly reversed by the thermal treatment.

Conclusion:

Initially, diffusion of Al was hypothesized based on EDX & WDXS results of a pristine sample. Subsequent SIMS analyses could prove the redistribution of Al in the different sample states (pristine, cycled, and recovered). TEM & SAED results show an obvious difference in the crystal structure, revealing that especially the LLZO/LCO interface loses crystallinity during cycling. Latter could be partially recovered by an annealing process. Additional thermodynamic calculations (and DFT Raman spectra simulation, not presented in the case study, details under³²) have been performed and provided essential pieces of the puzzle, before a mechanism for Al diffusion/redistribution could be presented.

This case study hypothesized a mechanism for the diffusion of Al-ions, claiming that Al first diffuses from LLZO:Al,Ta to the LCO/LLZO:Al,Ta interface, before it continues to spread along LCO grain boundaries. During cycling Al seems to homogeneously spread among the LCO phase, where Al seems to stay even after thermal recovery. Thermodynamic calculations indicate that Al could get trapped in the LCO phase and potentially migrate from an octahedral Li site to a Co site during annealing.

Additionally, this work proves that the electrochemical characteristics of a deteriorated LCO/LLZO:Al,Ta interface can be restored through thermal annealing, resulting in regained high ionic conductivity and reduced interfacial resistance. This

recovery is achieved by recrystallizing the previously amorphized LCO/LLZO:Al,Ta interface during the electrochemical process.

Although the initial storage capacity is not fully recovered, this approach demonstrates the potential for cost-effective recycling of garnet (LCO-LLZO:Al,Ta)-based ASSLBs. This method eliminates the need to break down the cell components to their raw material level. Potential reasons for the not fully recovered capacity could be a not completely recrystallized LLZO cubic phase (Figure 15 i,k) and/or the presence of inactive LCO particles (Figure 16 d & g white circles).

In conclusion, by implementing the described technique, the recycling process of garnet (LCO-LLZO:Al,Ta)-based ASSBs becomes easier, more efficient, and economically viable, while also reducing its environmental impact.

3.5. Closing Remarks

In this chapter we presented several X-ray based correlative analysis workflows.

In the first section, μ CT, was used to study the porosity of pristine and short-circuited LLZO solid electrolytes, to estimate the amount of Li occupying pores and intergranular cavities.

This is followed by an ex-situ correlative nanoCT-SEM-SIMS analysis of cathode materials combining two powerful instruments. By that demonstrating the feasibility as well as the compatibility of both techniques, which could be integrated within one common SEM. The study focussed on damaged AM. NanoCT was used to reconstruct the entire sample, and scope for potential ROIs, in a second step, SEM provides high resolution secondary electron images and SIMS was used for high-sensitivity chemical mapping.

After having studied the solid electrolyte and cathode material individually in the first two sections, the next section focusses on the complex 3D composite LLZO/LCO system. This study was initially performed via EDX and WDXS to characterize, but also quantify the chemical composition. Subtle hints regarding the Al-concentration (dopant in LLZO) indicated that potential metal diffusion could occur, subsequent SIMS analysis could confirm this initial hypothesis. This chapter is rounded up in an intense study regarding the electrochemical degradation of LLZO/LCO and its thermal recovery.

In the context of the model sample shown in Figure 2 in Chapter 2, we note that this chapter does not solely focusses on the solid-state electrolyte as it was the case for Chapter 2. This chapter combines X-ray based techniques with SEM-SIMS, complementing the analytical capability for the analysis of solid electrolytes and

CHAPTER 3

cathode materials. While μ CT was used to study the solid electrolyte, nanoCT (& SEM/SIMS) was used to study cathode material, then EDX & WDXS (& SIMS) analysis were performed to investigate the LLZO/LCO 3D interface.

ANNEXE 2

The following QR code, opens a video of a microscopic 3D reconstructed volume of a blended cathode material studied under “3.3. NanoCT for Cathode Material”. The sample material is described under “3.3.1. Sample preparation”. The reconstructed volume has a dimension of $18.5\ \mu\text{m} \times 12.4\ \mu\text{m} \times 5.8\ \mu\text{m}$.



Figure 17: QR-code showing a video of a FIB-SEM reconstructed volume of a blended cathode material (LCO and NCA).

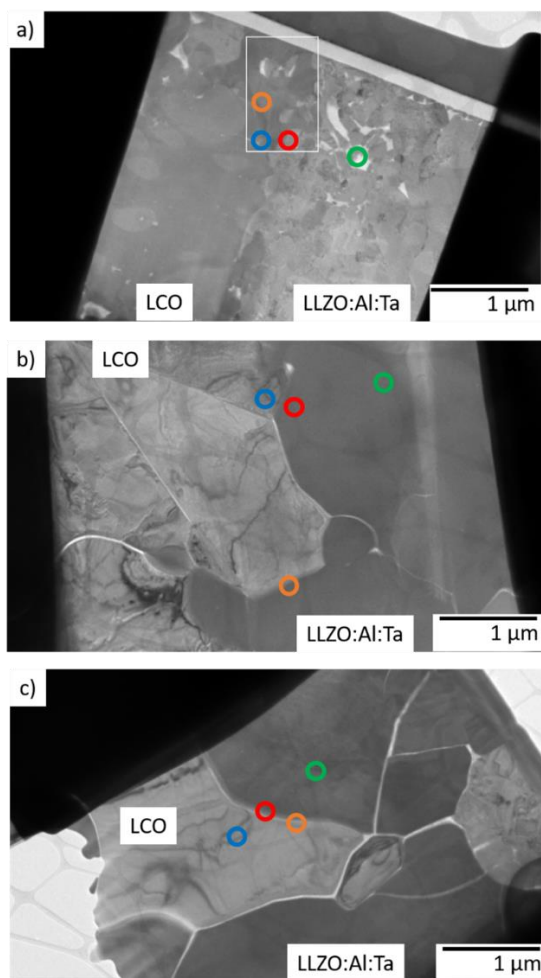


Figure 18: TEM images of an uncycled (a), cycled (b), and recovered (c) LCO/LLZO:Al,Ta interface. The circles show the locations of areas investigated by high-resolution TEM in orange and; blue for LCO; green for LLZO:Al,Ta; red for LLZO:Al,Ta bulk for the SAED pattern shown in Fig. 3. Reprinted with permission from ³².

References

- (1) Hernandez, A. M.; Boone, J. M. *Medical physics* **2014**, DOI: 10.1118/1.4866216.
- (2) Ganesh Kumar, K.; Balaji Bhargav, P.; Balaji, C.; Nafis, A.; Aravinth, K.; Ramasamy, P. *Journal of Electrochemical Energy Conversion and Storage* **2021**, DOI: 10.1115/1.4049573.
- (3) Jiang, Y.; Zhou, Y.; Hu, Z.; Huang, Y.; Zhu, X. *Ceramics International* **2020**, DOI: 10.1016/j.ceramint.2019.10.046.
- (4) Zhang, X.; Oh, T.-S.; Fergus, J. W. *J. Electrochem. Soc.* **2019**, DOI: 10.1149/2.1031915jes.
- (5) Castro, O. de; Audinot, J.-N.; Hoang, H. Q.; Coulbary, C.; Bouton, O.; Barrahma, R.; Ost, A.; Stoffels, C.; Jiao, C.; Dutka, M.; Geryk, M.; Wirtz, T. *Analytical chemistry* **2022**, DOI: 10.1021/acs.analchem.2c01410.
- (6) Schindelin, J.; Arganda-Carreras, I.; Frise, E.; Kaynig, V.; Longair, M.; Pietzsch, T.; Preibisch, S.; Rueden, C.; Saalfeld, S.; Schmid, B.; Tinevez, J.-Y.; White, D. J.; Hartenstein, V.; Eliceiri, K.; Tomancak, P.; Cardona, A. *Nature methods* **2012**, DOI: 10.1038/nmeth.2019.
- (7) Lutter, F.; Stahlhut, P.; Dremel, K.; Zabler, S.; Fell, J.; Herrmann, H.-G.; Hanke, R. *Nuclear Instruments and Methods in Physics Research Section B: Beam Interactions with Materials and Atoms* **2021**, DOI: 10.1016/j.nimb.2021.05.006.
- (8) Stahlhut, P.; Dremel, K.; Dittmann, J.; Engel, J. M.; Zabler, S.; Hoelzing, A.; Hanke, R., First results on laboratory nano-CT with a needle reflection target and an adapted toolchain. In *Developments in X-Ray Tomography X*; Stock, Stuart R.; Müller, Bert; Wang, Ge, Eds.; SPIE, 2016.
- (9) Stock, S. R.; Müller, B.; Wang, G., Eds. *Developments in X-Ray Tomography X*; SPIE, 2016.
- (10) Andersen, D.; Chen, H.; Pal, S.; Cressa, L.; Castro, O. de; Wirtz, T.; Schmitz, G.; Eswara, S. *International Journal of Hydrogen Energy* **2023**, DOI: 10.1016/j.ijhydene.2022.12.216.
- (11) Benninghoven, A.; Rüdenauer, F. G.; Werner, H. W. *Secondary ion mass spectrometry*; J. Wiley: New York, 1986.
- (12) Eswara, S.; Pshenova, A.; Yedra, L.; Hoang, Q. H.; Lovric, J.; Philipp, P.; Wirtz, T. *Applied Physics Reviews* **2019**, DOI: 10.1063/1.5064768.
- (13) Sui, T.; Song, B.; Dluhos, J.; Lu, L.; Korsunsky, A. M. *Nano Energy* **2015**, DOI: 10.1016/j.nanoen.2015.08.013.
- (14) Wang, C.-M.; Zhu, Z.; Engelhard, M. H.; Devaraj, A.; Baer, D. R. *Microsc. Today* **2016**, DOI: 10.1017/S1551929516000092.
- (15) Wirtz, T.; Castro, O. de; Biesemeier, A.; Hoang, H. Q.; Audinot, J.-N. *Microsc Microanal* **2020**, 26 (S2), 82–83.
- (16) KOKAM ENGINEERING CO., LTD. *Superior Lithium Polymer Battery SLPB 353452* **2002** (Kokam SLPB353452-DATA SHEET(020917)).
- (17) Ordoñez, J.; Gago, E. J.; Girard, A. *Renewable and Sustainable Energy Reviews* **2016**, DOI: 10.1016/j.rser.2015.12.363.
- (18) Priebe, A.; Audoit, G.; Barnes, J.-P. *Ultramicroscopy* **2017**, DOI: 10.1016/j.ultramic.2016.11.010.
- (19) Cressa, L.; Fell, J.; Pauly, C.; Hoang, Q. H.; Mücklich, F.; Herrmann, H.-G.; Wirtz, T.; Eswara, S. *Microsc Microanal* **2022**, DOI: 10.1017/S1431927622012405.
- (20) Engstler, M., Fell, J., Lutter, F., Maisl, M., Herrmann, H.G., Mücklich, F., Ed. *Correlative Tomography – Combining X-ray Nanotomography and FIB/SEM Serial Sectioning to analyze Al-Si cast alloys*; 10th Conference on Industrial Computed Tomography on Correlative: Wels, Austria (iCT 2020), 2020.
- (21) Dremel, K., Althoff, D., Zabler, S., Ed. *CT alignment correction in iterative reconstruction methods*, 2016.
- (22) Wirtz, T.; Castro, O. de; Hoang, H. Q.; Cressa, L.; Eswara, S.; Biesemeier, A.; Audinot, J.-N. *Microsc Microanal* **2021**, DOI: 10.1017/S1431927621003810.

- (23) ASTM Standard E 1441:2019. *Standart Guide for Computed Tomography (CT) Imaging*; ASTM International: West Conshohocken, PA.
- (24) Bessette, S.; Paoella, A.; Kim, C.; Zhu, W.; Hovington, P.; Gauvin, R.; Zaghbi, K. *Scientific reports* **2018**, DOI: 10.1038/s41598-018-33608-3.
- (25) Goodenough, J. B.; Kim, Y. *Chem. Mater.* **2010**, DOI: 10.1021/cm901452z.
- (26) Manthiram, A. *Nature communications* **2020**, DOI: 10.1038/s41467-020-15355-0.
- (27) Park, K.; Yu, B.-C.; Jung, J.-W.; Li, Y.; Zhou, W.; Gao, H.; Son, S.; Goodenough, J. B. *Chem. Mater.* **2016**, DOI: 10.1021/acs.chemmater.6b03870.
- (28) Ji, W.; Luo, B.; Wang, Q.; Yu, G.; Liu, Z.; Zhao, Z.; Zhao, R.; Wang, S.; Wang, X.; Zhang, B.; Zhang, J.; Hou, F.; Liang, J. *Adv. Energy Mater.* **2023**, DOI: 10.1002/aenm.202300165.
- (29) Li, J.; Wang, R. *Ceramics International* **2021**, DOI: 10.1016/j.ceramint.2021.02.034.
- (30) Ihrig, M.; Finsterbusch, M.; Laptev, A. M.; Tu, C.; Tran, N. T. T.; Lin, C.-A.; Kuo, L.-Y.; Ye, R.; Sohn, Y. J.; Kaghazchi, P.; Lin, S.; Fattakhova-Rohlfing, D.; Guillon, O. *ACS applied materials & interfaces* **2022**, DOI: 10.1021/acsami.1c22246.
- (31) Ihrig, M.; Finsterbusch, M.; Tsai, C.-L.; Laptev, A. M.; Tu, C.; Bram, M.; Sohn, Y. J.; Ye, R.; Sevinc, S.; Lin, S.; Fattakhova-Rohlfing, D.; Guillon, O. *Journal of Power Sources* **2021**, DOI: 10.1016/j.jpowsour.2020.228905.
- (32) Ihrig, M.; Kuo, L.-Y.; Lobe, S.; Laptev, A. M.; Lin, C.-A.; Tu, C.; Ye, R.; Kaghazchi, P.; Cressa, L.; Eswara, S.; Lin, S.; Guillon, O.; Fattakhova-Rohlfing, D.; Finsterbusch, M. *ACS applied materials & interfaces* **2023**, DOI: 10.1021/acsami.2c20004.
- (33) Kotobuki, M.; Kanamura, K.; Sato, Y.; Yoshida, T. *Journal of Power Sources* **2011**, DOI: 10.1016/j.jpowsour.2011.04.047.
- (34) Scheld, W. S.; Lobe, S.; Dellen, C.; Ihrig, M.; Häuschen, G.; Hoff, L. C.; Finsterbusch, M.; Uhlenbruck, S.; Guillon, O.; Fattakhova-Rohlfing, D. *Journal of Power Sources* **2022**, DOI: 10.1016/j.jpowsour.2022.231872.
- (35) Tsai, C.-L.; Ma, Q.; Dellen, C.; Lobe, S.; Vondahlen, F.; Windmüller, A.; Grüner, D.; Zheng, H.; Uhlenbruck, S.; Finsterbusch, M.; Tietz, F.; Fattakhova-Rohlfing, D.; Buchkremer, H. P.; Guillon, O. *Sustainable Energy Fuels* **2019**, DOI: 10.1039/C8SE00436F.
- (36) Banerjee, A.; Wang, X.; Fang, C.; Wu, E. A.; Meng, Y. S. *Chemical reviews* **2020**, DOI: 10.1021/acs.chemrev.0c00101.
- (37) Rawlence, M.; Garbayo, I.; Buecheler, S.; Rupp, J. L. M. *Nanoscale* **2016**, DOI: 10.1039/C6NR04162K.
- (38) Thangadurai, V.; Narayanan, S.; Pinzaru, D. *Chemical Society reviews* **2014**, DOI: 10.1039/c4cs00020j.
- (39) Wang, C.; Fu, K.; Kammampata, S. P.; McOwen, D. W.; Samson, A. J.; Zhang, L.; Hitz, G. T.; Nolan, A. M.; Wachsmann, E. D.; Mo, Y.; Thangadurai, V.; Hu, L. *Chemical reviews* **2020**, DOI: 10.1021/acs.chemrev.9b00427.
- (40) Wang, D.; Zhu, C.; Fu, Y.; Sun, X.; Yang, Y. *Adv. Energy Mater.* **2020**, DOI: 10.1002/aenm.202001318.
- (41) Inada, R.; Takeda, A.; Yamazaki, Y.; Miyake, S.; Sakurai, Y.; Thangadurai, V. *ACS Appl. Energy Mater.* **2020**, DOI: 10.1021/acsaem.0c02474.
- (42) Tsai, C.-L.; Dashjav, E.; Hammer, E.-M.; Finsterbusch, M.; Tietz, F.; Uhlenbruck, S.; Buchkremer, H. P. *J Electroceram* **2015**, DOI: 10.1007/s10832-015-9988-7.

CHAPTER 4

1. CHAPTER 1 Background
2. CHAPTER 2 Correlative SEM/SIMS
3. CHAPTER 3 X-ray Based Correlative Approaches
4. CHAPTER 4 *Operando* Neutron Imaging
 - 4.1. Motivation
 - 4.2. Experimental Design
 - 4.2.1. Design of the Sample Holder
 - 4.2.2. Final Experimental Configuration
 - 4.3. Material & Methods
 - 4.3.1. Sample Preparation for *Operando* Neutron Imaging
 - 4.3.2. Neutron Tomo- & Radiography
 - 4.3.3. Sample Preparation for *ex-situ* SEM/SIMS Analysis
 - 4.4. Results
 - 4.4.1. *Operando* Neutron Imaging
 - 4.4.2. Li Quantification
 - 4.4.3. From Neutron Imaging to Secondary Ion Mass Spectrometry
 - 4.4.4. Post-Mortem Structural and Chemical Characterisation
 - 4.4.5. Proposed Hypothesis
 - 4.4.6. Limitations
 - 4.5. Conclusions

ANNEXE 3

References

4.1 Motivation

This chapter focusses on the design and execution of an *operando* neutron imaging experiment. Furthermore, post-mortem SEM/SIMS analysis was performed. Our methodology is based on an *operando* experiment of a solid-state half cell (Li/LLZO/Li) which is being cycled until short-circuit failure under neutron irradiation for analysis. Post-mortem investigation will be performed: 1) via secondary electron imaging for structural analysis and 2) via SIMS for chemical mapping. Hence creating complementary data sets between neutron radiography - being a quantitative transmission technique - and correlative SEM and SIMS imaging allowing high resolution high sensitivity structural and chemical imaging.

The current study shows a correlative analysis and characterization approach aiming to show the complexity and potential of *operando* methodologies and by that supporting battery research for an accelerated development. The results discuss different dendrite types and their formation, Li quantification and shed light from a more critical point of view on *operando* approaches.

4.2 Experimental Design

The overall experimental plan consists of:

- 1) Before cycling one neutron tomography measurement is performed (125 projections = 2.88° angle per scan) allowing to get a three-dimensional reconstruction of the pristine sample.
- 2) Two-dimensional radiography measurements are performed during the cycling of the battery until short-circuit failure (*operando*).
- 3) After the short-circuit failure another tomography measurement is performed (identical experimental conditions), to have a three-dimensional comparison between pristine and short-circuited sample.
- 4) Correlative SEM and SIMS analysis (surface sensitive).

The approach comes with particular challenges, first the presence of metallic Li in the sample requires the system to be always in a controlled atmosphere to prevent oxidation of Li. A second obstacle is the overall experimental design as well as the sample holder design for the neutron imaging.

4.2.1 Design of the sample holder

The *operando* neutron imaging experiment necessitates a custom-designed sample holder as multiple requirements need to be satisfied; regarding materials which are

used, dimensions, compatibility with the sample stage of the ICON beamline¹. In addition, it should be air-tight to prevent Li from getting into contact with the ambient air. The design of the sample holder for the *operando* neutron imaging experiment can be seen in Figure 1. For instance, in a) the outer shell parts (1: Electrode Screw male and 2: Electrode Screw female) are represented, in b) the parts on the inside of the sample holder are shown: a screw (3) and pressure pin (4) are made from Ti alloy. The pressure oxide cylinder (5) and the oxide sample cylinder (8) parts are made of Al_2O_3 . The latter are crucial for a successful experiment because (5) is responsible to electronically separate both electrodes, making it possible to cycle the sample. (8) holds the sample, meaning it needs to be an insulator and practically transparent to neutrons which is the case for Al_2O_3 . (6) and (9) represent O-rings which allow a certain degree of compressibility. The dimensions of the sample holder are 40 mm height, 18 mm radius where the sample is positioned with a wall thickness of 1.5 mm for the outer metallic shell and 4.7 mm for the oxide sample cylinder.

EIS measurements were performed on Li based samples inside and outside of the glove box to test whether the sample holder is airtight. A leak in the design would inevitably lead to oxidation of Li, which would be measurable by an increased impedance. Needless to say, that any leak would be fatal for the experiment.

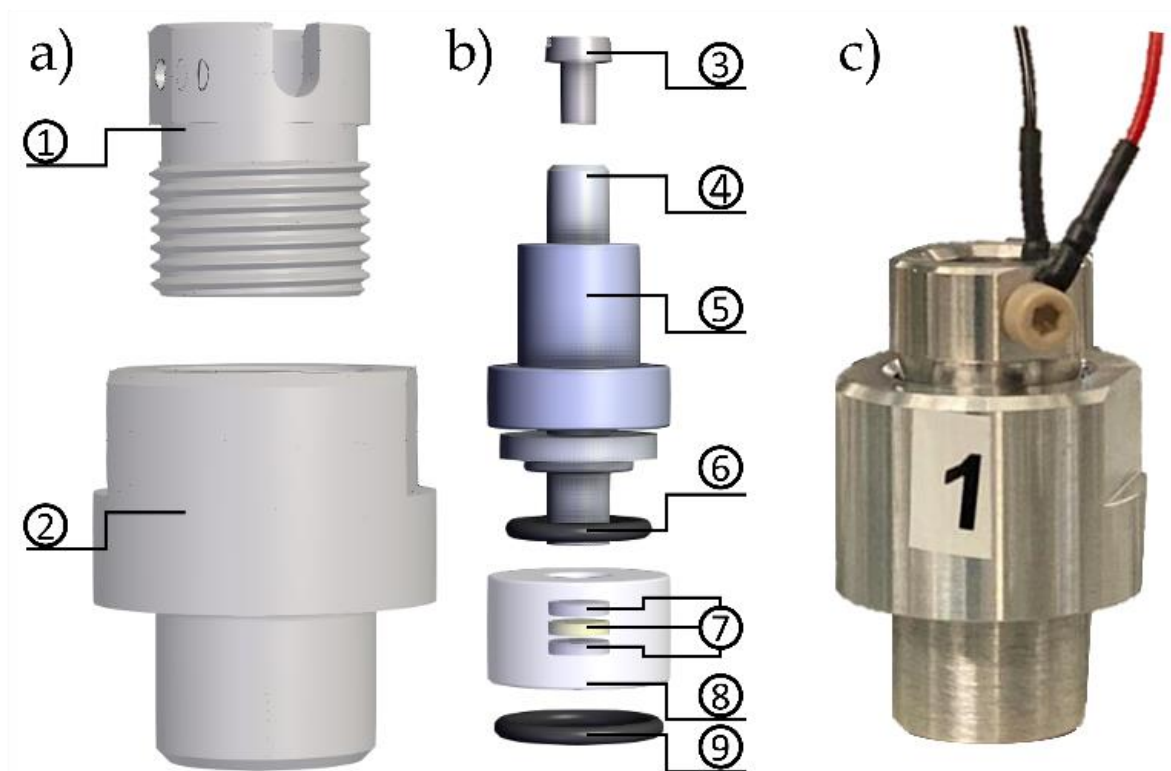


Figure 1: Design of the sample holder for *operando* neutron imaging of solid-state half cells. a) Outer shell parts with 1- electrode screw male and 2- electrode screw female. b) Inner parts of the sample holder: 3- screw; 4- pressure pin; 5- pressure oxide cylinder; 6- small O-ring; 7- Li/LLZO/Li half-cell; 8- oxide sample cylinder; 9- large O-ring. c) picture of the assembled sample holder with electrode cables attached.

4.2.2 Final Experimental Configuration

A potentiostat is connected to both contacts of the sample holder for electrochemical experiments. One contact is connected to the electrode screw male (1) (Figure 1 c & Figure 15 red cable) and the second is connected between a screw (3) and the pressure pin (4) (Figure 1 & Figure 15 c black cable), the pressure oxide cylinder (5) separates both poles electronically. The final experimental configuration is shown in Figure 15 where a potentiostat is attached to both contacts (red and black cables) as described before, and a PC connected to the potentiostat monitors and controls the electrochemical experiment. The sample holder gets positioned in between the beamline and the detector in order to perform simultaneous neutron imaging and electrochemical cycling. (Figure 15)

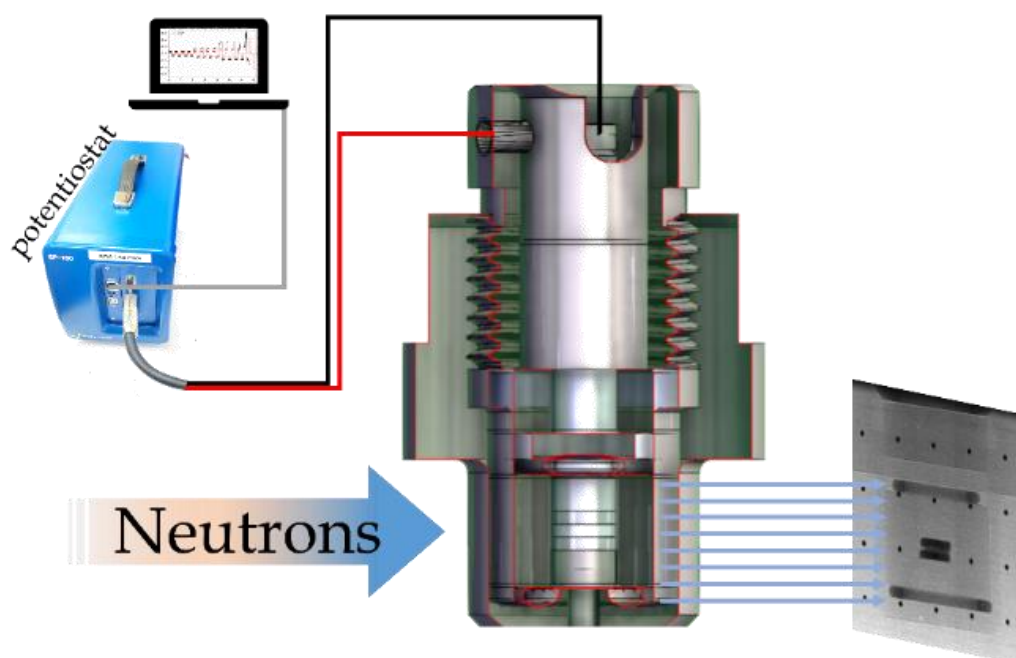


Figure 2: Schematics of the final experimental configuration of the operando neutron radiography. The potentiostat is attached to both polarities (red and black cables) of the sample holder and to a PC which monitors and controls the electrochemical experiment. During cycling the neutron beam will penetrate the sample and due to different attenuation coefficients of the elements, radiographs can be recorded.

4.3 Materials and methods

The LLZO pellets were synthesized the same way as described in Chapter 2 under “Materials & Methods”, resulting in high density pellets ($\sim 5.16 \text{ g/cm}^3$). After sintering, the pellets were polished using different sandpapers until they have dimensions of 11 mm in diameter and 1-1.5 mm in thickness. The metallic Li-foil which is used to assemble the half-cell is from Alfa Aesar (CAS-No. 7439-93-2). No liquid electrolyte nor special pre-treatment on the Li foils were used in this work.

4.3.1 Sample preparation for *operando* neutron imaging

As the neutron beam penetrates through the cross-section of the sample and not through its thickness, it is important to design the half cell with a radius as small as possible, to have penetration path which is small enough for neutrons to be transmitted. Hence the LLZO pellet was polished to a radius of ~ 2.1 mm and a thickness of ~ 0.9 mm. Figure 3 shows a 3D reconstruction of the Li- foils and the LLZO pellet.



Figure 3: Exemplary 3D reconstruction of the Li/LLZO/Li sample generated from the neutron tomography data.

4.3.2 Neutron Tomo- & Radiography

The measurements were conducted at the ICON¹ (Imaging with Cold Neutrons) beam line of the SINQ neutron source at Paul Scherrer Institute (PSI). For the radiography measurement, a source aperture of 20 mm was used, resulting in a L/D ratio (length-to-diameter ratio) of 350 and a geometric blurring of approximately 50 μm for the sample detector distance of 19 mm. The neutron images were acquired using the micro-setup detector, featuring a field of view of $27 \times 27 \text{ mm}^2$ and a pixel size of 13.5 μm . The neutrons were converted to visible light using a scintillator screen made of Tb doped $\text{Gd}_2\text{O}_2\text{S}$, with a thickness of 20 μm . The produced visible image was captured by a CCD camera (Andor Ikon-L, 2048×2048 pixels). The exposure time for single images was set to 30 s. For the tomography measurements, the source aperture was increased to 40 mm, resulting in a twofold increase of the geometric blur (100 μm) but allowing faster tomographies due to the increase of neutron flux. The tomographies were acquired using 125 angle steps distributed over 360° , resulting in a total acquisition time of approximately 1 hour.

For the radiography time series, the following image processing was applied:

- I. Subtraction of the camera background.
- II. Filter for white spots caused by gamma rays hitting the detector.
- III. Removal of high spatial frequency noise using a Gaussian filter.
- IV. Removal of the heterogeneity in the scintillator screen sensitivity by division of an open beam image.

- V. Correction of the beam intensity fluctuations by measuring the intensity in a non-changing area.
- VI. Correction of the cell movement using fixed features of the cell as fiducials.
- VII. Subtraction of the scattered background using the black body grid method².
- VIII. Division by an image of the initial state in order to see the changes due to Li accumulation.
- IX. Conversion to optical density using the formula $OD = -\ln\left(\frac{I}{I_0}\right)$.

Where OD is the optical density, I is the dose of neutrons that passes through the sample and reaches the detector, and I_0 is the original neutron dose being emitted from the source, before it interacts with the sample. The ratio of I to I_0 , is defined as the transmittance. Radiographs were recorded every 30 s however to reduce noise, the images were grouped by 30 minutes intervals, and the resulting “grouped” images were averaged pixel-wise. This means that 60 radiographs (= 30 min with 1 radiograph every 30 s) are overlaid and the “values” i.e. the measured intensities (0-255) of every pixel are summed. The result is an (over 30 minutes) averaged radiograph. The processing described above was performed using in-house developed scripts written in Python. The tomography data was reconstructed using the PSI developed MuhRec³ software. The 3D reconstructions (e.g. Figure 3) were performed using the commercial software AVIZO (Version 2021.1., ThermoFisher).

4.3.3 Sample preparation for *ex-situ* SEM/SIMS analysis

After the *operando* neutron imaging experiment, the sample holder (including the sample) was activated by neutron irradiation, meaning that the sample holder needed to be safely stored until the radioactive decay reached a non-critical level (approximately one week). In a subsequent step, the sample holder was opened inside an Ar-glove box ($[O_2]=\sim 0.6$ ppm; $[H_2O]=\sim 0.8$ ppm) and cut in half in order to analyse the inside of the half-cell. Different preparation techniques for SEM/SIMS bulk analysis of solid-state batteries can be found elsewhere⁴ (Chapter 2).

4.3.4 SIMS analysis

SIMS imaging was performed using a Thermo Fisher Scios DualBeam FIB-SEM equipped with an in-house developed double-focusing magnetic sector SIMS system which allows the detection of multiple masses in parallel^{5,6}. The FIB consists of a gallium liquid metal ion source producing $^{69}\text{Ga}^+$ primary ions. The secondary ions that were collected and imaged are: $^7\text{Li}^+$. The SIMS measurements were carried out with a primary ion beam energy of 30 keV, a beam current of 50 pA, and a dwell time 0.5 ms per pixel. The images were recorded with a resolution of 512×512 pixels and fields of view between 20×20 and 30×30 μm . To extract positive secondary ions, the sample was biased to +500 V which resulted in a primary ion impact energy of 29.5

keV. Data analysis was performed using the free software ImageJ⁷ and the commercial software AVIZO (Version 2021.1., Thermo Fisher).

4.4 Results

After the preparation of the solid electrolyte half-cell sample (Li-LLZO-Li) and the proper placing inside the custom-designed sample holder, the latter was positioned between the neutron beamline and the detector to perform the experiment. The cables (see Figure 1 c and Figure 2) were connected to both polarities of the sample holder and to the potentiostat. After proper positioning, general setting optimisation and a few calibration measurements¹ (open beam black body², open beam, dark current), neutron tomography could be performed. An angular step of 2.88° was chosen resulting in 125 projections, the exposure time per measurement was 20 s. Tomography measurements were performed before cycling the sample and after short-circuit failure; during cycling 2-dimensional radiography measurements were performed.

4.4.1 *Operando* Neutron Radiography

Before *operando* radiography measurements could be performed, calibration measurements (open beam black body, open beam, dark current) needed to be performed again. For radiography an exposure time of 30 s per measurement was chosen. The cycling parameters were initially chosen to incite a short-circuit failure of the Li-LLZO-Li sample within 24 h with four different current density settings 5, 10, 20 and 40 $\mu\text{A}/\text{cm}^2$ and 12 cycles for each setting. One full cycle took 30 minutes, resulting in $4 \times 12 \times 30 \text{ min} = 24 \text{ h}$. However, as the half-cell did not short-circuit after 24 h, we decided to increase the current density to force a failure of the half cell. One cycle with a current density of 80 $\mu\text{A}/\text{cm}^2$ and two cycles with a current density of 160 $\mu\text{A}/\text{cm}^2$ were added. Figure 4 a) shows the voltage profile (black) and the current (red) as a function of time. Small alterations of the voltage profile are noticeable between 19-20 h (cycle: 39-40) which seems to recover in the following cycles (41-44 \rightarrow time = 21-22.5 h), coming back to expected voltage profile. From cycle 45, the voltage profile changes and won't recover until short-circuit at cycle 50. The last cycle (51) was performed to test whether the sample is fully short-circuited or if it will recover.

Figure 4 b) shows neutron radiographs at different stages of the experiment, at the 1st, 15th, 31st and 50th cycle, respectively. The big bright dot visible in all radiographs results from using a black body grid with Gadolinium dots, having the highest neutron attenuation upon all elements, which is necessary for the correction of systematic biases such as scattered neutrons and other sources such as light reflections in the detector system². The two highlighted regions on the left half of the sample (blue and green box), show considerable change of the optical density during cycling. The right side of the pellet does not show any trend of the optical density during cycling,

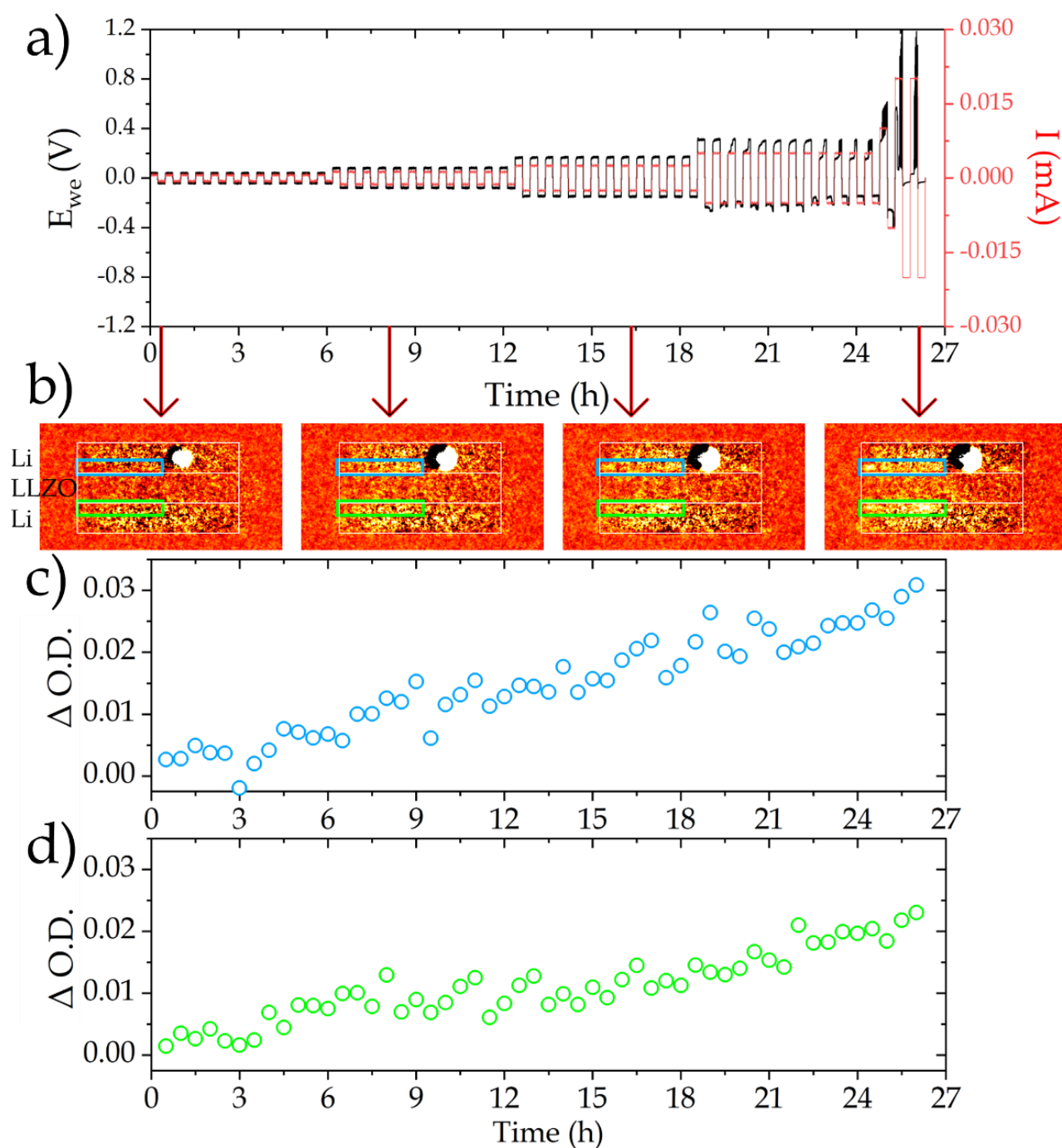


Figure 4: Operando neutron imaging. a) Voltage profile (black) and applied current densities (red): four different current density settings 5, 10, 20 and 40 $\mu\text{A}/\text{cm}^2$ with 12 cycles for each. Three additional cycles, one with a current density of 80 $\mu\text{A}/\text{cm}^2$ and two cycles with a current density of 160 $\mu\text{A}/\text{cm}^2$ were added to force a short-circuit of the half-cell. b) Radiographs of the half-cell at different stages of the operando experiment, at the 1st, 15th, 31st and 50th cycle, respectively. The horizontal FOV of each radiograph is 6.3 mm. The highlighted regions (cyan and green box) represent regions with the most alteration of the O.D. during the cycling. c) & d) Diagrams of $\Delta O.D.$ as a function of time (1 h = 2 cycles), the cyan highlighted region shows a difference of $\sim 3\%$ and the green highlighted region a difference of $\sim 2.5\%$, respectively.

at least not for larger regions. The diagrams in Figure 4 c) & d) show the change of optical density inside the cropped boxes during the cycling (time resolution = 30 min resulting in 52 data points) elucidating a $\Delta O.D. > 3\%$ (blue box) and $\sim 2.5\%$ (green box).

A 2nd experiment was carried out to insure reproducibility and reliability of our custom-designed experimental set-up. This additional neutron *operando* experiment was performed with 14 cycles (~7 h), followed by post-mortem SEM/SIMS analysis (ANNEXE 3). The reason for the different number of cycles of both experiments is purely related to the limited beam-time. Post-mortem analysis uncovered comparable Li-degradation artefacts in both samples (see “4.4.4. Post-Mortem structural and chemical characterisation” and ANNEXE 3), ensuring reproducibility.

4.4.2 Li quantification

To relate the optical density to the volume of lithium in the electrolyte, the following calculation was conducted. The effective transmission through the sample can be calculated as⁸:

$$\frac{I}{I_0} = \frac{\int I_0(E) \cdot c_{eff}(E) \cdot e^{-[\Sigma_{el}(E) + \Phi \cdot \Sigma_{Li}(E)] \cdot d} \cdot dE}{\int I_0(E) \cdot c_{eff}(E) \cdot dE} \quad (0.1)$$

Where $I_0(E)$ is the beam spectrum (energy dependent intensity), $c_{eff}(E)$ is the energy dependent detector capture efficiency, $\Sigma_{el}(E)$ is the neutron linear attenuation coefficient of the electrolyte, $\Sigma_{Li}(E)$ is the neutron linear attenuation coefficient of lithium, Φ is the volume of lithium dendrites and d is the thickness of the electrolyte in the direction of the neutron beam.

$$OD = -\ln\left(\frac{I}{I_0}\right) \quad (1.2)$$

Based on the electrolyte composition ($\text{Li}_7\text{La}_3\text{Zr}_2\text{O}_{12}$) with a specific weight of 5.16 g/cm³ and using the energy dependent neutron attenuation cross sections of Li, La, Zr and O from the ENDF VIII database (Ref: <https://www.nndc.bnl.gov/endl-b8.0/>), the energy dependent linear attenuation coefficients of the electrolyte could be computed, as reported in Figure 5.

The neutron linear attenuation coefficient of the electrolyte as a function of energy (Figure 5 a), shows the contribution of the different elements of LLZO. The diagram elucidates that Li in the LLZO crystal structure has the main contribution regarding neutron attenuation. Figure 5 b) demonstrates the linear attenuation coefficient as a function of the volume of Li dendrites present within the electrolyte. Based on equation (0.1), the change of optical density (absolute O.D., & the transmission) for the ICON beam line as a function of Li dendrite volume, assuming an average electrolyte thickness of 4 mm in the direction of the neutron beam (corresponding to the central section of the round shape electrolyte disk) could be computed (Figure 6).

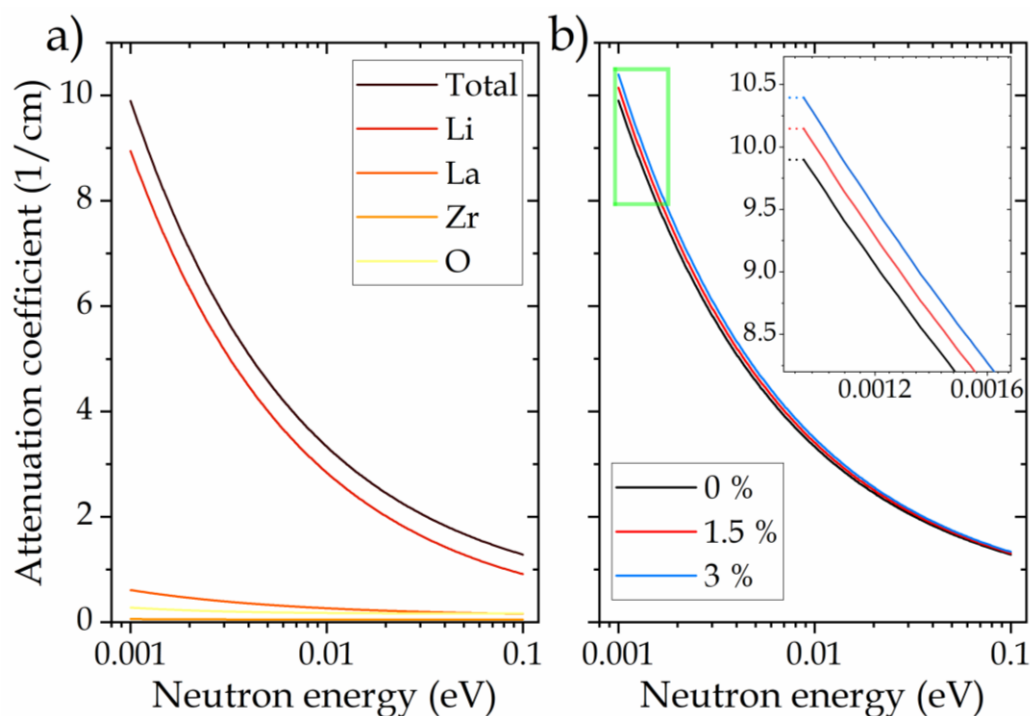


Figure 5: (a) Neutron linear attenuation coefficient of the electrolyte as a function of energy, showing the contribution of the different components (b) Linear attenuation coefficient as a function of the Li dendrites volume within the electrolyte.

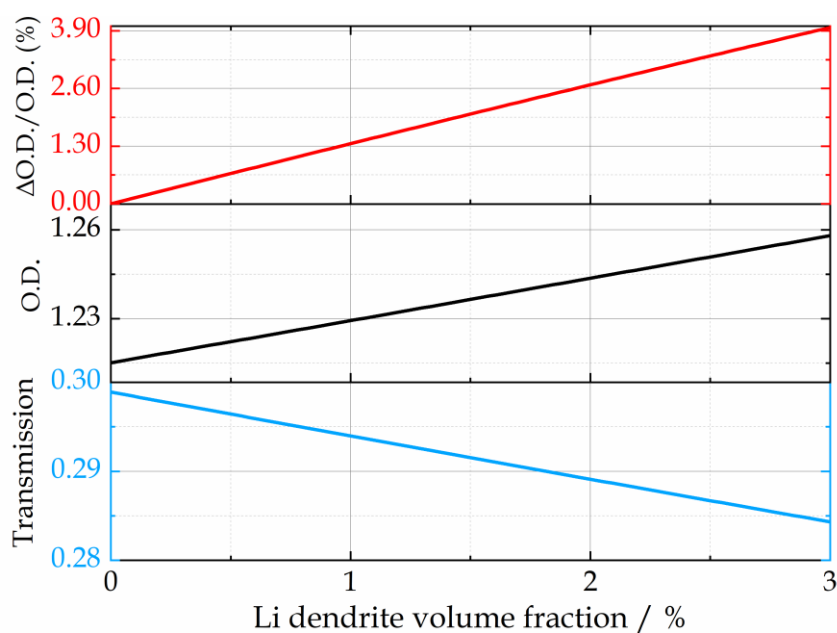


Figure 6: Transmission, optical density, and change of optical density as a function of the volume of Li dendrites, for the ICON beam line and for an electrolyte thickness of 4 mm.

The values of $\Delta O.D./O.D.$ in Figure 6 can be used to evaluate the Li dendrite volume responsible for the changes reported in the radiographs (Figure 4 c, d & Figure 7). For instance, according to our calculations, regions in the radiographic images with $\Delta O.D./O.D.$ of 2% represent a difference of Li dendrite volume of $\sim 1.5\%$.

Battery degradations can occur very localized and one single dendritic filament can in principle short-circuit the battery. The spatial resolution of the ICON beamline does

not allow to detect single sub-micron scale dendrites, however larger ($>20\ \mu\text{m}$) localized Li accumulations can be spotted.

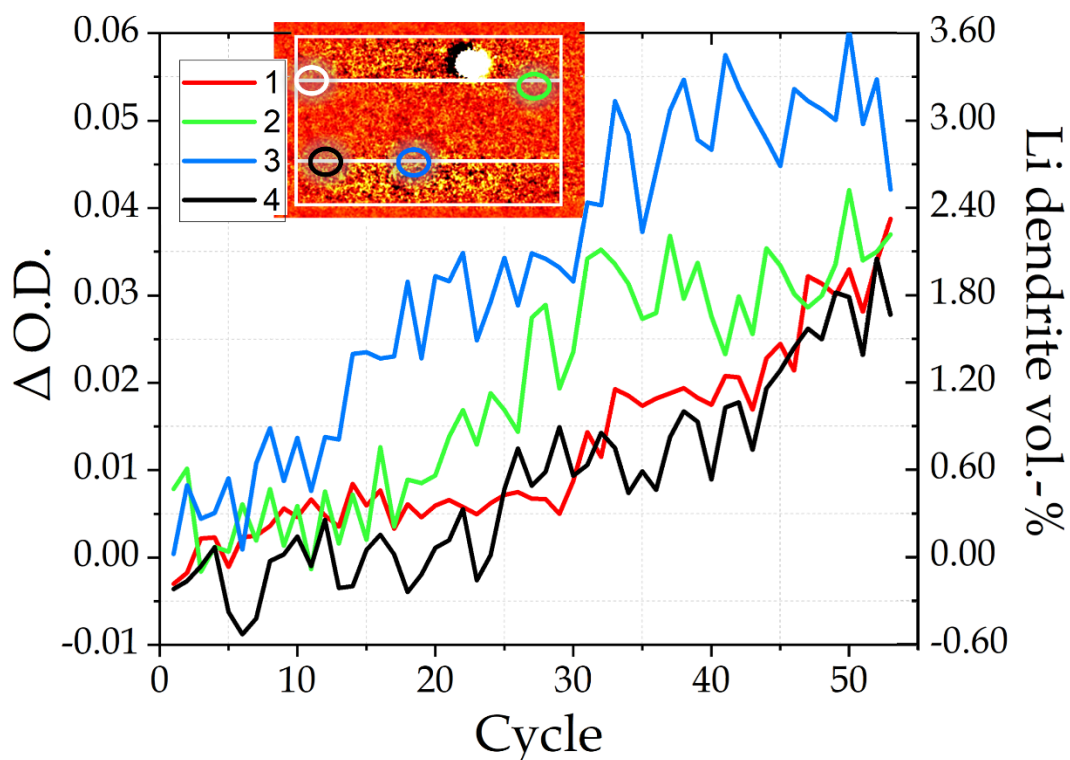


Figure 7: Diagram of $\Delta\text{O.D.}$ as a function of cycles at localized regions. The regions which were chosen for this evaluation are shown in the radiograph inset (1=white; 2=green; 3=blue and 4=black). The horizontal FOV of the radiograph is 4.9 mm. All the regions of considerable $\Delta\text{O.D.}$ are at the interface between Li and LLZO and show fluctuations of the O.D. between 3 and 6 %.

Figure 7 shows a diagram of $\Delta\text{O.D.}$ as a function of cycles at localized regions, which were chosen for this evaluation (radiograph inset: 1=white; 2=green; 3=blue and 4=black). In Figure 4 as well as in Figure 7 all the regions of considerable $\Delta\text{O.D.}$ are at the interface between Li and LLZO and show fluctuations of the O.D. between 2.5 and 6 %. This means that the Li dendrite volume in those regions, which grew during cycling, is between 1.5 and 3.6 %. As mentioned above, usually dendrite formation and propagation are not homogeneously within batteries, hence a single dendritic connection from one electrode to the other can already cause short circuit failures. As the resolution of neutron imaging is only $\sim 30\ \mu\text{m}$, only larger ($>20\ \mu\text{m}$) Li-accumulations will become detectable by neutron imaging.

4.4.3 From Neutron Imaging to Secondary Ion Mass Spectrometry

Neutron activation occurs when a material (activation of different elements differ greatly) is exposed to a flux of neutrons, resulting in the creation of radioactive isotopes within the material. When the neutrons interact with the atomic nuclei of the material, they can induce nuclear reactions, leading to the transformation of stable isotopes into radioactive isotopes. These undergo radioactive decay, emitting

radiation in the form of gamma rays, beta particles, or alpha particles. The specific type and energy of the radiation emitted depend on the radioactive isotopes produced during the activation process.

It's crucial to take neutron activation into account after neutron irradiation experiments to ensure personal and the environmental protection, as radioactive materials can pose risks to human health and the surrounding ecosystem. Only after sufficient radioactive decay, it was safe and possible to transport the sample for subsequent post-mortem SEM/SIMS analysis.

4.4.4 Post-Mortem Structural and Chemical Characterisation

The sample holder was introduced in a glove box before it could be opened and prepared as described in Chapter 2. In the following, the sample was transferred from the glove box to the FIB-SEM-SIMS instrument via an inert gas transfer system⁴.

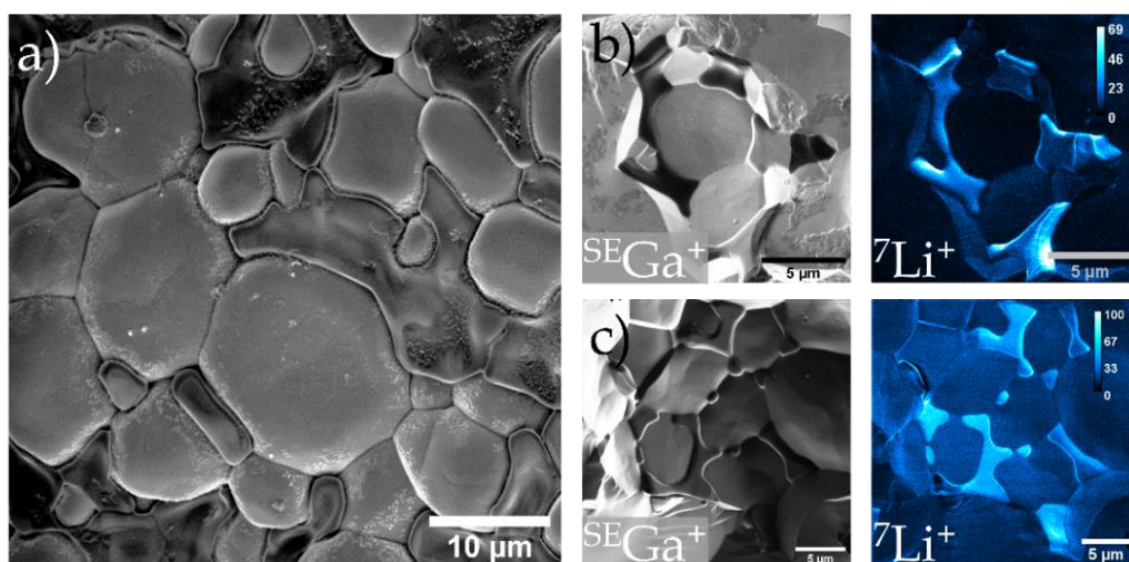


Figure 8: a) Secondary electron images recorded by ion irradiation ($^{69}\text{Ga}^+$), and correlative secondary electron and chemical maps of $^7\text{Li}^+$ (b & c).

Secondary electron imaging immediately reveals that a compositional change must have occurred, as a second phase, different from LLZO becomes visible. Figure 8 reveals in a) the dark phase which seems to be mostly located in intergranular spaces. Figure 8 b) and c) show two secondary electron images with smaller FOVs which clearly show that the dark phase is preferentially localised in grain boundaries. Additionally, SIMS imaging has been performed at the exact same locations as b) and c) elucidating that the dark phase which appeared as a consequence of cycling is Li-rich. While several researchers were able to observe similar degradation features after short-circuiting LLZO based batteries, only a few were able to directly prove the presence of Li on these phases.

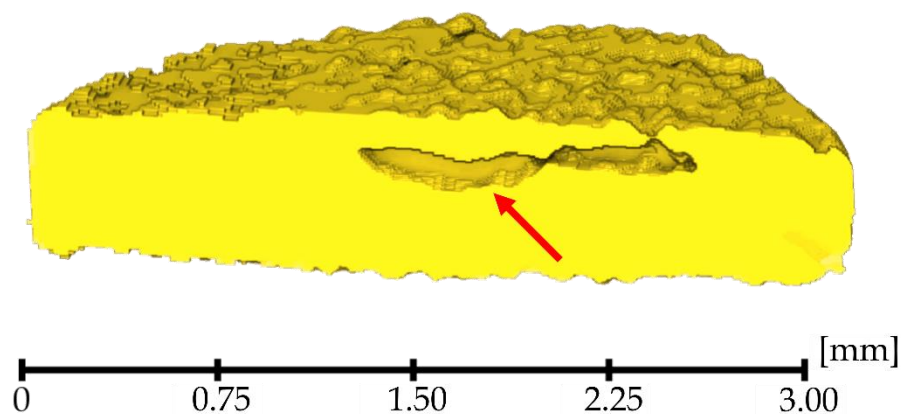


Figure 9: 3-dimensional reconstruction of the pristine LLZO pellet based on the neutron tomography data. This cross section elucidates a dense material; however, one larger crack is visible in the centre of the pellet. SE/SIMS images from Figure 8 were recorded in dense regions, while images in Figure 11 were taken in the proximity of the crack (red arrow).

While the images from Figure 8 were taken from very dense bulk-regions of the LLZO, Figure 10 shows images taken at the proximity of an internal crack in the bulk of the LLZO pellet. Figure 9 shows a reconstructed 3-dimensional cross-section of the uncycled LLZO pellet, elucidating the presence of a large crack in the bulk. Impurities or defects like pores and cracks are undesired, as they reduce the electrochemical performance and encourage parasitic Li-accumulations. It is unclear if this crack was produced during sample preparation for the neutron experiment or already when synthesising/pressing the pellet. It is just clear that the crack did not appear during cycling, as it could already be seen in the tomography of the uncycled half-cell.

To our surprise, different morphologies of the Li-rich phase could be observed inside of the crack. A SEM image with large FOV = 96 μm of the crack in the short circuited LLZO pellet is visible in Figure 10 a). The approximate position is indicated by the red arrow in Figure 9. Li whiskers growing in the crack (red box in Figure 10 a) are demonstrated from two perspectives: side view (b) and top view (c). The presence of Li whiskers is highlighted by white dashed circles. A second rather bulky Li morphology is indicated by white arrows in b, c, and d. Figure 10 d) shows a region on the edge of the crack where again whiskers are visible, but more interestingly a pore ($\sim 10 \mu\text{m}$) which is filled by Li-rich material and looks like it would start growing a whisker dendrite (small, dashed circle). e) shows a Li map of the region indicated by the green box in d), proving that the whiskers as well as the bulky dendrites are Li-rich. The whiskers have an approximate height of 7 μm and individual filaments have a diameter $< 0.3 \mu\text{m}$, even though this is difficult to evaluate as bundles of filaments have formed.

In conclusion, we were able to observe three different Li-dendrites morphologies within the same sample.

1. Intergranular (and/or grain boundary) Li accumulations as observed in Figure 8 in high density regions.
2. Thin whiskers growing out of grain boundaries in cracks.
3. Bulky Li-accumulations in pores and cracks.

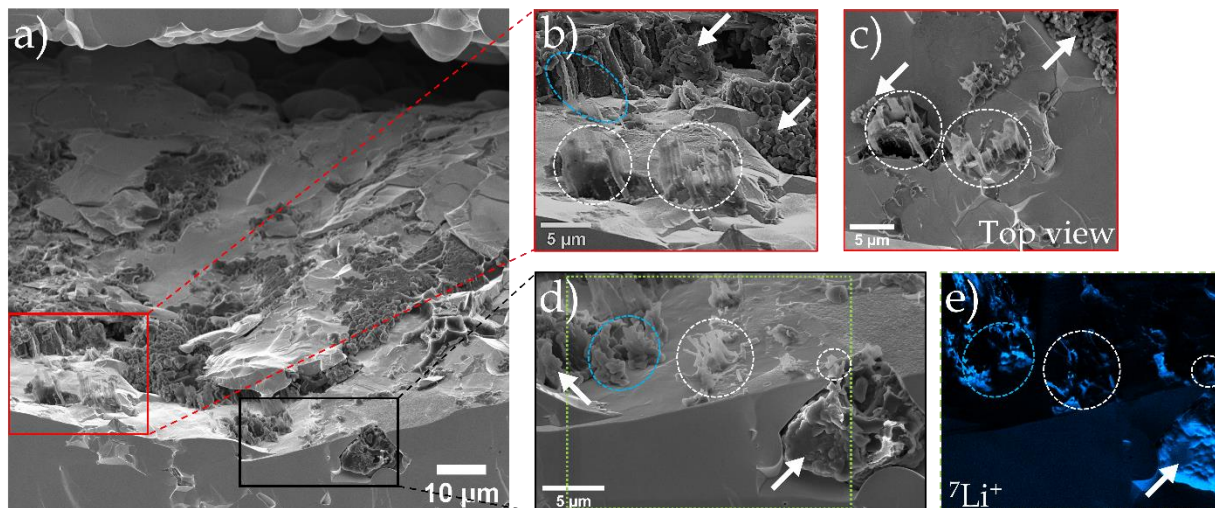


Figure 10: a) SEM image with large FOV = 96 μm of the crack in the short circuited LLZO pellet. The approximate position is indicated by the red arrow in Figure 9. b) (side view) and c) (top view) show a zoom-in of the region indicated by the red box in a). These images reveal the presence of whisker like dendrites (white dashed circles) and a bulky morphology (white arrows). d) shows a region on the edge of the crack where again whiskers are visible, but more interestingly a pore ($\sim 10 \mu\text{m}$) which is filled by Li-rich material. e) shows a Li map of the region indicated by the green box in d).

We believe that the three different dendrite morphologies that could be observed in Figure 10 are all connected by one or multiple phenomena and that different factors like local electrolyte density and length of the whiskers could play a crucial role. In Chapter 1 under “1.2.3. Types of Li-accumulations in LLZO based batteries” different morphologies which have been observed and studied in literature are discussed.

In the next section, we are going to discuss the observed Li-accumulation types and we are going to propose a hypothesis which could explain the co-existence of different types (whiskers, mossy, and intergranular/diffuse) which were observed in this chapter.

4.4.5. Proposed Hypothesis

For the following hypothesis we assume:

- 1) That Li-accumulations (dendrites) nucleate on the anode–electrolyte interphase, as indicated by the neutron radiography experiment.
- 2) That metallic Li (including accumulations & dendrites) is the only electronic conducting phase, i.e. we exclude the formation of other electronic conducting phases.

Consequently, the only possible regions for Li-ions to get neutralized to metallic Li is, either on the anode/electrolyte interface (nucleation) or on an already nucleated Li

accumulation (growth). As the kinetics of the growth is faster than that of nucleation⁹, growth is preferred over nucleation. Hence based on the two former assumptions, we believe, that only a few nucleation hotspots emerge on the anode/electrolyte interface (supported by the neutron radiography) which keep on growing to a 3D percolation network of intergranular Li-accumulations (see Figure 11 a). From a 2D point of view, the full connectivity of the 3D network is not visible, hence we only see partly connected Li-accumulations (Schematic: Figure 11 a; Experiments: Chapter 2 & 3). Based on our assumptions, Li ions can only be neutralized on interconnected branches of the 3D structure as electrons are required for the neutralization. The presence of a 3D percolation network is supported by various examples in this work (Figure 8, 10 & 13; see also Chapter 2 & 3) as well as in literature e.g. (10-15). While this might be the case for high density regions of the LLZO phase, porous regions might trigger a different growing mechanism.

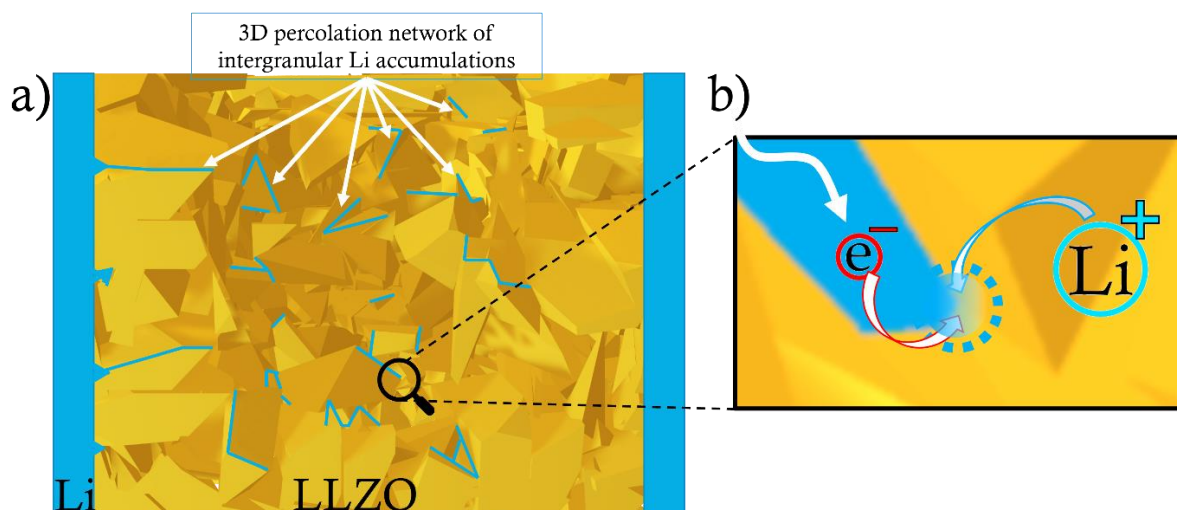


Figure 11: Schematics of a) a Li/LLZO/Li half cell (Li=cyan; LLZO=yellow) with 3D percolation network of intergranular Li accumulations; b) the neutralization of Li^+ showing that e^- can only be provided by an electronic conducting phase (e.g. Li dendrites).

Figure 12 a-f shows schematics (and SEM images) explaining the hypothesized growth of two different morphologies (in porous regions) observed in the post-mortem analysis (Figure 10). Those morphologies are whiskers with a length of $\sim 7 \mu\text{m}$ and a diameter of $< 0.3 \mu\text{m}$ (Figure 10 b, c, d). The second dendrite type is bulky and mossy ($> 10 \mu\text{m}$) as indicated by the white arrows in Figure 10 b, c, d. In Figure 12 the white phase represents the LLZO matrix and the black lines the grain boundaries, the grey shape is representative for a pore/void and the red structure represents a growing Li-accumulation. The yellow arrows represent the tendency of growth of the Li-accumulations at different stages.

Figure 10 provides hints for this hypothesized evolution, by looking at the small white dashed circle in Figure 10 d, we see very small whiskers ($1-2 \mu\text{m}$), representing the initial phase of whiskers growing (Figure 12 a). The large dashed white circles in Figure

10 b & d show whiskers which grew already much larger $\sim 7 \mu\text{m}$ and some of them seem to fuse together (Figure 10 b, c dashed blue circles & Figure 12 c). The regions highlighted by the blue dashed circles show bulky Li-accumulations which seem to result from whiskers growing and fusing together and/or entangling as they grow (schematically represented by Figure 12 d). Ultimately, we can see large chunky Li-accumulations (Figure 10 b, c, d) which have the same appearance as the Li-accumulations in the pore (Figure 10 d, e).

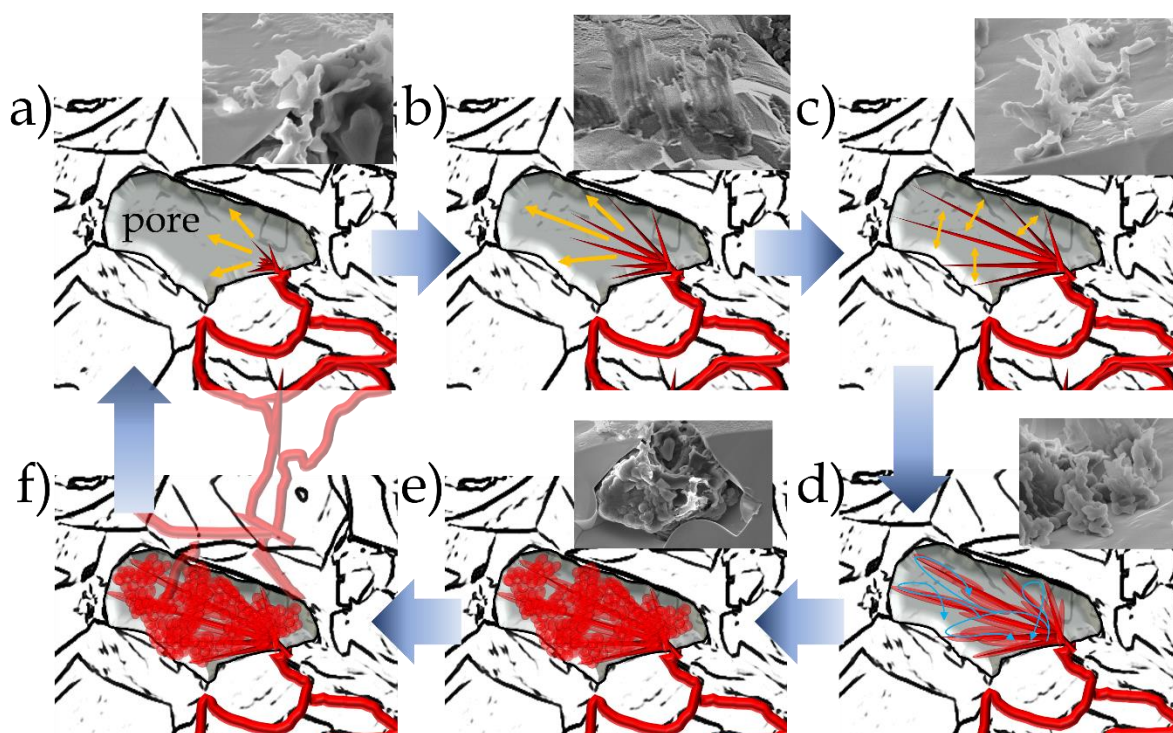


Figure 12: Schematic representation explaining step by step the formation and co-existence of two morphologies of Li-accumulations during battery cycling (with SEM images from Figure 10). The white phase represents the LLZO matrix and the black lines the grain boundaries, the grey shape is representative for a pore/void and the red line represents a growing Li-accumulation. The yellow arrows represent the tendency of growth of the Li-accumulations at different stages. a) Li-accumulation growing from dense LLZO into a pore/void & initial growth of whiskers. b) continuous growth of whiskers along their preferential growing orientation. c) Whiskers grew until they reach the walls of the pore, either their growth along a different axis and they grow thick or d) they continue growing in the same direction but start entangling (blue arrows); or both scenarios could happen simultaneously. e) Pore filled with “mossy” Li-accumulations. f) Li-accumulation starts to grow beyond the pore.

Figure 12 schematically describes what we can observe in Figure 10 and proposes a simplified mechanism for the growth of Li-accumulation inside low-density regions of LLZO e.g. large pores/voids, cracks. However, further studies are needed to validate this hypothesis, such as characterization with additional techniques and numerical simulations on growth rates and directions.

For high density ($>97\%$) regions within the LLZO pellet, based on experimental data and many post-mortem observations, Li tends to diffuse along grain boundaries and small intergranular cavities as described by Frenck et al.¹² as “cracks”. Such examples

can be found in Chapter 2, 3 and in this chapter in Figure 10. The fact that the Li-accumulations observed by Cheng et al.¹¹ look different, results from the fact, that they exposed the post-mortem LLZO-pellet to ambient air, while introducing the sample into the microscope. We performed an experiment to test how the Li-accumulations would be altered after air exposure and could prove that the difference of morphology between Cheng et al. and our observations are indeed related to air exposure (Figure 13). Yet, both cases represent the same type of Li-accumulation. The observed morphological difference probably goes beyond surface oxidation, however further investigation would be required to study the exact composition of the Li-accumulations after air exposure.

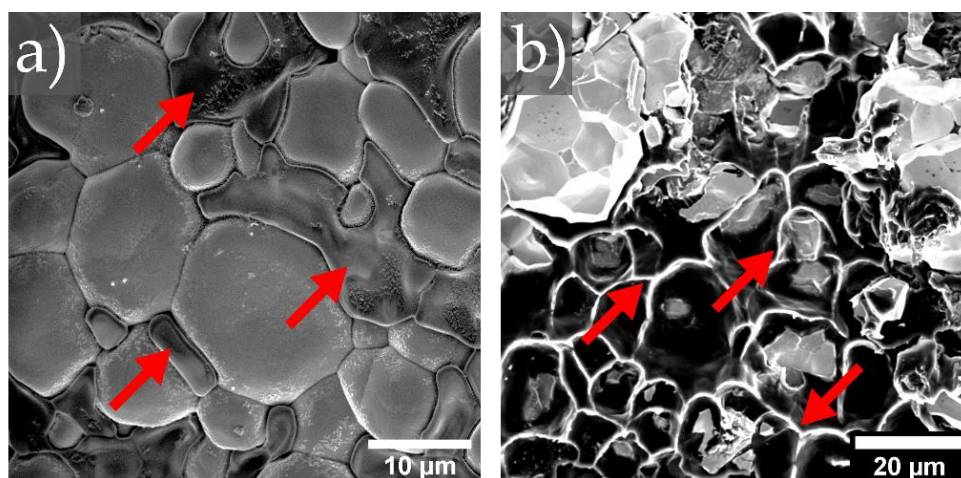


Figure 13: SEM images of post-mortem LLZO samples which have been produced and cycled under similar conditions. a) was kept constantly under controlled atmosphere (Argon or vacuum) and b) was exposed to ambient air after short-circuiting. The difference between both morphologies results from Li oxidation at air exposure. The red arrows highlight the Li accumulations in both cases.

4.4.6. Limitations

Given that our findings are based on a limited number of analysed samples, interpretations should be treated with caution. Blondeau et al.¹⁶ for instance discusses the reliability of *operando* measurements in rechargeable batteries during *operando* synchrotron X-ray radiation. In summary they demonstrated that the interaction between synchrotron X-rays and the cells not only modified the electrode but also entirely invalidated the electrode processes right from the initial cycles. This shows that utmost caution must be taken when performing and interpreting *operando* experiments. Beam-related (neutrons as well as ions) artefacts might occur, which have not been studied neither considered in this study, thus we don't know yet if their effect is significant or negligible. Like synchrotron X-rays, neutron irradiation could alter or influence electrochemical processes or induce parasitic cross-reactions or both. The structural effect of ion irradiation can be studied by simulations (SRIM¹⁷ like in ⁴) and additional TEM, AFM or LCSM. Another factor which needs to be taken into

account is that Ga-ions can alter electrochemical properties of LLZO, hence the Ga dose and implantation needs to be monitored during the SIMS experiment and considered when interpreting electrochemical data.¹⁸

In summary we can say that future of battery research inevitably relies on advanced *operando* workflows and considerable progress has been made recently, however most of these approaches are still in an early phase and complex phenomena like the influence of the analysis on the cycling and vice versa needs more attention in order to design reliable *operando* experiments.

4.5 Conclusion

In this chapter we presented an *operando* neutron imaging approach, to study Li penetration during electrochemical cycling of a Li/LLZO/Li half-cell.

In the beginning the requirements and restrictions for a successful experiment are discussed, followed by a detailed description of the sample-holder design (Figure 1) as well as the final experimental design (Figure 2). Subsequently, sample preparations for the *operando* neutron experiment as well as for the post-mortem SEM/SIMS analysis are described.

The following section discusses the results, and the Li/LLZO/Li sample was cycled during 26 h with six different current density settings until short-circuit failure (Figure 4). The voltage profile as well as the difference of neutron attenuation observed on the Li/LLZO interface were discussed. Based on the $\Delta O.D.$ and equation (1.1) & (1.2) we could calculate localized vol.-% of the Li-accumulations growing during cell operation. Li dendrite volume in selected regions grew up to 3.6 % (Figure 7).

Subsequently, structural and chemical analysis via correlative SEM/SIMS was performed and the results revealed different morphologies of Li accumulations. Dense LLZO regions elucidated a “diffusing” behaviour of Li accumulation (Figure 8), on the other hand, low-density regions in the LLZO pellet (pores, cracks, ...) show different types of Li accumulations (Figure 10).

The neutron analysis elucidated an increase of the Li dendrite volume in selected regions up to 3.6%. The selected areas, which showed substantial OD fluctuations were mainly on the LLZO/Li interface, however, SEM/SIMS analysis clearly proved the presence of Li dendrites in the bulk of LLZO, too. This contradiction in the data is probably due to the fact that the spatial resolution of the neutron tomography is in the tens of μm -range, while SEM/SIMS imaging presents a spatial resolution which is almost three order of magnitude smaller (nm-range). The SEM/SIMS analysis could prove that the short-circuit caused during cc cycling of the symmetric cell, is a

consequence of Li-dendrite growth through the solid electrolyte. Unfortunately, neutron tomography can't detect individual Li dendrites grow, as their dimensions are below the resolution of the technique.

A system to categorize Li accumulation types as well as a hypothesis (4.4.5. Proposed Hypothesis) of the creation and co-existence of the observed Li accumulation types is proposed.

From this chapter we can draw the following conclusions:

- Successful concept and design of an *operando* neutron imaging sample-holder.
- Introduction of a new *operando* methodology via neutron imaging, combined with post-mortem correlative SEM/SIMS analysis. The neutron imaging experiment intends to observe and follow Li growth through the solid electrolyte and enables quantitative analysis of Li.
- Li quantification revealed localized Li dendrite volume, which grew during cycling, between 1.8 - 3.6 %.
- Correlative SEM/SIMS analysis enables structural and chemical analysis of the post-mortem sample. Observation of three different Li accumulation types, which have been described and a hypothesis has been expressed, explaining the creation and co-existence of the different types.

ANNEXE 3

A 2nd experiment was carried out to insure reproducibility and reliability of our custom-designed experimental set-up. The neutron experiment was performed at the PSI in Villigen, Switzerland from 8th to 9th December. A proposal (attached here in ANNEXE 3) for 72 h beamtime was submitted, “only” 48 h beamtime got accepted. Initial test measurement (tomo- & radiography + *operando*) were performed (Figure 14 a) with 5 different current density settings: 5, 10, 20, 40, and 80 $\mu\text{A}/\text{cm}^2$. The 5, 10 and 20 $\mu\text{A}/\text{cm}^2$ underwent 4 cycles for each, followed by 1 cycle with 40 $\mu\text{A}/\text{cm}^2$ and one cycle with 80 $\mu\text{A}/\text{cm}^2$. As it is recognisable, that the post-mortem analysis via SEM/SIMS show similar Li accumulations, this experiment clearly strengthens the former experiment and supports the conclusions. However, the Li accumulations were too small in order to detect fluctuations of the OD beyond noise.

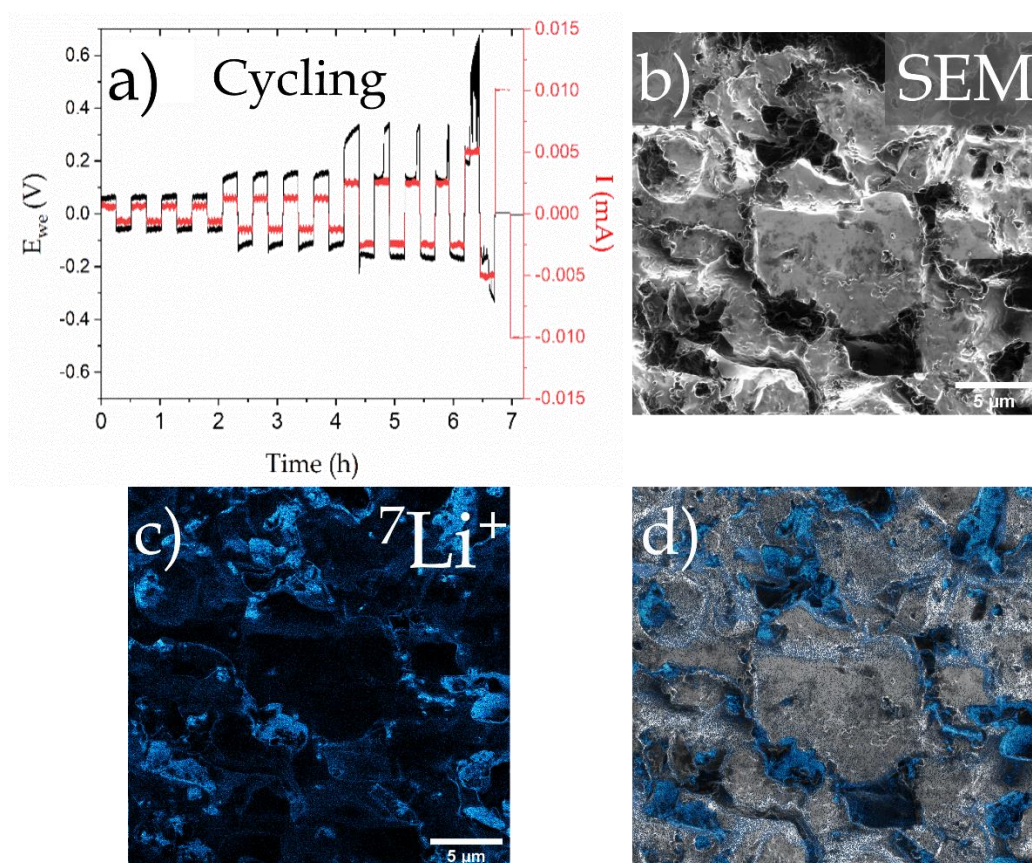


Figure 13: Second operando neutron imaging experiment. a) Voltage profile of the operando experiment performed with 4 different current density settings: 5, 10, 20, 40, and 80 $\mu\text{A}/\text{cm}^2$. The 5, 10 and 20 $\mu\text{A}/\text{cm}^2$ underwent 4 cycles for each, followed by 1 cycle with 40 $\mu\text{A}/\text{cm}^2$ and one cycle with 80 $\mu\text{A}/\text{cm}^2$. b) Post-mortem SEM image of the bulk of LLZO, elucidating Li accumulations. c) Li chemical map of the same region of interest as b), highlighting the presence of Li accumulations. d) Combined SEM and SIMS image.

Proposal for beam time at PSI-ICON:

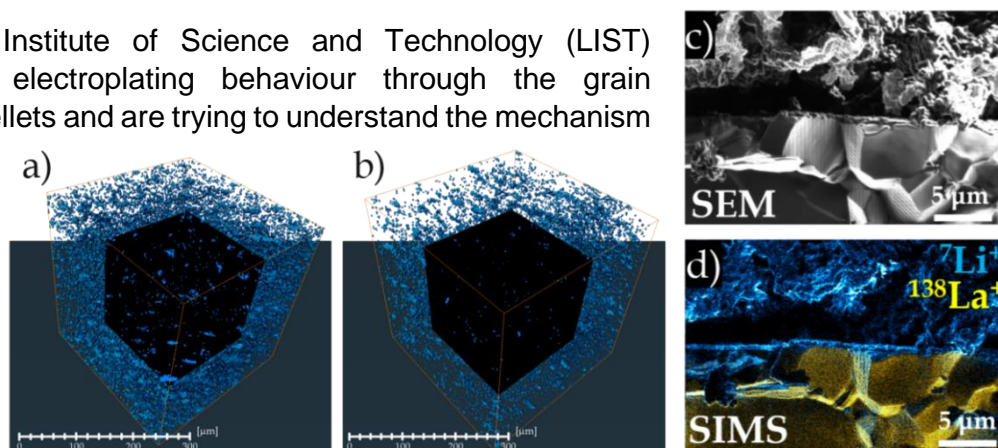
In Operando neutron imaging of lithium depositions inside of garnet type solid electrolytes

Luca Cressa¹, Tom Wirtz¹, Santhana Eswara¹

¹ Advanced Instrumentation for Nano-Analytics (AINA), Luxembourg Institute of Science and Technology, 41 rue du Brill, L-4422, Belvaux, Luxembourg

Introduction: Solid-state electrolytes (SSE) are attracting considerable interest in the field of battery research. The replacement of the liquid electrolyte with a SSE, which may act as both the separator and the electrolyte, targets an improvement of future battery's design and reliability. Unfortunately, in most cases SSE display low ionic conductivities compared to that of liquid electrolytes, however one prominent candidate among the related lithium garnets namely $\text{Li}_7\text{La}_3\text{Zr}_2\text{O}_{12}$ (LLZO) could overcome this challenge. Its good Li^+ conductivity of $\sim 10^{-4}$ S cm^{-1} at room temperature compared to most other SSE as well as its excellent stability with metallic lithium makes LLZO very appropriate for an application in rechargeable solid-state batteries (SSB). Initially it was thought that by assembling SSB, the issue of Li dendrite formation would be solved due to the high shear modulus ($\sim 5 \times 10^{10}$ Pa) of oxides. However, literature reports several cases where failures of SSB have been observed due to Li protrusions growing through grain boundaries and consequently short-circuiting the battery.

We at Luxembourg Institute of Science and Technology (LIST) observed similar Li electroplating behaviour through the grain boundaries of LLZO pellets and are trying to understand the mechanism of these parasitic reactions which occur during cycling and limit the lifetime of SSB. We designed an *In-Operando* SEM/SIMS set up at LIST allowing to structurally and chemically image battery samples under operational conditions.



Advantages of this methodology are nanoscale lateral resolution, the possibility to detect low-Z elements and isotopes, and good surface sensitivity. However, one major disadvantage is that we can't analyse bulk material without removing material, for this a non-destructive analysis is needed.

By analysing battery samples with neutron imaging, being a non-destructive method, we create complementary data sets pushing *In-Operando* analysis of batteries beyond the state-of-the-art.

Preliminary results from own work: Pre- and post-mortem LLZO pellet have been analysed by X-ray computer tomography (XCT) and revealed a difference in the porosity fraction of about 1.8 % (as prepared 2.85 % & post-mortem 1.06 %) as shown in Fig. 1. We believe that this difference is caused by the penetrating Li which grows through the grain boundaries until it reaches the cathode and consequently short-circuits the system.

Objectives of the proposed experiments: 1. *In-Operando* neutron imaging of Li electrodeposition.

2. Correlate the outcoming data with SEM/SIMS data, thus taking advantage of the complementarity of both techniques.

3. Creating a methodological protocol for advanced *In-Operando* multimodal analysis and characterization of battery materials.

Methodology: For the proposed experiment, batteries with a Li anode and a SSE, namely LLZO will be assembled. The cathode material will be chosen accordingly to not interfere with neutron imaging. It is planned to design an *In-Operando* experiment, meaning that the battery sample is meant to be analysed under operational conditions (Fig. 2). The electrochemical charging and discharging will be performed with a Biologic SP-150 potentiostat which we use on a regular basis to perform *In-Operando* correlative SEM/SIMS analysis. To keep the battery sample free from contaminations it will be sealed under inert gas in a pouch bag with connections for the electrodes.

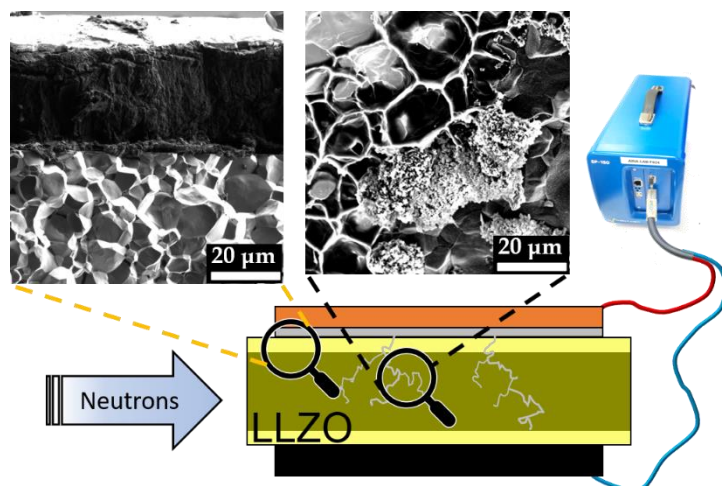


Figure 15: Schematic setup of the *In-Operando* neutron imaging experiment. The SEM images show (left) Li/LLZO interface and (right) Li-depositions which grow through the grain boundaries of LLZO

Risk analysis: As Li gives a high contrast in neutron imaging and as the composition of the SSE also contains Li, initially it was unclear if the contrast difference between “LLZO lithium” and “dendrite lithium” would be sufficient to achieve the purpose of the experiment. Figure 3 shows the attenuation coefficient as a function of the neutron energy. The computational data reveals that for a neutron energy of 10^{-3} eV the attenuation of Li in LLZO is around 9 cm^{-1} and for Li dendrites (with a volume fraction of 0-3%) the attenuation fraction is above 10 cm^{-1} . This means that LLZO will make a significant attenuation and that dendrites with a volume fraction between 0% and 3% will have a visible contribution.

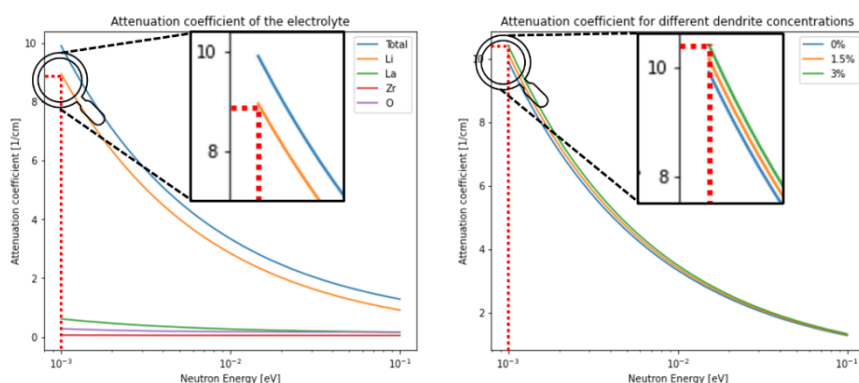


Figure 16: Computed attenuation for LLZO and Li-dendrites. Thanks to Dr. P. Boillat for the computation.

Individual dendritic structures will probably not be visible, however larger accumulations (e.g. Li matrix forming through grain boundaries) should be detectable ensuring a successful observation of

Li depositions within the achievable resolution. Further computational results indicate that the contrast would not be very high (0.5% difference in transmission per % of dendrite concentration), however it should be adequate for the purpose of the experiment.

CHAPTER 4

Expected Impact, dissemination, joint articles: We hope that with 3 days beam time on the ICON within your facility, we could during an *In-Operando* experiment study how those parasitic Li depositions are penetrating through LLZO, by that we can overcome the limits of SIMS being a purely surface sensitive technique. Additionally, we will push the limits of *In-Operando* analysis by correlating *In-Operando* neutron imaging¹⁹ with *In-Operando* SEM/SIMS²⁰. A joint article will probably result from the outcoming data, some results may become part of conference talks.

References

- (1) Kaestner, A. P.; Hartmann, S.; Kühne, G.; Frei, G.; Grünzweig, C.; Josic, L.; Schmid, F.; Lehmann, E. H. *The ICON beamline – A facility for cold neutron imaging at SINQ. Nuclear Instruments and Methods in Physics Research Section A: Accelerators, Spectrometers, Detectors and Associated Equipment* **2011**, *659*, 387–393.
- (2) Boillat, P.; Carminati, C.; Schmid, F.; Grünzweig, C.; Hovind, J.; Kaestner, A.; Mannes, D.; Morgano, M.; Siegwart, M.; Trtik, P.; Vontobel, P.; Lehmann, E. H. *Chasing quantitative biases in neutron imaging with scintillator-camera detectors: a practical method with black body grids. Opt Express* **2018**, *26*, 15769–15784.
- (3) Kaestner, A. P. *MuhRec—A new tomography reconstructor. Nuclear Instruments and Methods in Physics Research Section A: Accelerators, Spectrometers, Detectors and Associated Equipment* **2011**, *651*, 156–160.
- (4) Cressa, L.; Sun, Y.; Andersen, D.; Gerard, M.; Castro, O. de; Kopljar, D.; Nojabae, M.; Friedrich, K. A.; Schmitz, G.; Wirtz, T.; Eswara, S. *Toward Operando Structural, Chemical, and Electrochemical Analyses of Solid-State Batteries Using Correlative Secondary Ion Mass Spectrometry Imaging. Anal Chem* **2023**, *95*, 9932–9939.
- (5) Audinot, J.-N.; Philipp, P.; Castro, O. de; Biesemeier, A.; Hoang, Q. H.; Wirtz, T. *Highest resolution chemical imaging based on secondary ion mass spectrometry performed on the helium ion microscope. Rep Prog Phys* **2021**, *84*.
- (6) Castro, O. de; Audinot, J.-N.; Hoang, H. Q.; Coulbary, C.; Bouton, O.; Barrahma, R.; Ost, A.; Stoffels, C.; Jiao, C.; Dutka, M.; Geryk, M.; Wirtz, T. *Magnetic Sector Secondary Ion Mass Spectrometry on FIB-SEM Instruments for Nanoscale Chemical Imaging. Anal Chem* **2022**, *94*, 10754–10763.
- (7) Schindelin, J.; Arganda-Carreras, I.; Frise, E.; Kaynig, V.; Longair, M.; Pietzsch, T.; Preibisch, S.; Rueden, C.; Saalfeld, S.; Schmid, B.; Tinevez, J.-Y.; White, D. J.; Hartenstein, V.; Eliceiri, K.; Tomancak, P.; Cardona, A. *Fiji: an open-source platform for biological-image analysis. Nat Methods* **2012**, *9*, 676–682.
- (8) Panakkal, J. P.; Ghosh, J. K.; Roy, P. R. *Analysis of optical density data generated from neutron radiographs of uranium-plutonium mixed oxide fuel pellets inside sealed nuclear fuel pins. Nuclear Instruments and Methods in Physics Research Section B: Beam Interactions with Materials and Atoms* **1986**, *14*, 310–313.
- (9) Wood, K. N.; Kazyak, E.; Chadwick, A. F.; Chen, K.-H.; Zhang, J.-G.; Thornton, K.; Dasgupta, N. P. *Dendrites and Pits: Untangling the Complex Behavior of Lithium Metal Anodes through Operando Video Microscopy. ACS Cent Sci* **2016**, *2*, 790–801.
- (10) Aguesse, F.; Manalastas, W.; Buannic, L.; Del Lopez Amo, J. M.; Singh, G.; Llordés, A.; Kilner, J. *Investigating the Dendritic Growth during Full Cell Cycling of Garnet Electrolyte in Direct Contact with Li Metal. ACS Appl Mater Interfaces* **2017**, *9*, 3808–3816.
- (11) Cheng, E. J.; Sharafi, A.; Sakamoto, J. *Intergranular Li metal propagation through polycrystalline Li₆.₂₅Al_{0.25}La₃Zr₂O₁₂ ceramic electrolyte. Electrochimica Acta* **2017**, *223*, 85–91.
- (12) Frenck, L.; Sethi, G. K.; Maslyn, J. A.; Balsara, N. P. *Factors That Control the Formation of Dendrites and Other Morphologies on Lithium Metal Anodes. Front. Energy Res.* **2019**, *7*.
- (13) Golozar, M.; Paoletta, A.; Demers, H.; Savoie, S.; Girard, G.; Delaporte, N.; Gauvin, R.; Guerfi, A.; Lorrmann, H.; Zaghbi, K. *Direct observation of lithium metal dendrites with ceramic solid electrolyte. Sci Rep* **2020**, *10*, 18410.
- (14) Ren, Y.; Shen, Y.; Lin, Y.; Nan, C.-W. *Direct observation of lithium dendrites inside garnet-type lithium-ion solid electrolyte. Electrochemistry Communications* **2015**, *57*, 27–30.

- (15) Shen, F.; Dixit, M. B.; Xiao, X.; Hatzell, K. B. *Effect of Pore Connectivity on Li Dendrite Propagation within LLZO Electrolytes Observed with Synchrotron X-ray Tomography*. *ACS Energy Lett.* **2018**, *3*, 1056–1061.
- (16) Blondeau, L.; Surblé, S.; Foy, E.; Khodja, H.; Belin, S.; Gauthier, M. *Are Operando Measurements of Rechargeable Batteries Always Reliable? An Example of Beam Effect with a Mg Battery*. *Anal Chem* **2022**, *94*, 9683–9689.
- (17) Ziegler, J. F.; Ziegler, M. D.; Biersack, J. P. *SRIM – The stopping and range of ions in matter (2010)*. *Nuclear Instruments and Methods in Physics Research Section B: Beam Interactions with Materials and Atoms* **2010**, *268*, 1818–1823.
- (18) Jalem, R.; Rushton, M.; Manalastas, W.; Nakayama, M.; Kasuga, T.; Kilner, J. A.; Grimes, R. W. *Effects of Gallium Doping in Garnet-Type $\text{Li}_7\text{La}_3\text{Zr}_2\text{O}_{12}$ Solid Electrolytes*. *Chem. Mater.* **2015**, *27*, 2821–2831.
- (19) Song, B.; Dhiman, I.; Carothers, J. C.; Veith, G. M.; Liu, J.; Bilheux, H. Z.; Huq, A. *Dynamic Lithium Distribution upon Dendrite Growth and Shorting Revealed by Operando Neutron Imaging*. *ACS Energy Lett.* **2019**, *4*, 2402–2408.
- (20) Yamagishi, Y.; Morita, H.; Nomura, Y.; Igaki, E. *Visualizing Lithiation of Graphite Composite Anodes in All-Solid-State Batteries Using Operando Time-of-Flight Secondary Ion Mass Spectrometry*. *J Phys Chem Lett* **2021**, *12*, 4623–4627.

CHAPTER 5

1. CHAPTER 1 Background
2. CHAPTER 2 Correlative SEM/SIMS
3. CHAPTER 3 X-ray Based Correlative Approaches
4. CHAPTER 4 *Operando* Neutron Imaging
5. CHAPTER 5 Summary & Outlook
 - 5.1. Summary
 - 5.1.1. Correlative Microscopy
 - 5.1.2. *Operando*
 - 5.1.3. Impact
 - 5.2. Outlook
 - 5.2.1. Today's Limitations
 - 5.2.2. On-going work
 - 5.2.3. Future Work

5.1. Summary

Facing the climate crises, equipped with many immature battery technologies which could become the next generation energy storage systems by replacing classic Li ion batteries, we find ourselves in front of one major challenge: How can we improve battery analysis and characterization and by that accelerate battery research?

5.1.1. Correlative Microscopy

In Chapter 1 we explained the importance of correlative microscopy and spectroscopy, allowing to acquire complementary structural, physical and chemical data. In this chapter we will summarise and discuss performed, as well as potential future, correlative workflows.

Three further techniques (X-ray photoelectron spectroscopy (XPS), depth profiling, & laser confocal scanning microscopy (LCSM)) have been included in the summaries (Figure 1, Table 1, Table, & Table), as they were used within the practical part of this thesis, but were not explicitly discussed in this manuscript, as this is still preliminary results. Depth profiling was performed via SIMS and via XPS, and as it adds an additional dimension to the outcoming data, we included it as independent technique.

As intensively reported in this study, we overcame the issues mentioned in Chapter 1 (“Problem Statement” & “Thesis Objectives”) by designing new correlative ways to analyse batteries. With our approaches, we tried to combine as many techniques as needed to tackle certain questions. Thirteen different analysis techniques (4 structural, 3 crystallographic, 4 quantitative, and 2 qualitative) were adapted to perform advanced analysis.

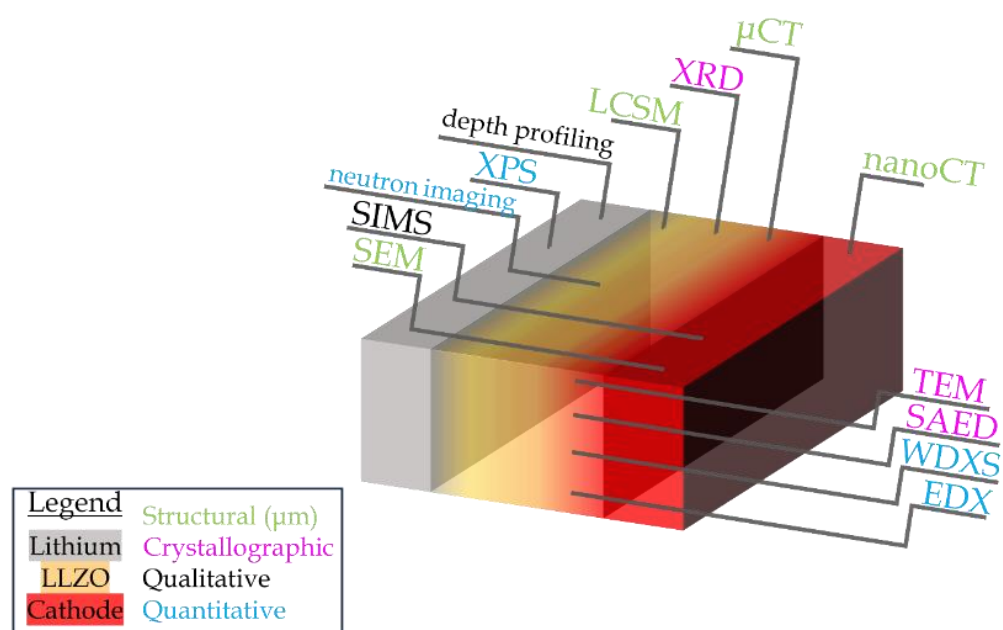


Figure 1: Schematics of all analysis techniques performed within this thesis. The sample is visualized by three phases: grey = Lithium, yellow = LLZO, and red = cathode. While SEM and SIMS have been performed on all parts of a solid-state batteries (anode, solid electrolyte, and cathode), other techniques have only been used on two or one phase. This schematic only shows

which techniques have been used but does not reveal any information on which techniques were directly correlated (see Table 1).

Figure 1 shows a schematic of all analysis techniques performed within this thesis. While SEM and SIMS have been performed on all parts of a solid-state batteries, other techniques have only been used on one or two phases. Like for example neutron imaging was performed on a Li/LLZO/Li half-cell visualized by the line touching Li & LLZO in the schematics. TEM, SAED, EDX, and WDXS have only be performed on the cathode, on LLZO, and on their interface as illustrated in the schematics. XPS and SIMS depth profiling was performed on the Li anode; LCSM, XRD, and μ CT on LLZO; and nanoCT was only performed on the cathodic side.

Table 1: Matrix showing which techniques have been used in correlative approaches. The number in the first row represent the same technique as designated in the first column. Green = correlative. Red = non-correlative. (n^0 im. = neutron imaging)

		1	2	3	4	5	6	7	8	9	10	11	12
1	SEM												
2	LCSM	Green											
3	μ CT	Green	Red										
4	nanoCT	Green	Red	Red									
5	XRD	Green	Red	Red	Red								
6	TEM	Green	Red	Red	Red	Red							
7	SAED	Green	Red	Red	Red	Red	Green						
8	SIMS	Green	Green	Green	Green	Green	Green	Green					
9	XPS	Green	Red	Red	Red	Red	Red	Red	Green				
10	EDX	Green	Green	Green	Green	Red	Green	Green	Green	Red			
11	WDXS	Green	Red	Red	Red	Red	Green	Green	Green	Red	Green		
12	n^0 im.	Green	Red	Red	Red	Red	Red	Red	Green	Red	Red	Red	

In addition to Figure 1, Table 1 shows in a matrix which techniques have been correlatively used. For instance, we see that SEM and SIMS have been correlatively used with every other technique. A few unprecedented correlative analyses were performed, however out of 66 bilateral correlative combinations, only 30 have been adapted within this thesis. This clearly shows that there is still a huge potential for new correlative approaches. The correlation of the techniques should always be adapted to the kind of information which is needed to tackle a certain question.

Table 2 on the other hand summarizes which techniques have been used to study the different parts of SSBs (Li anode, solid electrolyte, cathode). Two additional columns “/” represent the interphase between cathode/SE and anode/SE respectively.

With a few correlative approaches, we were able to push the limits of the analysis of solid-state batteries. However, as mentioned in Chapter 1 (under “1.3.4. Advanced Analysis”), meanwhile it is not enough to simply correlate two techniques and, to go truly beyond state-of-the-art, “Ideal Options” (Table 3 in Chapter 1) should be

included. One of the so-called ideal options is the inclusion of *in-situ* and/or *operando* capabilities. In the next section we will briefly summarise and discuss the *operando* workflows which have been extensively described in Chapter 2 & 4. While some techniques (SEM & SIMS) have been used on all components. Other techniques we used to analyse a single component e.g. nanoCT, LCSM and XPS. Table 2 is complementary to Figure 1 and Table 1.

Table 2: Matrix showing which of the parts of a SSB (A = anode, SSE = solid-state electrolyte, C = cathode) were analysed with which techniques in the framework of this thesis. The “/”-columns represent the analysis of interface regions between A & SSE and between SSE & C.

	Technique	A	/	SSE	/	C
1	SEM					
2	LCSM					
3	μ CT					
4	nanoCT					
5	XRD					
6	TEM					
7	SAED					
8	SIMS					
9	Depth pro.					
10	XPS					
11	EDX					
12	WDXS					
13	Neutron im.					

5.1.2. *Operando*

As the availability of advanced analysis techniques is limited, we had no other option than to design our own workflow, experimental configuration and sample holder for *operando* capabilities. The correlative *operando* SEM/SIMS approach described in Chapter 2 is a very versatile and adaptable system which can be used to study a multitude of different battery samples. The system can also be used for analysis beyond solid-state batteries, e.g. gel batteries, piezoelectric materials, solar cells, ... Additionally the functions that the pressure on the sample can be regulated and that a multitude of electrochemical experiments (EIS, CV, cycling, resistance measurements, ...) can be performed in *operando* mode makes the sample holder and the entire workflow very attractive for research purposes.

This correlative *operando* approach allowed us to observe Li-accumulations during cycling and to structurally as well as chemically image the Li/LLZO/Li half-cell before and after cycling. By that we were able to directly obtain a correlation between the microstructure, chemical composition, and electrochemical performance.

On the other hand, we designed a second sample holder enabling *operando* neutron imaging (Chapter 4). This sample holder -other than the previous one- is not universal and is specifically designed for only one single experiment. The entire design,

dimensions and materials of the sample holder were carefully chosen in order to enable a successful *operando* neutron imaging experiment.

Both experiments showed the significant potential of correlative *operando* workflows opening doors for real-time, multi-dimensional data acquisition, by that being able to tackle many unanswered questions and hopefully accelerate battery research.

Table 3 summarizes which techniques can be used for surface and/or bulk analysis and, whether 2D and/or 3D data is recorded (green=yes; red=no; yellow=only in combination with a FIB; white=not defined). Additionally, the modes (e.g. ex-situ; in-situ; operando) which were used on the different techniques are indicated. The last two columns indicate the input and the output signals among the 13 used technique.

Table 3: Matrix showing which of the used techniques are surface & bulk sensitive, which techniques delivers 2- &/or 3D data. The mode in which the techniques were used (Ex-/In-situ or Operando), and what is the nature of input & output signal of each technique.

	Technique	Surface	Bulk	2D	3D	Mode	Input	Output
1	SEM	Green	Yellow	Green	Yellow	Operando	e ⁻	e ⁻
2	LCSM	Green	Red	Green	Green	Ex-situ	Photon	Photon
3	μCT	Red	Green	Green	Green	Ex-situ	X-ray	X-ray
4	nanoCT	Red	Green	Green	Green	Ex/In-situ	X-ray	X-ray
5	XRD	Green	Red	White	White	Ex-situ	X-ray	X-ray
6	TEM	Red	Green	Green	Red	Ex-situ	e ⁻	e ⁻
7	SAED	Green	Green	White	White	Ex-situ	e ⁻	e ⁻
8	SIMS	Green	Yellow	Green	Yellow	In-situ	Ion	Ion
9	Depth pro.	Red	Green	Red	Green	In-situ	Ion / X-ray	Ion / e ⁻
10	XPS	Green	Yellow	Green	Yellow	Ex-situ	X-ray	e ⁻
11	EDX	Green	Red	Green	Red	Ex-situ	e ⁻	X-ray
12	WDXS	Green	Red	Green	Red	Ex-situ	e ⁻	X-ray
13	Neutron im.	Red	Green	Green	Green	Operando	n ⁰	n ⁰

5.1.3. Impact

Instrumentation

- In Chapter 2 we presented the design, and proof of concept of a correlative FIB-SEM-SIMS-based *operando* workflow with a Li/LLZO/Li solid state half-cell. With that we were able to push today's instrumental limitations toward an *operando* correlative SEM/SIMS approach. While now only SEM imaging is fully *operando* and SIMS operation is only *in-situ*, current work is focussing in enabling full *operando* capability of SIMS.
- In Chapter 3 we introduced a methodology that combines FIB-SEM, X-ray nanoCT, and SIMS techniques for comprehensive analysis of lithium batteries. This integration allows for precise ROI scoping and sample characterization, high resolution imaging, three-dimensional reconstructions, and chemical

composition analysis. The combination of nanoCT-SIMS, can be carried out on readily available FIB-SEM instruments, eliminating the need for specialized standalone equipment. This broadens the scope of research possibilities, allowing us to address longstanding questions that demand correlative analysis encompassing both structural and chemical investigations from the μm to nm scales.

- In Chapter 4, a successful concept and design of an *operando* neutron imaging sample-holder is demonstrated. The introduction of a new *operando* methodology via neutron imaging, combined with post-mortem correlative SEM/SIMS analysis, opens doors for structural and chemical analysis, and the quantification of dendritic Li.

Materials Science

- In Chapter 2 we were able to study Li dendrites, growing through LLZO during operation. After short-circuit, Li was detected and chemically mapped in cavities and intergranular regions, by that we could support other studies which stated Li accumulations without a direct detection of Li. In this study a correlation between the microstructure, the chemical composition, and the electrochemical performance is obtained directly.
- In Chapter 3 we discussed X-ray based correlative approaches, in very diverse ways to analyse all components of a solid-state battery. For example, μCT and SEM/SIMS were used to investigate the porosity of LLZO and to get an estimation about what vol.-% is occupied by Li accumulations in LLZO. We measured a porosity of $\sim 2.8\%$ of the pristine LLZO samples. Additionally, the volume occupied by dendrites is $\sim 55\%$ of the initial porosity fraction. This gives us a rough estimation of the extent of dendrite formation in dense ($>95\%$) LLZO based batteries.
- The correlative nanoCT-SIMS approach (Chapter 3) enabled to study degraded AM elucidating that Al, initially only present in the NCA phase, tends to accumulate in internal grain-boundaries of primary NCA particles and diffuses into the binder phase.
- In another study we correlated EDX, WDXS, SEM-SIMS *ex-situ* while studying the LLZO:Al,Ta/LCO interface. This work is discussed in detail in “Case Study 1” (Chapter 3). After additional analysis (TEM, SAED, & simulations) we could elucidate two major reasons for electrochemical performance loss: 1) interfacial

loss of crystallinity of LLZO and 2) electrochemical-driven Al diffusion. Within the study a thermal recovery treatment is proposed which could recover ~80% of the original performance. Additionally, a mechanism for the Al-redistribution during cycling and during sintering is presented.

This study focussing on the recovery of degraded batteries, can have an impact on real life challenges related to the climate crises like sustainability, circular economy and green energy, which emphasizes its significance.

- In Chapter 4 under *operando* neutron imaging, a symmetric cell was cycled until short-circuit failure. This revealed, a growth of Li dendrite volume fraction up to 3.6 % in selected regions. In a post-mortem SEM/SIMS analysis different dendrite types could be observed and analysed.

Having summarized all this, it becomes evident that advanced analysis is not only an attractive asset, but that it is necessary to adapt and upgrade common techniques and workflows for correlative and/or *operando* analysis for an accelerated development of next generation batteries.

Turning back to the initial “Problem Statement” & “Thesis Objectives” which were posed in Chapter 1, we can say with confidence, that we achieved the objectives and took a significant step forward in the right direction:

- i. By optimising workflows, adapt them to battery research and on the other hand leaving enough room for adaptation to study energy storage systems beyond Li-LLZO based batteries.
- ii. By using multiple techniques, to develop unprecedented correlative workflows.
- iii. We designed two major workflows using techniques for the detection of Li and by that being able to study nucleation and evolution of Li-dendrites. One workflow (Chapter 2) taking advantage of SIMS focusses on qualitative analysis and the neutron imaging, another workflow (Chapter 4) could add quantitative information to the detected Li.
- iv. We successfully implemented a fully *operando* SEM workflow, which has the capability to perform *in-situ* SIMS. Additionally, we designed and successfully executed an *operando* neutron imaging experiment.
- v. The use of high-sensitivity and high-resolution techniques (e.g. SIMS, WDXS, ...) enables generation of nm-scaled resolution with dopant-level sensitivity, which could be demonstrated in “Case Study 1” (Chapter 3)

5.2. Outlook

5.2.1. Today’s limitations

In Chapter 1 we mentioned challenges that prevent and slow down progress in battery research. One is the limited availability of advanced analysis techniques. As more and

more practical tools and workflows are reaching the market, the accessibility of advanced techniques will increase, hence more researchers will have the opportunity to perform advanced analysis.

While handling Li and other battery components, is in many cases still demanding due to air and moisture sensitivity, it does not pose a major limitation any more.

A more complex challenge, however, is the interference between battery operation and simultaneous analysis. To this day, we do not exactly know how large these effects are, some researchers were able to observe interferences, and could point out how complex interpretations can become when operation and analysis are not fully decoupled. This aspect is crucial for the future of *operando* workflows and still needs more attention and research.

5.2.2. On-going work

The following two studies are part of ongoing work which will be published soon:

- 1) Preliminary studies were performed on solid-state polymer battery systems, where we especially took advantage of the mm- to nm-capability of SEM to image the entire cell but also individual dendrites (Figure 2). A few illustrative SEM images are shown in Figure 2. Those preliminary results promise further interesting correlative investigations on polymeric materials, where SEM could be combined with other methods, which were used and discussed in this work.

1) Entire cell imaging

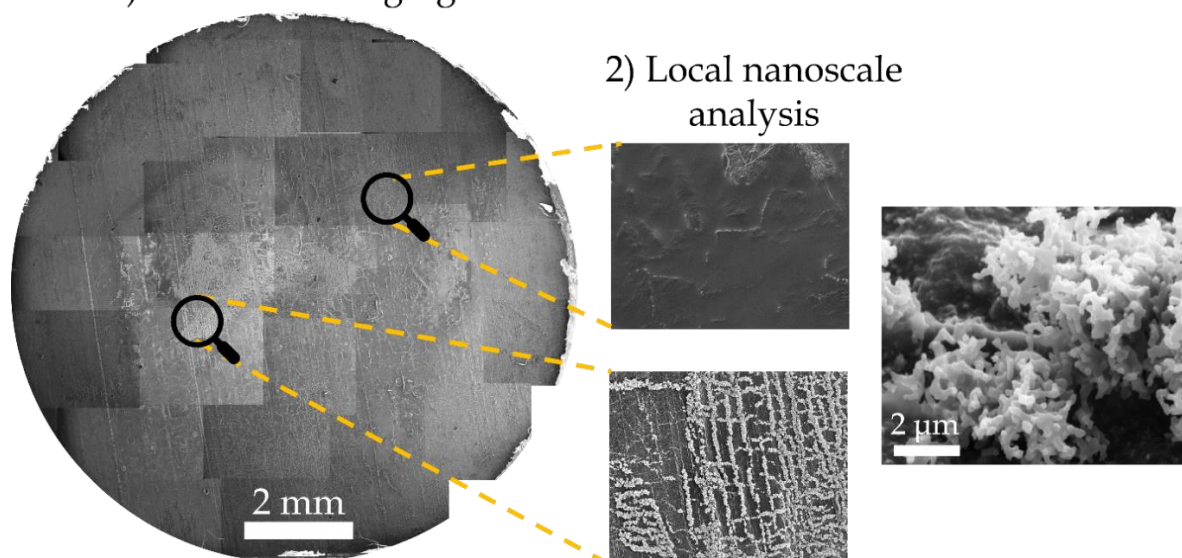


Figure 2: 1) stitched SEM images representing the surface of a complete circular Li-foil (diameter ~ 10 mm). 2) Local structural analysis elucidating regions with and regions without dendrites. (FOV ~ 10 μ m)

- 2) A collaboration with the German Aerospace Center (DLR) and the Helmholtz Institute Ulm for Electrochemical Energy Storage (HIU) led to an interesting study. The work focusses on structure-resolved electrochemical simulations to investigate the influence of resistive phases at the cathode/electrolyte interface

on the electrochemical performance and to identify potential degradation mechanisms. Based on the combination of structure-resolved simulations, density functional theory simulations, and experimental data i.e. SIMS chemical imaging, degradation mechanisms could be identified. SIMS data elucidates, that diffusion of Al from the electrolyte (LLZO) into the cathode phase (LCO) occurs during electrochemical cycling. Additionally, based on SIMS chemical imaging, the inactive LCO particle fraction (~16%) could be estimated.

In summary, the combination of the simulation results and the SIMS data allowed to attribute performance loss to different degradation mechanisms. This example shows that SIMS analysis, as well as correlative approaches could be used beyond the pure experimental scope and be implemented in and/or compared to simulations. This will first enhance the simulation models and consequently accelerate battery research, as better models suggest better designs.

5.2.3. Future Work

The following ideas are suggested as possible future work:

Chapter 2:

Regarding the *operando* SEM/SIMS workflow we are about to upgrade the design and workflow with the goal to perform fully *operando* SIMS, as for the moment only SEM is fully *operando*. A few modifications of the sample holder and the experimental configuration are already in progress. Different strategies are being investigated to limit potential interferences between electrochemical experiments and structural/chemical analysis.

Chapter 3:

The correlation between X-ray based techniques and SEM/SIMS was shown to be very useful when studying batteries, hence these approaches are worth being pursued. Especially quantitative techniques like XPS, EDX, and WDXS provide a perfect correlation allowing to study the batteries' structure, and chemical composition qualitatively as well as quantitatively.

Further studies on the growth and evolution of the SEI on Li anodes, by correlating XPS and SEM/SIMS (*ex-situ*) are in progress.

Chapter 4:

Operando neutron imaging, even if unpractical and preparation-intense, is a very promising technique as it combines structural and chemical quantitative data at the same time. Additionally, *operando* investigation is easily implementable with a cleverly designed sample holder. Regarding our approach, a neutron beam with a higher resolution would be essential in order to study individual dendrites grow

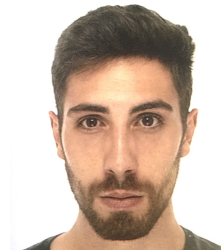
through the electrolyte. The capability of detecting and quantifying Li is essential for battery analysis. Hence, the experience and technical knowledge gained during the preparation and execution of the *operando* neutron experiment should be used in the future to design similar experiments.

Table 1 shows the possibilities of bilateral correlative techniques discussed in this work and elucidates that there are still a lot of unexplored combinations. This in relation with Table 2 showing which parts of a solid-state battery have been studied in this work opens many doors for battery research. Table 2 reveals that this thesis mainly focusses on the analysis of the solid-state electrolyte, the cathode and the interface between both. Future work could implement more complementary workflows focussing on the anode and the anode SSE interface.

References

- (1) Cressa, L.; Fell, J.; Pauly, C.; Hoang, Q. H.; Mücklich, F.; Herrmann, H.-G.; Wirtz, T.; Eswara, S. *A FIB-SEM Based Correlative Methodology for X-Ray Nanotomography and Secondary Ion Mass Spectrometry: An Application Example in Lithium Batteries Research*. *Microsc Microanal* **2022**, *28*, 1890–1895.
- (2) Ihrig, M.; Kuo, L.-Y.; Lobe, S.; Laptev, A. M.; Lin, C.-A.; Tu, C.-H.; Ye, R.; Kaghazchi, P.; Cressa, L.; Eswara, S.; Lin, S.-K.; Guillon, O.; Fattakhova-Rohlfing, D.; Finsterbusch, M. *Thermal Recovery of the Electrochemically Degraded LiCoO₂/Li₇La₃Zr₂O₁₂:Al,Ta Interface in an All-Solid-State Lithium Battery*. *ACS Appl Mater Interfaces* **2023**, *15*, 4101–4112.
- (3) Cressa, L.; Sun, Y.; Andersen, D.; Gerard, M.; Castro, O. de; Kopljar, D.; Nojabae, M.; Friedrich, K. A.; Schmitz, G.; Wirtz, T.; Eswara, S. *Toward Operando Structural, Chemical, and Electrochemical Analyses of Solid-State Batteries Using Correlative Secondary Ion Mass Spectrometry Imaging*. *Anal Chem* **2023**.

CRESSA LUCA



Employment History

Research assistant acting within the **interBATT project** at Luxembourg Institute of Science and Technology (LIST), Belval
September 2020 - present

- Design of advanced correlative analysis techniques for next-gen batteries.
- Contribution to the overall success of an european research project in collaboration with different partners including the German Aerospace Center (DLR).
- Documentation and dissemination of scientific results.

Temporary position as **experienced laboratory technician** at Laboratoires Réunis (LR), Junglinster
May 2020 - August 2020

- Managing a team of twelve technicians acting in four laboratories.
- The team was responsible for the whole procedure from sample reception to technical validation of the PCR-results.
- Up to 20,000 tests per day.

Graduate internship at LIST, Belval
August 2019 - February 2020

- Performing experiments & simulations to tackle scientific questions.
- Working with advanced characterization techniques and prototypes.

Student summer job at Luxembourg Institute of Health (LIH), Esch-sur-Alzette
August 2018 - September 2018

- Laboratory work and documentation - **Department of Infection and Immunity**.

Voluntary internship at LIH, Esch-sur-Alzette
July 2017 - August 2017

Education

Dr. rer. nat., Materials science
University of Stuttgart, **Institute for Materials Science**
September 2020 - present

Master of science, Chemistry
Leopold-Franzens University, Innsbruck
March 2018 - April 2020

Bachelor of science, Chemistry
Leopold-Franzens University, Innsbruck
October 2014 - March 2018

Contact:

244, rue de Soleuvre
Differdange, 4670
Luxembourg
+352 691931721
lcressa31@gmail.com

and of birth:

31.12.1994
Esch-sur-Alzette

Nationality:

Luxembourg

Languages

English

German

Italian

French

Spanish

Luxembourgish

Skills

Scientific background

Problem-solving

Software proficiency

Attention to detail

Creative thinking

Communication

Hobbies:

Mountaineering
Astrophysics
Computer science
Running
Chess

Supplementary Material

Publications

Analytical Chemistry

“Toward Operando Structural, Chemical, and Electrochemical Analyses of Solid-State Batteries Using Correlative Secondary Ion Mass Spectrometry Imaging”

Cressa, L., Sun, Y., Andersen, D., Gerard, M., De Castro, O., Kopljar, D., Nojabae, M., Kaspar, A.-F., Schmitz, G., Wirtz, T., Eswara, S.

Microscopy and Microanalysis

“A FIB-SEM Based Correlative Methodology for X-Ray Nanotomography and Secondary Ion Mass Spectrometry: An Application Example in Lithium Batteries Research”

Cressa, L., Fell, J., Pauly, C., Hoang, H.-Q., Mücklich, F., Herrmann, H.-G., Wirtz, T., Eswara, S.

ACS Applied Materials & Interfaces

“Thermal Recovery of the Electrochemically Degraded $\text{LiCoO}_2/\text{Li}_7\text{La}_3\text{Zr}_2\text{O}_{12}:\text{Al,Ta}$ Interface in an All-Solid-State Lithium Battery”

Ihrig, M., Kuo, L., Lobe, S., Laptev, M.A., Lin, C., Tu, C., Ye, R., Kaghazchi, P., Cressa, L., Eswara, S., Lin, S., Guillon, O., Fattakhova-Rohlfing, D., Finsterbusch, M.

International Journal of Hydrogen Energy

“Correlative high-resolution imaging of hydrogen in Mg_2Ni hydrogen storage thin films”

Andersen, D., Chen, H., Pal, S., Cressa, L., De Castro, O., Wirtz, T., Schmitz, G., Eswara, S.

★ Achievements

Competitive proposal accepted for beamtime at **Paul Scherrer Institute (PSI)** in 2022

“Best Science Case” at Alpbach Summer School 2022

Jury: “Most comprehensive science case that excellently fits the topic of the summer school.”

FNR Science Image Competition 2021: Distinction in the category “Object of study”

“For the jury, the picture invites the viewer to unleash their imagination. It is grainy and mysterious, as if it were a shot from outer space even though it is not.”

Summer Schools

Post Alpbach summer school event at ESA’s Educational Concurrent Design Facility (ESEC Galaxia), Libin November 2022

Alpbach, “Comparative Plasma Physics in the Universe” organised by Österreichische Forschungsförderungsgesellschaft (FFG) and European Space Agency (ESA), Alpbach

July 2022

High Resolution & Analytical Microscopy at Institute for Materials Science, University of Stuttgart

September 2021

References

Dr. Tom Wirtz - Head of Unit - Scientific Instrumentation and Process Technology (SIPT) at LIST

Dr. habil. Santhana Eswara - Senior Researcher at LIST

Prof. Dr. Dr. h.c. Guido Schmitz - Chair Professor Institute for Materials Science at University of Stuttgart

Dr. rer. nat., habil. Nikolaus Schlaich - Head of Laboratory at BioNTech IMFS